UNIVERSITÀ DEGLI STUDI DI PAVIA
DIPARTIMENTI FISICI

o

SCIENTIFICA ACTA

QUADERNI DEL DOTTORATO

VOLUME XVI ANNO XVI NUMERO 2

25 LUGLIO 2001

ISTITUTO NAZIONALE DI FISICA NUCLEARE

o

CENTRO STAMPA - DIPARTIMENTI FISICI
Via Bassi, 6 27100 Pavia

INDICE

Particle induced infrared emission in gases, liquids, and crystals

Davide Iannuzzi
Dip. di Fisica Nucleare e Teorica - Univ. di Pavia
I.N.F.N. - Sez. di Pavia

23rd July 2001

Contents

Abstract

We present the first study on particle induced infrared emission in noble gases. The aims of this investigation are twofold: (i) to understand the kinetic pathway in the de-excitation processes of a particle excited gaseous system, and (ii) to evaluate the potentiality of particle detectors based on infrared rather than vacuum-ultraviolet scintillation. We have thus studied the particle induced infrared spectra in Helium, Neon, Argon, Krypton, and Xenon, at room temperature and nearly atmospheric pressure, in the previously unexplored wavelength region between $\simeq 0.95$ μm and $\simeq 1.65$ μm. In lighter gases the emission is ascribed to atomic transitions. In Xenon, an excimer transition dominates the spectrum, which has been studied as a function of the gas density. In Krypton, an excimer transition is also present, although its intensity is comparable to that of atomic transitions. We have also observed secondary emission when an electric field is applied. The emission is ascribed to energy-transfer processes between drifting electrons and gas atoms. We have finally measured the light yield of the sample investigated (20600 ± 2400 photons/MeV for Xenon, $\simeq 5000$ photons/MeV for Argon and Krypton) and studied the properties of secondary scintillation near a thin wire. A first prototype of gaseous proportional scintillation counter, working in the infrared region, is presented. In the end, we report also on a first study on infrared emission in noble liquids and inorganic crystals.

Introduction

Particle induced light emission: a general overview.

Some materials have the property to convert into light much of the energy released by incident particles. These materials are commonly called *scintillators*[Bir-64, Kno-00].

In a *scintillation particle detector*, a light sensor is faced to a scintillator to detect the photon emission induced by the passage of an incident particle. The first primitive scintillation detector was assembled by chance in 1903 by William Crookes, who observed that some Radium (the radiative source), accidentally spilled on a Lead Sulfide film (the scintillator), appeared at his eyes (the light sensor) as a "turbulent luminous see"[Cro-03] (see figure I-1). After few years from its invention, this device (called by its inventor *spinthariscope*) was used to detect alpha particles in the famous Geiger-Marsden's experiments[Gei-09, Gei-10, Gei-13] (see figure I-2) that lead Ernest Rutherford to develop the modern theory of atoms[Rut-11, Rut-14]. Indeed, scintillators were already involved in what can be considered the first particle physics experiment, and that was the beginning of a long story.

Since then, scintillators have been developed as a basic compo-

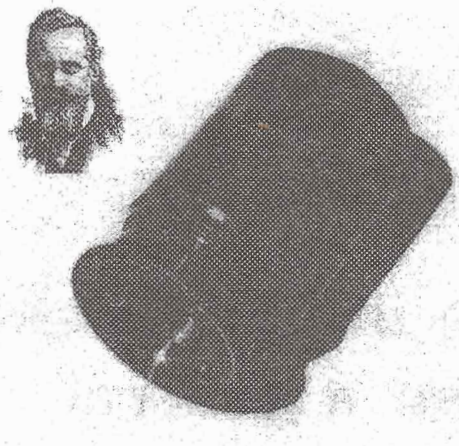

Figure I-1: A commercially-available spinthariscope (1920), and its inventor William Crookes.

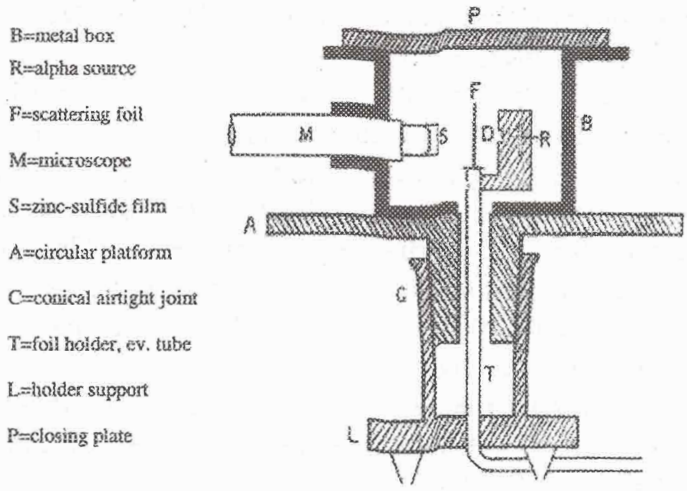

Figure I-2: A scheme of the Geiger-Marsden's experimental apparatus for the measurement of the deflection of alpha particles by a thin film[Gei-13].

Modality	Annual Production	Scintillation Content	Annual Volume
Planar X-Ray	1000000 screens	50 cc/screen	50000 lt
X-Ray CT	2000 scanners	75 cc/scanner	150 lt
SPECT	2000 scanners	3000 cc/scanner	6000 lt
PET	50 scanners	10000 cc/scanner	500 lt

Table I-1: Annual world-wide volume of scintillator required by medical imaging instruments[Mos-99]. (CT=Computed Tomography, SPECT=Single Photon Emission Computed Tomography, PET=Positron Emission Tomography).

nent in particle detectors for accelerators and cosmic rays experiments (see for example [Lec-99]). The important results obtained so far have been encouraging many international collaborations to rely on scintillator detectors for future large scale experiments, where the physical constraints and the harsh experimental conditions impose very tight instrumental specifications.

The spin-off of these investigations in other fields is extremely wide and successful. Scintillation detectors are commonly used in several devices for medical, analytical, and industrial applications, ranging from radiology to oil-well logging, from radio-immuno assay to non-destructive quality control. In table I-1 we report, by way of example, the number of medical imaging units annually sold. All in all, about 175 metric tons of scintillator are required annually[Mos-99] only for medical imaging instruments.

In spite of this world-wide broad interest, it has been noted that the research on scintillator detectors has been mainly focused on the particle induced light emission in the vacuum-ultraviolet to visible range[Car-98]. Very few studies have been reported on near-infrared and infrared scintillation, although there is no physical reason to rule out the hypothesis that some materials might efficiently convert the energy of incident radiation into photons in those wavelength

regions.

Our research is focused on the study of elementary processes in which the energy of a charged particle is converted into infrared photons. The aim of this study is twofold: (i) to investigate the feasibility of a new kind of particle detectors based on particle induced infrared emission rather than visible or ultraviolet scintillation, and (ii) to investigate possible unknown routes in the de-excitation pathways of beam excited samples, which could shed light on the interaction mechanisms of charged particles with matter.

We have focused our attention on the infrared emission properties of particle irradiated noble gases. Some preliminary studies on other samples (liquefied noble gases and crystals) have been also performed. In the present work we report on the results of this investigation.

In the following sections we present the arguments that encouraged our research.

I-1 Particle induced light emission in noble gases

The emission of vacuum-ultraviolet to visible light induced by incident radiation in noble gases has been widely investigated and quite well understood. Most of the known properties are summerized in [Pol-81] and [Bra-79] and recalled here below.

Spanning the wavelength region from in vacuum-ultraviolet to visible, the light spectra of particle-beam excited rare gases present a common feature. They are all characterized by two vacuum-ultraviolet broad bands (in the 100-200 nm range), commonly called *continua*, and two less intense, reasonably sharp, resonance lines at higher wavelength. The intensities of the lower wavelength band (called *first continuum*) dramatically decrease as the pressure of the gas is increased. For high density gases (pressure higher than 1 bar) the higher wavelength band (called *second continuum*) dominates

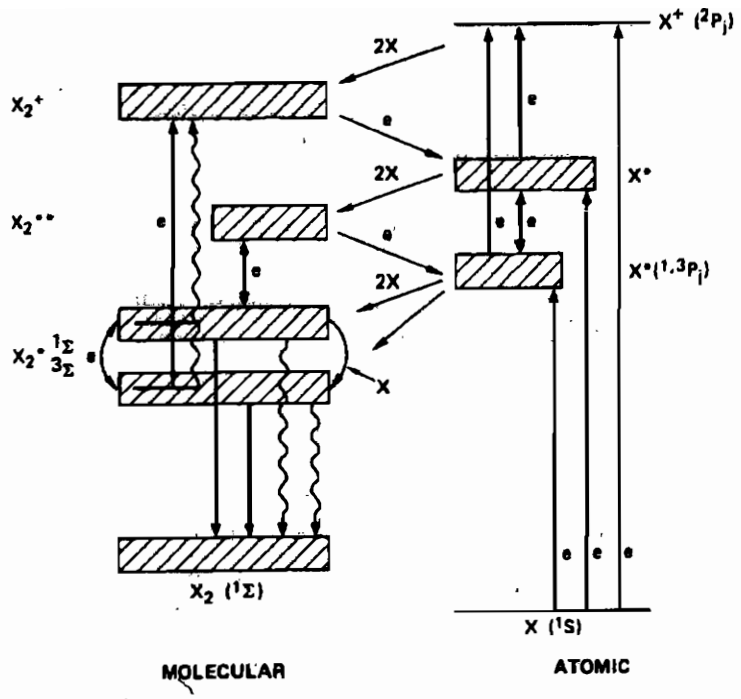

Figure I-3: Energy levels relevant to noble gas particle induced emission[Bra-79]. Electron collisions are denoted by letter e; photoemission and photoabsorption are indicated by wavy arrows.

the spectrum.

The origin of the emission observed is the radiative decay of some excited levels that are populated through a sequence of collisional energy exchanges. In figure I-3 we show a schematic diagram of this sequence. The incident radiation ξ ionizes and excites the gas X in the reactions:

$$\xi + X \longrightarrow X^* + \xi \tag{1}$$

$$\xi + X \longrightarrow X^+ + e^- + \xi \tag{2}$$

Although the interaction of the ground states of two noble gases

atoms is usually repulsive (except for weak long range attractions), strong chemical bounds can be formed in the interaction of an ionized atom with a ground state atom of the same species. The atomic ions of process 2 form in fact molecular ions through a very fast three body association process:

$$X^+ + 2X \longrightarrow X_2^+ + X \tag{3}$$

Subsequently, a dissociative recombination reaction quickly forms another excited (neutral) atoms:

$$X_2^+ + e^- \longrightarrow X^* + X \tag{4}$$

Also excited atoms can form strong chemical bounds with a ground state atom of the same species. These molecular states are called *excimers* and are usually populated through another three body reaction:

$$X^* + 2X \longrightarrow X_2^* + X \tag{5}$$

So, the passage of an ionizing particle through a noble gas sample gives rise to both (i) excited atoms and (ii) excimers. These excited states can de-excite either through non-radiative decay or through radiative transitions. Radiative transitions are responsible for the scintillation emission.

The sharp lines observed in the particle induced spectra in noble gases are the result of the $^3P_1 \longrightarrow {}^1S_0$ and $^1P_1 \longrightarrow {}^1S_0$ transitions. The first continuum is ascribed to transitions from high vibrational levels of the $^1\Sigma_u$ (emerging from the interaction of a $^3P_1$ atom with a $^1S_0$ atom) and $^3\Sigma_u$ (emerging from the interaction of a $^3P_2$ atom with a $^1S_0$ atom) excimer states to the repulsive ground state $^1\Sigma_g$ (that dissociates into two $^1S_0$ atoms). The second continuum corresponds to the same molecular transitions but originating from vibrationally relaxed levels. The states $^1\Sigma_u$ and $^3\Sigma_u$ are separated by less than 0.1 eV and both contribute to both continua. The intensity of the first continuum decreases with pressure because of the increase of the vibrational relaxation rate.

Gas	λ (nm)	Light Yield (ph./MeV)	Fast Comp. ns	Slow Comp. μs
Ar	126	29000	4.2	3.2
Kr	146	14000	-	0.35
Xe	173	20000	5.5	0.1

Table I-2: Scintillation properties of heavier noble gases (room temperature and nearly atmospheric pressure)[Hur-70, Miy-92, Bra-79].

I-2 Noble gases as scintillators: vacuum-ultraviolet versus infrared emission

In table I-2 we report the scintillation properties of heavier noble gases[Hur-70, Miy-92, Bra-79] at room temperature and nearly atmospheric pressure. The data refer to the second continuum emission (called, in this contest, *primary scintillation*), that at these densities, as already underlined, dominates the emission spectra.

The use of noble gases as scintillator has, in principle, several competitive features in comparison to other scintillators.

- The light yield (i.e. the number of photons emitted per unit of energy released by the particle in the scintillator) is of the same order of magnitude as the light yield of NaI(Tl) ($\simeq$ 40000 photons/MeV), the most widespread used scintillating crystal.

- The time response (characterized by a double exponential decay, corresponding to the fast $^1\Sigma_u$-$^1\Sigma_g$ decay and the slow $^3\Sigma_u$-$^1\Sigma_g$ decay, whose relative intensities depend on the density of the gas[Pol-81]) is quite fast (except for Argon), and among the faster of all the scintillators if only the fast component is detected.

- The mechanical constraints for a gaseous detector are largely less stringent respect to a crystal detector. A gaseous scintillation detector can satisfy almost all the geometrical configurations required and its performance is uniform also over very large volumes.

- Noble gases scintillation detectors are generally cheaper than other scintillators, especially when large volumes are required.

- The scintillation detection can be implemented by collecting the ionization electrons onto an electrode, thus having also a charge collection read-out.

It is also known that, if an electric field is applied to a gas scintillation detector, the ionization electrons, during their drift motion, can transfer the energy gained by the electric field to the gas atoms. Their subsequent de-excitation produces an increase of the light emission (with characteristics similar to the primary scintillation emission), called *secondary emission*[Pol-81], whose intensity can be widely controlled by appropriate shaping of the electric field configuration.

In spite of all these interesting features, particle detectors based on primary scintillation are not very widely used[Pol-81]. Detectors exploiting secondary scintillation (the so called *gas proportional scintillation counter*) are more routinely exploited, especially in X-ray astronomy and medical physics (see for example [Rac-00] and references therein).

The performances of noble gases scintillation detectors are strongly limited by the fact that the emission wavelength λ is in the vacuum-ultraviolet region. For $\lambda > 200$ nm, light guides or mirror-like collection devices are inefficient, and the transparency of commonly used optical windows is lower than 10%. The first problem limits the collection efficiency to the solid angle under which the light sensor sees the scintillation track. Large light detectors are usually faced to the electric field region, at the shortest distance possible within the geometrical features of the detector, and the energy resolution strongly depends on the overall

configuration[Sil-99]. The window transparency problem forces the use of costly special windows and, in some cases, of proper wavelength shifters.

Because of the problems discussed above, gaseous detectors have been used mainly as charge devices. Electrons can be easily drifted in localized regions where read-out electrodes can be placed, with a nearly 100% (cheap) collection efficiency[Sau-77].

The collection of infrared photons, compared to that of ultraviolet light, is much easier. Many materials (such as evaporated copper, gold, silver) with a reflectivity higher than 98.5% for nearly 1 μm wavelength photons[Gra-72] can be efficiently used for the assembling of infrared light guide or mirror-like collection devices. If particles induce infrared emission in noble gases, high collection efficiencies could be reached. Furthermore, no window problems would arise, because many materials can be used with transparencies higher than 80% over a wide infrared wavelength range[Klo-91]. On the other hand, the performances of infrared light sensor are generally worse than ultraviolet sensor (smaller detection surface, lower signal-to-noise ratio, lower quantum efficiency, and higher cost). However, due to its application in military and telecommunication systems, infrared technology is growing faster and faster, and the gap between ultraviolet and infrared sensor will probably be filled in the next years. For example, photomultiplier tubes sensitive up to 1.7 μm are now commercially available[Ham-ds].

Keeping in mind these considerations, let us analyze the effects of the passage of an ionizing particles on the atoms of the gas from an energetic point of view. It is well known that the number of ion-electron pairs produced by a particle with energy E_p is given by[Kno-00]

$$n_i = \frac{E_p}{W} \tag{6}$$

where W is the mean energy necessary to produce an ion-electron pair and must be measured experimentally. W is not simply equal to the ionization potential ϵ_i, but is given by

	ϵ_i (eV)	ϵ_{ex} (eV)	ϵ_{se} (eV)	W (eV)	E_{ex}	E_i	$E_{ex}+E_i$
Ar	15.7	13.2	6.9	26.2	13.7%	59.9%	73.6%
Kr	14.0	11.9	6.1	24.3	17.3%	57.6%	74.9%
Xe	12.1	9.8	5.3	21.9	20.5%	55.2%	75.7%

Table I-3: Estimates of the energy balance in the interaction of an ionizing particle with heavier noble gases.

$$W = \epsilon_i + \epsilon_{se} + \frac{n_{ex}}{n_i}\epsilon_{ex} \tag{7}$$

where ϵ_{se} is the mean secondary electron energy, n_{ex} and n_i are, respectively, the number of excited and ionized atoms, and ϵ_{ex} is the mean excitation energy. Using equations 6 and 7, we can derive the fraction of energy that goes, respectively, in excitation (E_{ex}) and in ionization (E_i):

$$E_{ex} = \frac{W - \epsilon_i + \epsilon_{se}}{W} \tag{8}$$

$$E_i = \frac{\epsilon_i}{W} \tag{9}$$

Using the values reported in literature[Lor-76], one obtains the values listed in table I-3. If we assume a complete ion-electron recombination, we can argue that $\simeq$75% of the energy released by the particle goes into excitation. Suppose that only $\simeq$3% of the excited states relaxes by emitting an infrared photons (typical energy 1 eV). In this case, we would obtain a light yield of the similar to that of NaI(Tl). This means that even very low efficiency processes could give rise to important results for the development of particle detectors based on infrared scintillation.

Among the de-excitation processes that could result in the emission of infrared photons are atomic transitions, although previous

measurements in the visible to vacuum-ultraviolet range show that atomic radiative decays are not very efficient[Pol-81]. More interestingly, it has been observed[Mul-70, Koe-74] that excited atoms should produce other excimer states than $^{1,3}\Sigma_u$, which might de-excite emitting infrared photons. These processes have never been investigated, and could hopefully provide a very efficient scintillation mechanism.

It is also interesting to note that vacuum-ultraviolet second continuum is also exploited as lasing transition in commercially available excimer lasers[Bra-79][††]. The investigation of particle induced infrared emission could allow to identify some de-excitation mechanisms that could be extremely important in the depopulation kinetic of the lasing levels. Moreover the presence of eventual infrared excimer decays could open a new possibility for the development of high power infrared laser.

I-3 Particle induced infrared emission in noble gases: previous investigations

The first work on emission measurements in the near-infrared regions for noble gases irradiated with ionizing radiation was performed in 1968[Ara-78]. In this experiment, Neon, Argon, Krypton, and Xenon samples, kept at room temperature and nearly atmospheric pressure, are excited by a pulsed electron beam (500 keV, 10 ns, 10 J/bunch). The light produced by the electrons enters a monochromator coupled with a photomultiplier tube. The authors show that the emission spectra in the spanned wavelength region (between 350 and 1070 nm) are characterized by some atomic lines already observed in discharge experiments. No estimation on the

[††]Actually, excimer lasers based on pure noble gases have quite low efficiency. Better results are usually obtained with mixtures containing a buffer gas, such as Neon, plus ArF, KrF, XeCl, or XeF.

emission intensity is reported.

The hypothesis of using infrared light in gas scintillation counters was firstly suggested by P. E. Thiess and G. H. Miley[Thi-74], after a quite detailed study on atomic transitions induced by alpha particles in Helium, Neon, Argon and some mixtures of these gases with some other minority species, at room temperature and pressure ranging from few Torr to atmospheric pressure. The authors report that both primary and secondary scintillation can be observed in the wavelength region between 330 and 850 nm. In both cases, the emission is ascribed to atomic transitions. Also in this work, no measurement of the light yield is given.

The idea has been considered more recently by another group. In their first related article[Lin-88a], primary and secondary scintillation spectra in the 350-930 nm wavelength region are reported, for electron excited Neon, Argon, Krypton and Xenon at room temperature and pressure ranging from 0.2 to 2 bar. The hypothesis that atomic transitions are the sole origin to the emission observed is confirmed. Furthermore evidences are reported of a change in the relative intensities of the spectral lines with the increase of the electric field.

The authors subsequently show that secondary scintillation in the wavelength range previously explored can be successfully exploited for intensity measurements during Proton Induced X-ray Emission (PIXE) analyses[Lin-88b]. Similarly, in [Lin-88c] they report on the detection of alpha particles by means of another gas proportional visible plus near-infrared scintillation chamber. In figure I-4 we show the energy spectra of a 5.5 MeV alpha source obtained by exploiting visible plus near-infrared secondary scintillation of Neon, Argon, Krypton and Xenon (room temperature and atmospheric pressure).

The same group have also shown that the visible or near-infrared secondary emission can be amplified just by irradiating the high electric field region with a laser tuned on $(n+1)s$ to $(n+1)p$ atomic transitions (where n is the principal quantum number of the ground state) and detecting photons at higher wavelengths[Lin-91,

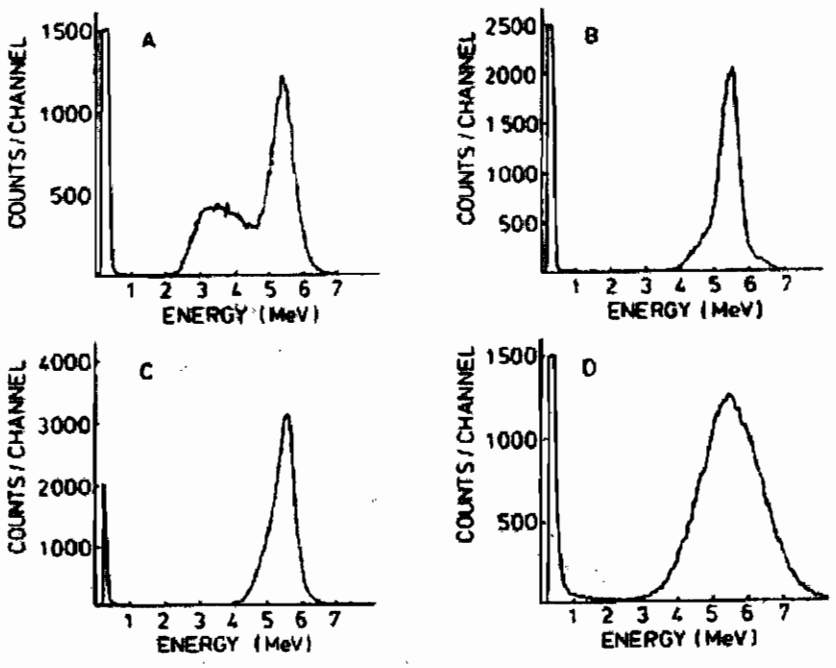

Figure I-4: Energy spectra of a 5.5 MeV alpha source obtained with a visible plus near-infrared scintillation counter filled with Neon (A), Argon (B), Krypton (C), and Xenon (D)[Lin-88c].

Lin-92a, Lin-92b]. In figure I-5 we show their results obtained with Neon. The energy spectra of a 5.5 MeV alpha source is shifted on the multichannel analyzer when the laser is used. The net gain for the laser-enhanced scintillation signal is 9 when the laser is tuned on the $3p[5/2]_3$ - $3s[3/2]_2$ transition. Similar results for Argon are reported.

The two processes responsible for this amplification are reported in figure I-6 for Neon. The laser light induces a transition from an $s-$level (populated by the passage of the particle) to a $p-$level. When the $p-$excited state decays towards an $s-$levels, near-infrared fluorescence photon are emitted. Transitions for which the final $s-$state has an energy higher than the initial $s-$state have a wave-

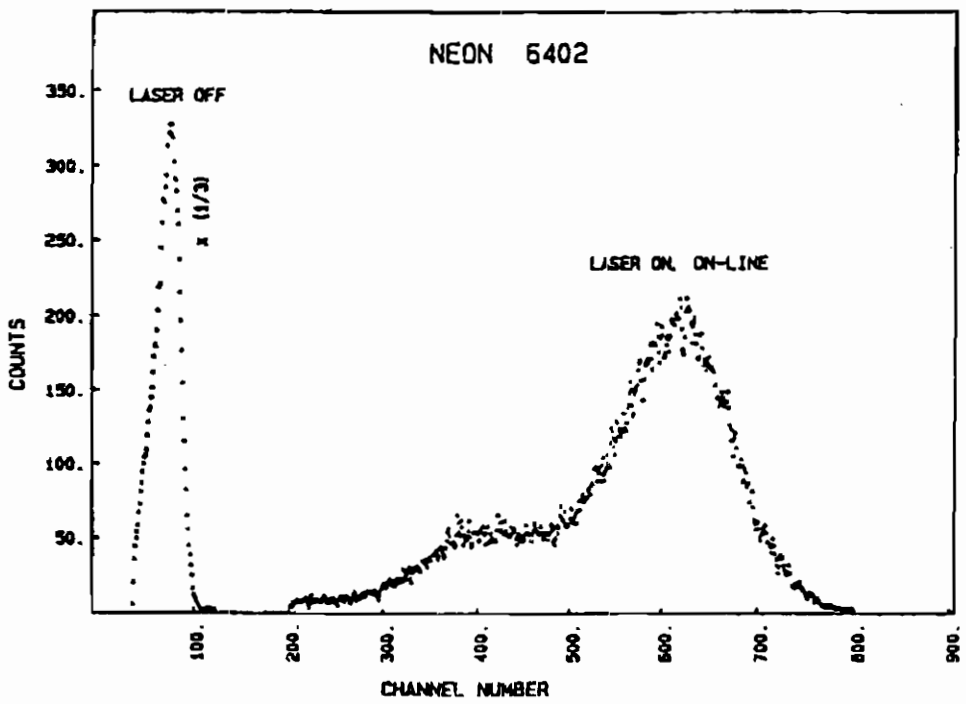

Figure I-5: Energy spectra of a 5.5 MeV alpha source obtained with a near-infrared scintillation counter filled with 500 mbar, room temperature, Neon. The left peak corresponds to normal operations. The right peak corresponds to the laser-enhanced scintillation signal.[Lin-91].

length longer than the laser one, and can therefore be detected. Alternatively, the $p-$excited atom can transfer by collision its energy to another atom, that is excited to a lower lying $p-$state. Consequently, the photon corresponding to the p to s decay can be detected. In this second case, the emission brings the atom back to the original $s-$state, allowing the cyclic repetition of the laser excitation.

In 1998 G. Carugno, using a HgCdTe infrared sensor, has observed that both primary and secondary emissions have some components also at higher wavelengths (up to 15 μm)[Car-98]. He called

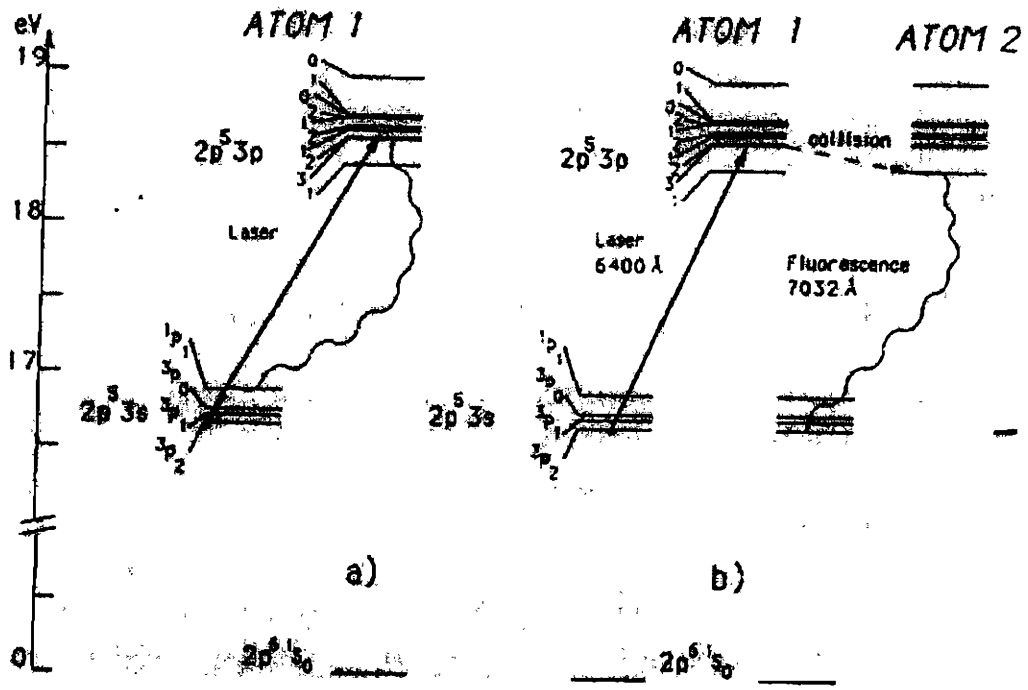

Figure I-6: Scheme of the mechanisms responsible of the laser-enhanced near-infrared scintillation.[Lin-91].

the primary emission *prompt emission* and the secondary emission *drift emission*. Hereafter we shall use his nomenclature. No explanation on the emission mechanisms is given.

We can conclude that no systematic study has been performed on particle induced emission in noble gases in the wavelength region $\lambda > 950$ nm, although there is experimental evidence that both infrared prompt emission and infrared drift emission take place. In the wavelength region between the second vacuum-ultraviolet and $\simeq$ 950 nm, only atomic transitions have been observed. The emission is huge enough for being exploited as scintillation light in particle detectors. However, no direct estimation of the light yield is given, and this detecting system has been used only in the prototypes for the initial measurements. From the results reported

above, one could conclude that the emission observed by Carugno in the infrared region must be ascribed to high lying atomic transitions, whose relatively low intensities would not allow to obtain competitive results using infrared rather than vacuum-ultraviolet scintillation light. In the following chapters we will show that things are not so trivial.

I-4 Considerations on other materials

Second continuum vacuum-ultraviolet scintillation takes place in noble liquids as well[Hel-85, Kub-82]. Scintillation light has a fast decay component (as in the case of gases) with a light yield comparable to that of NaI(Tl) (for a recent review on the properties of liquid noble gas scintillation and their application to particle detectors, see [Dok-99]). With respect to the gas phase, a noble liquid scintillator needs cumbersome cryogenic set-ups. Furthermore, since the light yield and the attenuation length depend on the purity of the sample, much more attention must be paid to impurities concentrations. However, the density of a liquid is generally two-three orders of magnitude higher than the density of a gas kept at room temperature and nearly atmospheric pressure. For this reason, many investigators have been trying to realize liquid noble gases scintillation detectors. Most of the works reported so far, however, show that the energy resolution of the prototypes is worse than the energy resolution that can be obtained with NaI(Tl)-based detectors, and such poor result comes mainly from the low light collection efficiency for ultraviolet photons and its non-uniformity. However, some groups are still working on underground and leptonic number-violating experiments using liquid Xenon or liquid Argon scintillation detectors[Bac-94, Ben-93, Dok-99].

The advantages of infrared light with respect to vacuum-ultraviolet light, the energetic considerations discussed above, and the possible presence of other excimer transitions in the infrared range are the main arguments that have lead us to investigate the pre-

Material	Light Yield (ph./MeV)	Emission Wavelength (nm)	Φ
Gd_2O_2S(Tb)	70000	545	16%
LaOBr(Tb)	67000	425	20%
CsI(Tl)	65000	545	15%
Y_2O_2S(Tb)	60000	545	14%

Table I-4: Scintillation properties of some crystals commonly used in particle detectors[Mos-99, Val-93]. Φ is the fraction of the energy released by the particle that goes into scintillation light.

viously unexplored properties of particle induced infrared emission in liquid Argon and Xenon.

We also have started a preliminary investigation on particle induced infrared emission in crystals. In table I-4 we report the scintillation properties of the highest light yield scintillating crystals [Mos-99, Val-93]. Column 4 shows the fraction of the energy released by the particle that goes into scintillation light. Once again, a great deal of the energy is lost in other processes. Some of these processes could in principle give rise to the emission of infrared photons. As a matter of fact, the irradiation of CsI(Tl) with X-rays give rise to infrared emission[Tak-96]. The origin of this emission is not yet clear, and, to our knowledge, this is the only crystal ever investigated in the infrared wavelength region. For this reason, we decided to study particle induced infrared emission in nearly 30 different crystals.

I-5 Aim and scheme of the present work

The aims of our work can be summerized as follows:

- To project and assemble an experimental apparatus for the

measurements of the spectra of particle induced infrared emission in noble gases at room temperature and nearly atmospheric pressure.

- To measure the spectra in all the noble gases species as far as prompt emission is concerned.
- To analyze the spectra and deduce the main kinetic pathways that give rise to the emission observed.
- To study in the details the drift emission in order to confirm that its origin must be ascribed to the energy transfer among the drifting electrons and the gas atoms.
- To measure the light yield of the most interesting samples and to investigate possible applications of both prompt and drift emission for particle detection purposes.
- To start a preliminary investigation of particle induced infrared emission in other samples, namely (i) noble liquids, and (ii) inorganic crystals.
- To identify possible research topics to continue successfully our investigation.

Thus, the scheme of the report is the following:

- **Chapter 1:** In Chapter 1 we describe the experimental apparatus we designed and assembled for systematic measurements of particle induced infrared spectra of noble gases. The facility consists of an electron gun (the ionizing source), an ionizing chamber (that contains the sample), and a Fast-Fourier-Transform Michelson spectrometer (for the spectrum analysis). We report all the technical details and underline the potentiality of this instrument.
- **Chapter 2:** In Chapter 2 we present the results of particle induced infrared spectra in Helium, Neon, Argon, Krypton, and

Xenon, at room temperature and nearly atmospheric pressure, in the wavelength region between $\simeq 0.95$ μm and $\simeq 1.65$ μm. We show that the emission mechanism for lighter gases (Helium, Neon, and Argon) is dominated by atomic emissions (although some other mechanisms could also be present). In Xenon, on the contrary, an excimer transition dominates the spectrum. In Krypton, an excimer transition is also present, but its intensity is of the same order of magnitude of the atomic emissions. We also present a detailed study of the behavior of the excimer peak in Xenon with pressure (in the 1 to 9 bar interval), and explain the results with a simple model, that is also tested on the results obtained with an Argon-Xenon mixture.

- **Chapter 3:** In Chapter 3 we show that the drift emission in gaseous Argon is in effect induced by the de-excitations of the atoms excited by the drifting electrons that gain energy from the electric field. The experimental results are compared to a kinetic model. The qualitative agreement with the data is very good, although some experimental problems do not allow a precise quantitative comparison of the theory with the experiment.

- **Chapter 4:** In Chapter 4 we present the measurement of the light yield of gaseous Xenon. The result is 20600 ± 2400 photons/MeV. Argon and Krypton show much lower light yield ($\simeq 5000$ photons/MeV). An experimental investigation on the possibility of using secondary infrared emission for particle detection purposes is also presented, together with an image of a proton bunch obtained with a rough prototype.

- **Chapter 5:** In Chapter 5 we report on the investigation on noble liquids and inorganic crystals. Firstly, we show that the light yield in liquid Xenon is dramatically lower than the value for gaseous Xenon (a factor 200 lower). Then, we experimentally demonstrate that, in the liquid phase, the excimer

peak is suppressed, and no drift emission occurs. Concerning inorganic crystal, we present the results obtained for nearly 30 samples. CsI(Tl) and YAG(Yb) are the most interesting infrared scintillators. Their light yields are, respectively, 5100 ± 470 photons/MeV and 74800 ± 9700 photons/MeV. Some applications are discussed.

- **Conclusions and perspectives:** In this final chapter, keeping in mind the results reported, we suggest possible future experiments.

Chapter 1

A facility for the study of particle-induced infrared emission in noble gases.

Introduction

We have already seen that the study of the light spectra of beam excited noble gases has provided the key elements to identify the dominant emission mechanisms. We have also underlined that the wavelength region investigated so far ranges from the vacuum-ultraviolet to the near-infrared part of the electromagnetic spectrum, although there is evidence that some emissions occur also at higher wavelengths[Car-98]. One of the aim of the present work is to understand the origin of the infrared emission observed in beam excited noble gases.

As in the case of the other wavelength regions, many informations on the emission mechanism can be obtained through a systematic study of the spectrum. A spectrum characterized by sharp lines, corresponding to atomic transitions, would clearly reveal that the de-excitation of particle excited atoms is responsible for the emission under investigation (as in the case of visible and near-infrared emission). On the other hand, other pathways have been

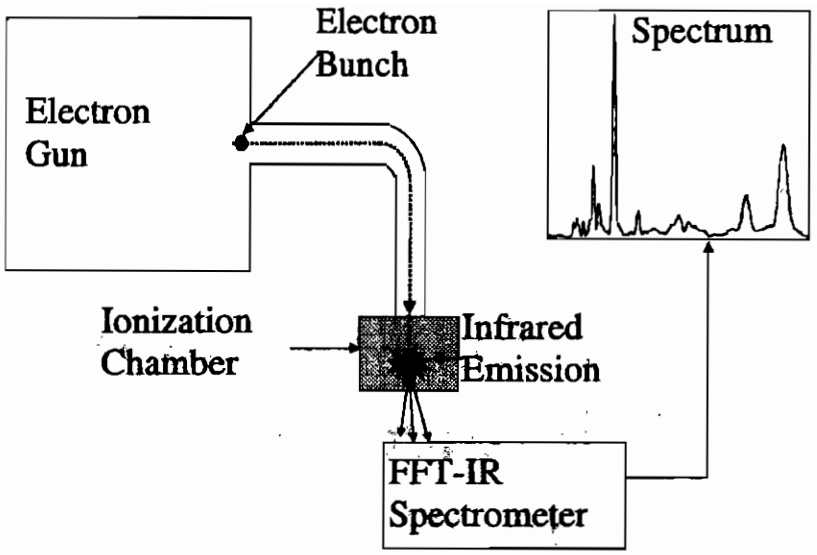

Figure 1.1: A scheme of the experimental apparatus.

suggested[Mul-70] in which high excited excimer levels might be populated, giving rise to radiative bound-free molecular transitions (as in the case of the excimer vacuum-ultraviolet second continuum). It is therefore evident that the measurement of the particle induced infrared emission spectrum in noble gases is a powerful tool for understanding not only of the emission mechanism, but, more generally, of the interaction of radiation with matter.

For this reason, we realized an experimental facility for systematic measurements of the emission spectra induced by ionizing particles in noble gases. In this chapter, we describe the technical details of this instrumentation.

1.1 Experimental details

A simplified lay-out of the experimental apparatus is shown in figure 1.1. A pulsed electron beam, produced by an homemade electron

gun, enters an ionization chamber filled with the gaseous sample. A Fast-Fourier-Transform Michelson spectrometer (FFT-IR) analyzes the infrared light at the exit of the chamber. The experimental apparatus can be divided into three main devices: (i) the electron gun, (ii) the ionization chamber, and (iii) the FFT-IR spectrometer (see also figures 1.2 and 1.3).

1.1.1 The electron gun

The homemade pulsed electron gun is represented in figure 1.4. Electron bunches are produced in a high vacuum stainless steel chamber (hereafter called *extraction chamber*) by means of photoelectric extraction from a metallic cathode. The cathode is kept at negative voltage with respect to a centrally pierced metallic anode, set in front of it and kept to ground. The photoelectrons are therefore accelerated by the electric field towards the anode, exit the extraction chamber passing through the anode hall, and enter an high vacuum stainless steel beam pipe. In the beam pipe, the bunches are magnetically focused and bent towards the entrance of the gas chamber.

The extraction chamber and the beam pipe are kept at a vacuum level of the order of 10^{-6} mbar or less by means of two consecutive turbo-molecular pumps coupled with a rotatory pump. This avoids high voltage discharges in the extraction chamber and beam losses in the beam pipe.

Photoelectric extraction is realized with a Ne-Ar-F excimer laser (Lambda Physik) that emits 192 nm wavelength photons in 50 ns long bunches at a maximum rate of 100 Hz, with an emission power of 10 mJ. The photons enter the beam pipe through a MgF_2 window, pass through the anode hall, and hit frontally the photocathode (see figure 1.4).

The photocathode is a brass plate, polished with a 0.25 μm diamond paste and fixed onto a stainless steel electrode. The pierced anode is also of stainless steel. The shapes and the dimensions of the electrodes, reported in figure 1.5, are designed for maximizing

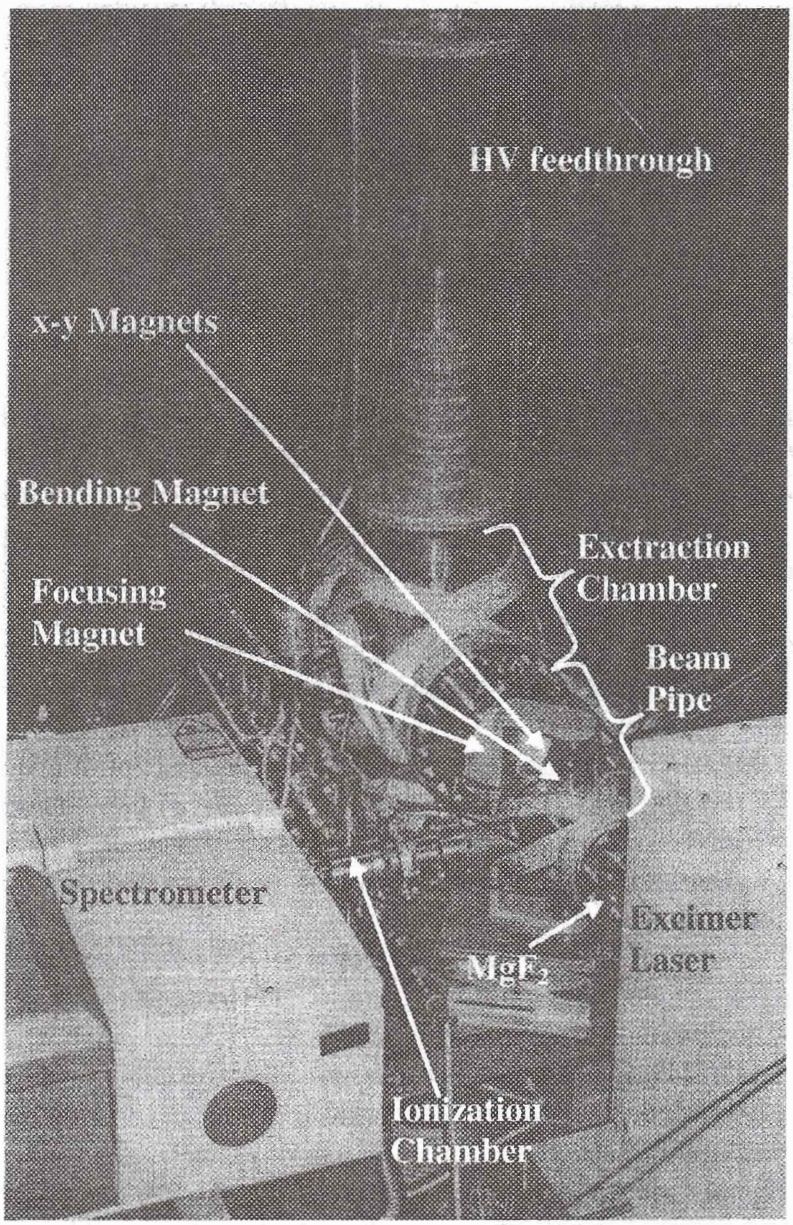

Figure 1.2: A picture of the experimental apparatus.

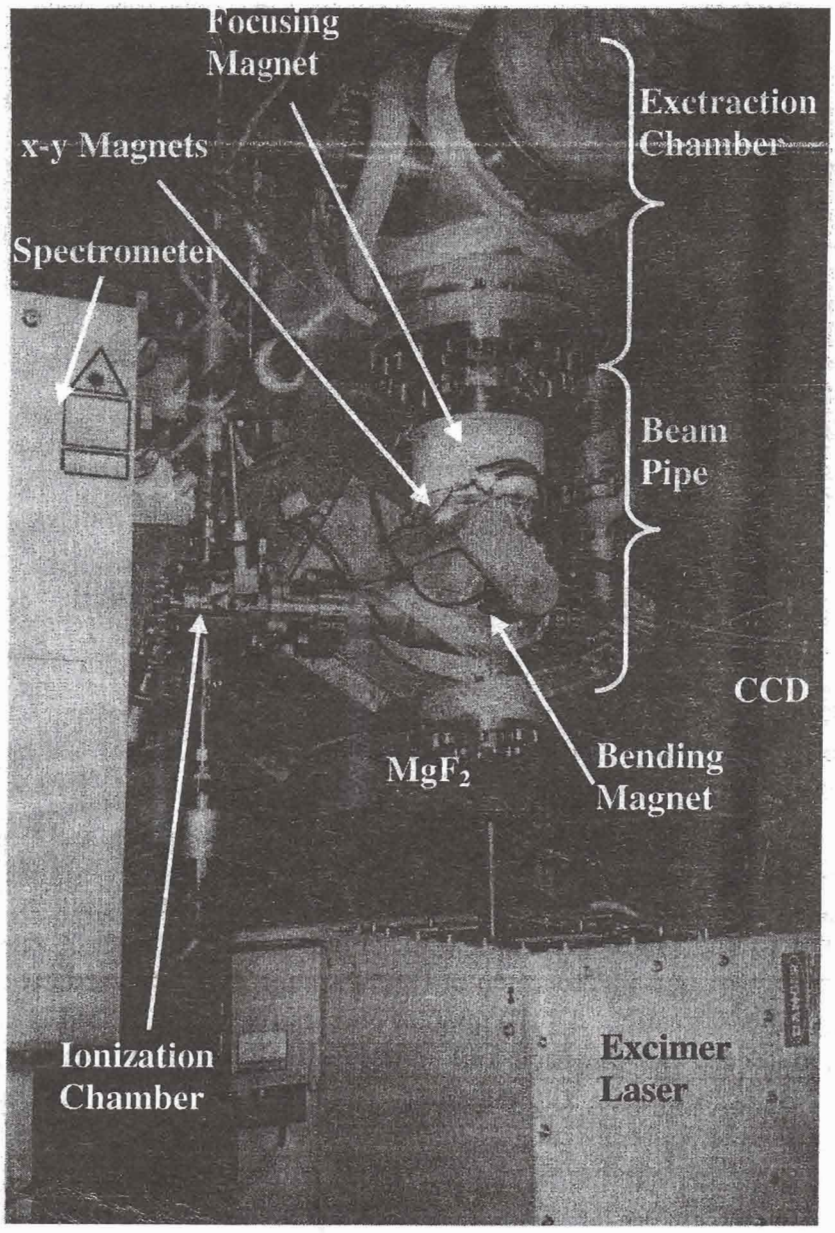

Figure 1.3: A picture of the experimental apparatus (top view).

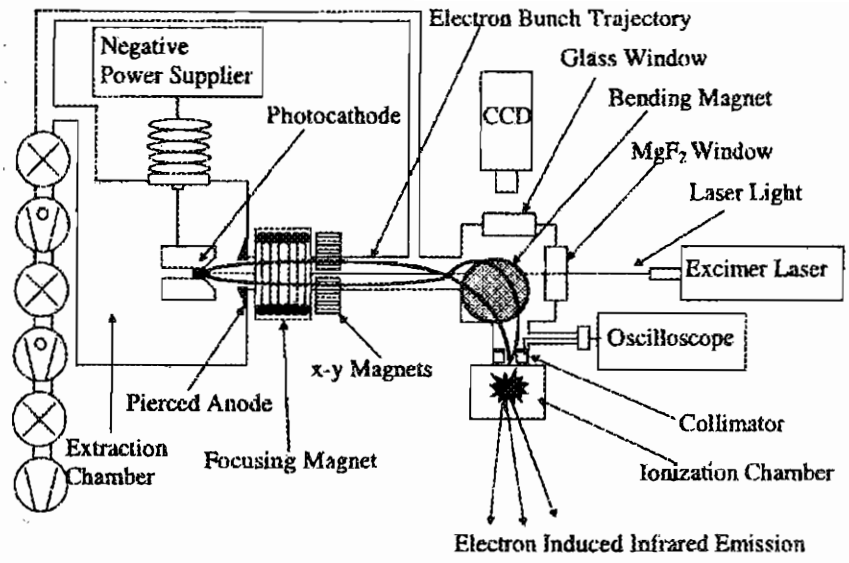

Figure 1.4: A schematic view of the electron gun.

the charge output of the electron gun. The cathode is connected to a power supply (RHR120W Spellman) that provides a negative voltage up to -100 kV, while the anode is kept to ground.

Near the anode, at the beginning of the beam pipe, a coil magnetic lens focuses the electrons. Other two couples of smaller coil magnets correct the trajectory of the electrons in the plane orthogonal to the beam pipe direction. Finally, a coil bending magnet accomplishes a 90° rotation of the beam direction, towards the gas chamber entrance. All the magnet currents can be adjusted in order to optimize the direction and spot-size of the electron bunches.

Before entering the chamber, the electrons pass a collimator made by a centrally pierced metallic plate. The hall is aligned with the entrance window of the gas chamber, and its diameter is equal to the entrance window diameter. The plate is connected to an high impedance (1 MΩ) channel of a digital oscilloscope. This collimator is used to periodically measure the mean number of electrons per

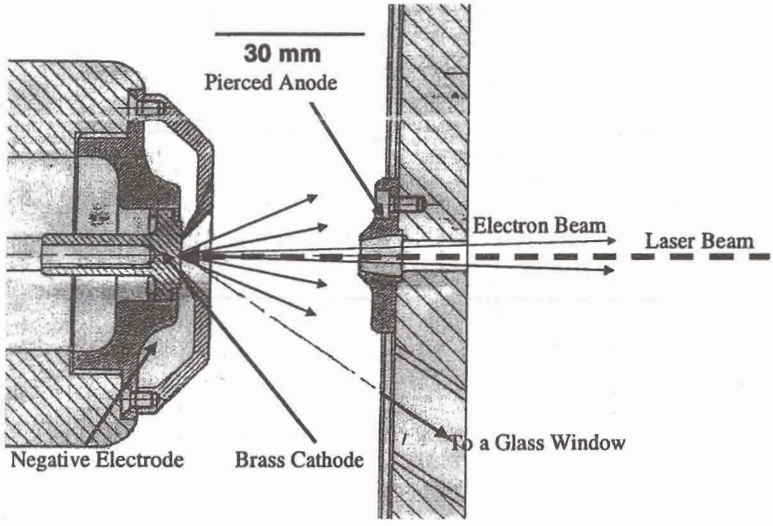

Figure 1.5: A drawing of the electrodes of the electron gun.

bunch. Adjusting the current on the coils of the two deflection magnets or of the bending magnet, we make the bunches collide against the metal. A typical signal corresponding to a collision of an electron bunch is shown in figure 1.6.

Integrating this signal by means of the oscilloscope computational options, we obtain a direct measure of the charge per bunch at the end of the beam pipe. Values up to 10 nC/bunch can be reached.

The collimator can be also used as a monitor for the beam direction and divergence. Its metallic surface faced to the beam pipe is covered with a thin film of fluorescent material. In front of it, in the position reported in figure 1.4, a CCD-camera detects the fluorescence light induced by the electrons that collide against the collimator. The minimum spot size that can be obtained is about 3 mm.

In table 1.1 a summary of the electron gun properties is re-

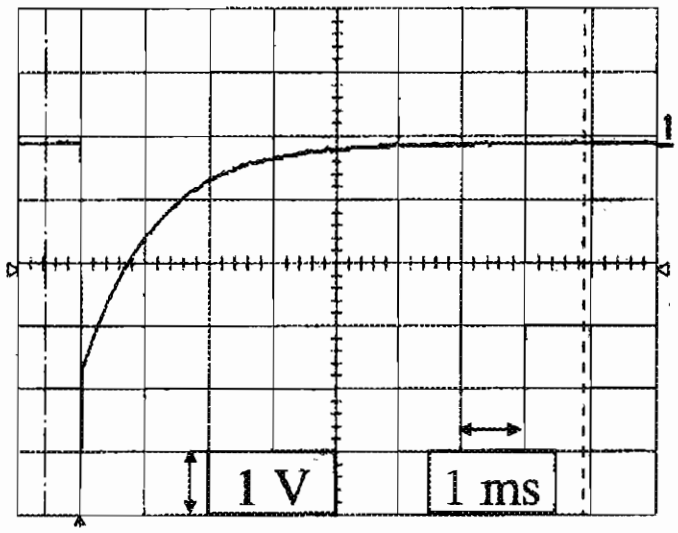

Figure 1.6: Typical signal for the measurement of the number of electrons per bunch.

Electron energy	Pulse duration	Pulse frequency	Charge per bunch	Spot size
up to 100 keV	50 ns	1 to 100 Hz	up to 10 nC	3 mm

Table 1.1: Electron gun properties

ported.

1.1.2 The ionization chamber

A schematic view of the ionization chamber is reported in figure 1.7 (see also figure 1.8). It consists of a stainless steel cylindrical chamber, mounted with the basis orthogonal to the beam direction.

The electrons enter the chamber passing a 3 mm diameter Kapton window on the center of one of the two basis of the cylinder. The thickness of the Kapton foil is 13 μm. Using the National Institute

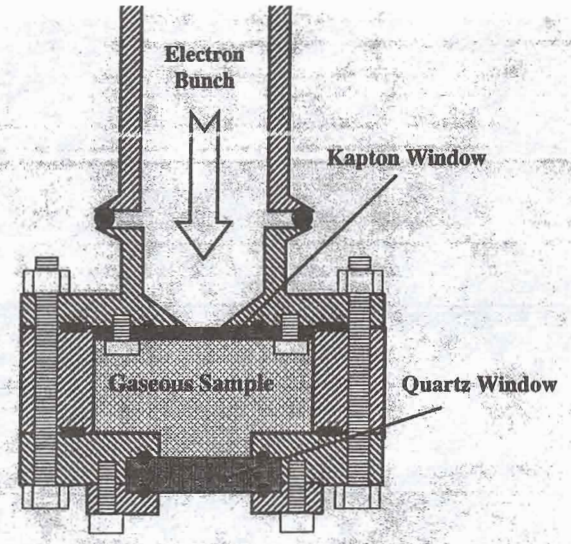

Figure 1.7: A schematic drawing of the ionization chamber.

of Standards and Technology data for the energy-loss of electrons in Kapton[Ber-00], it can be estimated that a 100 keV beam looses approximately 7.1 keV passing of the entrance window. For lower energies, we refer the reader to figure 1.9. At room temperature, the pressure inside the chamber can be set up to nearly 20 bar before breaking the Kapton foil. Thus, measurements of gaseous samples at pressure up to 20 bar can be performed.

The infrared light exits the chamber passing through a quartz window opposite to the entrance window. The transparency of the quartz window in the infrared range is given in figure 1.10. The thickness of the window is 1 cm. The aperture diameter is also 1 cm, while its distance from the entrance window is 5 cm. In table 1.2, the range of 100 keV electrons in Helium, Neon, Argon, Krypton and Xenon at room temperature is given as a function of the gas pressure. It can be seen that, except for lighter gases, and for pressure higher than $\simeq$ 2 bar, almost all the electrons are

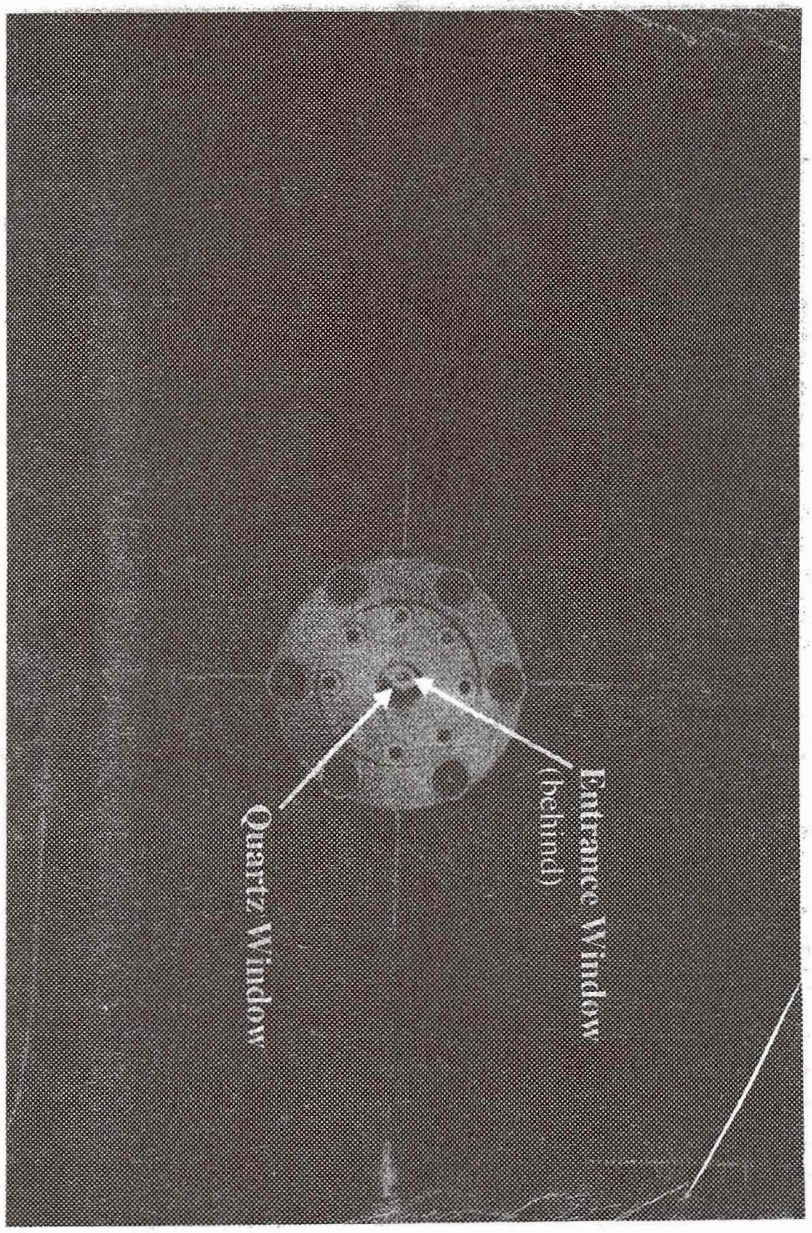

Figure 1.8: A frontal picture of the ionization chamber.

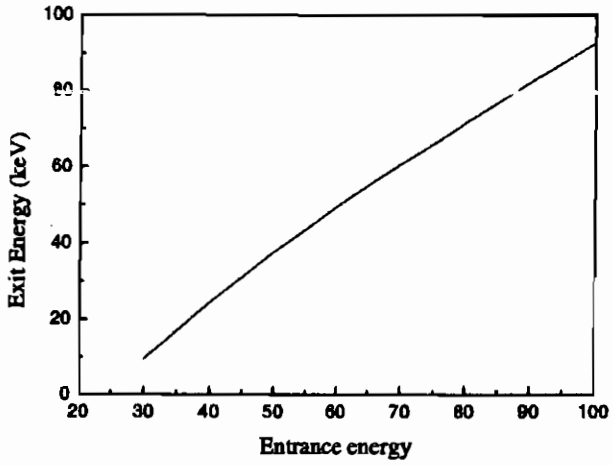

Figure 1.9: Energy of the electrons after the passage of the entrance window.

stopped before hitting the quartz window.

The chamber is connected to a bottle containing the gas with a nominal purity of about 10 ppm, to a vacuum pump and to a recirculation system equipped with an 0.1 l purifier cartridge (Oxisorb, Messer) (see figure 1.11 and 1.12). The chamber is evacuated down to 10^{-5} mbar before each gas filling by means of a turbomolecular pump coupled with a rotatory pump. After the filling, a recirculation pump forces the gas to flow continuously through the purifier cartridge during all the measurement time with a flow rate of the order of 1 l/min. This technique allows to keep the gas purity higher than 1 ppm, so that spectra features induced by impurities can be neglected.

1.1.3 The FFT-IR spectrometer

The infrared spectrum is performed by means of a FFT-IR spectrometer (Bruker Equinox55) whose entrance faces the light exit

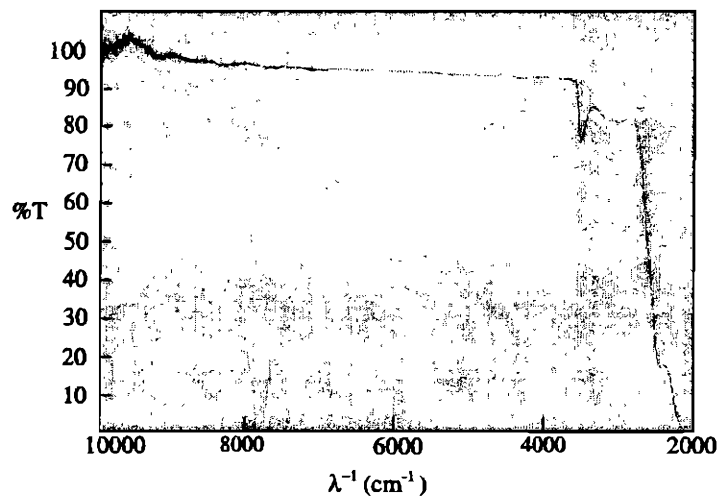

Figure 1.10: Transparency of the quartz window. In the opinion of the authors of the measurements, values higher than 100% are due to systematic errors and must be considered as 100% value.

	1 bar	2 bar	3 bar	4 bar	5 bar	10 bar	20 bar
He	87.9	43.9	29.3	22.0	17.6	8.8	4.4
Ne	21.0	10.5	7.0	5.2	4.2	2.1	1.0
Ar	12.3	6.1	4.1	3.1	2.5	1.2	0.6
Kr	6.9	3.4	2.3	1.7	1.4	0.7	0.3
Xe	4.9	2.4	1.6	1.2	1.0	0.5	0.2

Table 1.2: Range of 100 keV electrons in rare gases at room temperature (in cm).

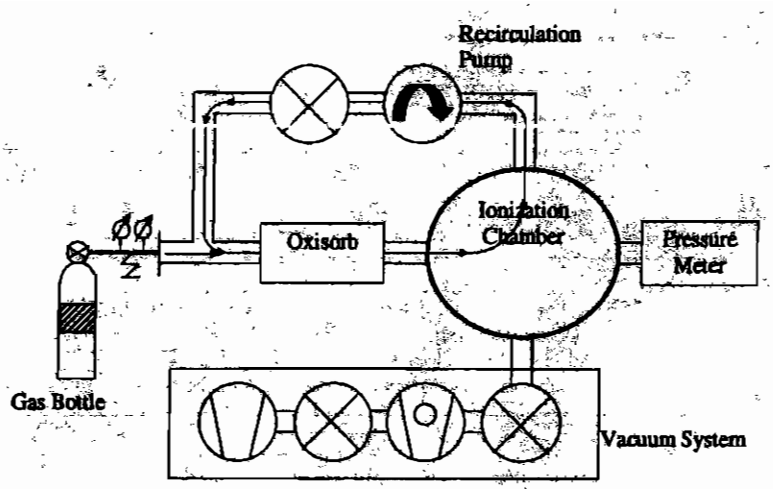

Figure 1.11: Scheme of the recirculation system.

window of the ionization chamber. A schematic view of its most important optical hardware is shown in figure 1.13. The infrared light produced inside the ionization chamber is focused onto the KBr beam splitter of a Michelson interferometer. The beam splitter allows half light to pass through while it reflects the other half. The two splitted beams are reflected back to the beam splitter by two different mirrors. One of the two mirror is located at a fixed distance L from the beam splitter. The distance of the other mirror (hereafter called *moving mirror*) from the beam splitter is $L + x$, where x is an adjustable distance. Thus the two parts of the splitted beam pass again through the beam splitter after a total path length of $2L$ and $2(L+x)$. When the two halves of the beam recombine on the beam splitter, they have an optical delay of $2x$. The recombined beam is finally focused on an infrared detector that measures the intensity I of the light as a function of the moving mirror displacement x. The function $I(x)$ is usually called interferogram. For example, in an ideally monochromatic emission at wavelength λ, the interferogram is:

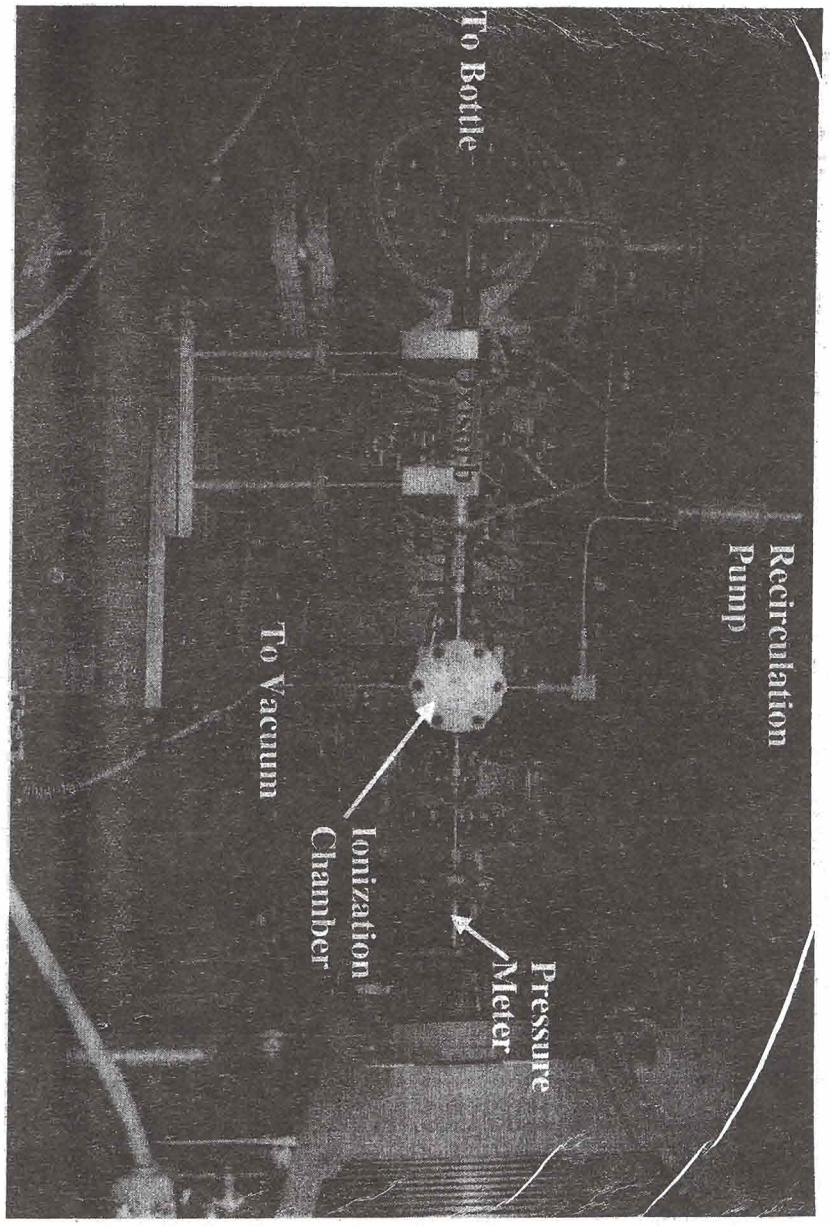

Figure 1.12: A picture of the recirculation system.

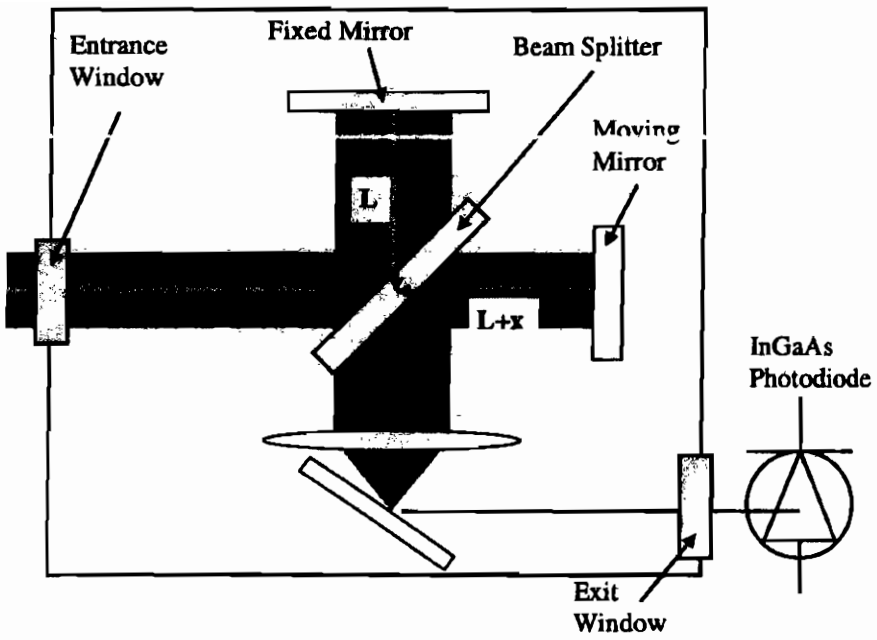

Figure 1.13: A schematic view of the spectrometer's optics.

$$I(x) = S(\nu)\cos(2\pi\nu x) \tag{1.1}$$

where $S(\nu)$ is the intensity of the monochromatic line located at the wavenumber $\nu = \lambda^{-1}$. In a more general case, when the emitted light is not monochromatic, the interferogram is given by

$$I(x) = \Re\left\{\int S(\nu)e^{-2\pi i\nu x}d\nu\right\} \tag{1.2}$$

To obtain the spectrum, it is necessary to measure I in correspondence of several values of x and calculate the real part of its Fourier Transform:

$$S(\nu) \propto \Re\left\{\int I(x)e^{2\pi i\nu x}dx\right\} \tag{1.3}$$

It is important to have a precise measurement of x before measuring $I(x)$. For this reason, the moving mirror is mounted on a step-motor controlled by an electronic board (TC-20, Bruker Optics) (hereafter called *mirror-board*). The monochromatic light of a He-Ne laser enters continuously into the interferometer. The interference of the He-Ne laser light at the exit of the interferometer is read by a photodiode sensitive in the visible region. The output of the photodiode is sent to the mirror-board that stops the mirror only in the positions for which a maximum or a minimum of interference is measured, i.e. for $2x = \frac{\lambda^*}{2}$, where $\lambda^* = 633$ nm is the emission wavelength of the He-Ne laser. The positions x at which the intensity I can be measured are

$$\ldots, L - n \cdot \frac{\lambda^*}{4}, L - (n-1) \cdot \frac{\lambda^*}{4}, \ldots, L - \frac{\lambda^*}{4}, L, L + \frac{\lambda^*}{4}, \ldots,$$

$$\ldots, L + (n-1) \cdot \frac{\lambda^*}{4}, L + n \cdot \frac{\lambda^*}{4}, \ldots$$

where n is a natural number.

For these values of x, the intensity I of the infrared light at the exit of the interferometer is measured by an InGaAs photodiode (G5832-05, EG&G), kept at room temperature. The diameter of the photodiode is 5 mm. Its quantum efficiency is given in figure 1.14. In figure 1.15, we report the electronic configuration of the read out system. The photodiode is biased by means of a reverse voltage of +1.5 V and of a 10 MΩ resistance (nominal value). With this set up, the nominal dark current is of the order of 10 nA and the nominal capacitance is approximately 3.5 nF.

The output of the photodiode passes through a 4.7 nF capacitance (nominal value) and enters into a charge amplifier[Bac-86]. The integration factor of the charge amplifier is equal to 0.25 mV/fC and its decay constant is 400 μs. The charge amplifier is connected to a shaper amplifier (EG&G, Ortec 575A), whose shaping time is 3 μs. Its gain can be adjusted from 2 to 100. In figure 1.15 we show a typical signal obtained in correspondence of an electron bunch.

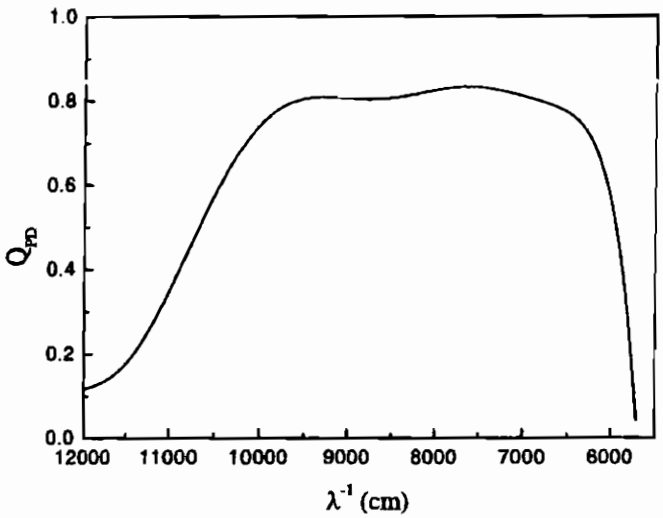

Figure 1.14: Quantum efficiency of the InGaAs photodiode.

This signal is sent to an electronic board (PAD82a, Bruker Optics) (hereafter called *mother-board*) installed into a personal computer and connected to the mirror-board. The mother-board performs a fast analog-to-digital conversion of the signal and stores on the computer the value of x (sent by the mirror-board) and the digital value of $I(x)$[††].

For the measurement of the complete interferogram, we use the so-called *Step Scan Technique*, that proceeds according to the following scheme.

1. The mother-board orders the mirror-board to put the moving mirror in its innermost position $x = L - x_m$.

2. The electron gun shoots one electron bunch.

[††]The AD conversion is quite complicated. In this contest, however, we just underline that the digital number $I(x)$ is proportional to the maximum of the signal $I(t; x)$ reported in figure 1.15

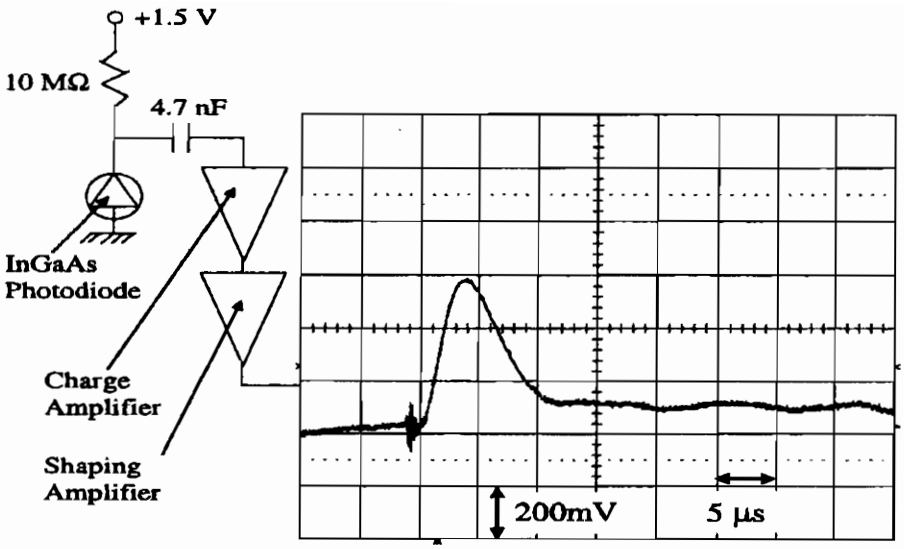

Figure 1.15: Scheme of the electronic read-out system of the InGaAs photodiode.

3. The mother-board performs the AD conversion of the signal coming from the infrared photodiode.

4. Steps 2 and 3 are repeated for N_m times to increase the signal-to-noise ratio. N_m is given by the user before starting the spectrum measurement.

5. The mother-board stores on the computer x and the average of $I_1(x), \ldots, I_{N_m}(x)$.

6. The mother-board orders the mirror-board to put the moving mirror one step forward $x = x + s$, where s is a multiple of $\frac{\lambda^*}{4}$ depending on the resolution and on the spectral range required by the user. The better the resolution required or the larger the spectral range spanned, the smaller is s.

7. Steps 2 to 6 are repeated until the moving mirror arrives to its outermost position $x = L + x_m$. For $x = L + x_m$, only

steps 2 to 5 are repeated.

In this way, at the end of the acquisition, the user has a discrete interferogram:

$$I(L - x_m), I(L - x_m + s), \ldots, I(L), \ldots, I(L + x_m - s), I(L + x_m)$$

The choice of N_m, of the resolution and of the spectral range deserves a comment. In principle, the maximum resolution is 0.1 cm^{-1} and the spectral range is between 5000 cm^{-1} and 15000 cm^{-1}. In this case, even with $N_m = 1$, the acquisition of the spectrum would take several hours because the number of steps is equal to $N_{step} = 568000$. This is not realistic not only for practical reasons, but also for technical problems. If the acquisition is too long, in fact, long term instabilities of the electron beam intensity introduce a fluctuation of the infrared signal amplitude not connected to the interferogram features. Usually, a compromise is reached for $N_m \simeq 50$ and $N_{step} \simeq 568$. For these values, one obtains a low noise spectrum in ten minutes. For $N_{step} = 568$ and spectral range between 5000 cm^{-1} and 15000 cm^{-1}, the resolution is 100 cm^{-1}. Without changing N_m and N_{step}, hence without increasing the measuring time, better resolutions can be achieved in a spectral region of interest by reducing the spectral range.

The deconvolution of the interferogram to the spectrum is performed by a commercial software (Opus 3.3). A typical spectrum of an Argon-Xenon mixture is shown in figure 1.16. The spectra can be fitted with a Gaussian or a Lorentzian curve plus a baseline by means of the same commercial software, that uses the Levenberg-Marquardt algorithm for the minimization of the χ^2 estimator[Pre-92]. However, this program does not calculate the error on the fitting parameters. In the next chapter we describe what we have done in order to give an error estimate.

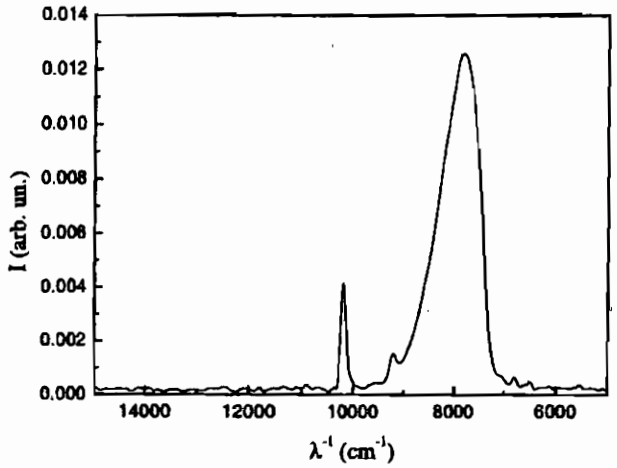

Figure 1.16: Fluorescent spectrum in Argon-Xenon mixture excited by the electron beam.

1.2 Calibrations and tests

The experimental apparatus has been tested with infrared scintillating crystals. We have irradiated a Al_2O_3(Ti) crystal, a YAG(Nd) and a YAG(Yb) crystal in this experimental set-up, and their well-known laser emission spectrum has been obtained[Bas-95, Buc-67]. In figure 1.17 we report, by way of example, the result obtained with a YAG(Yb) sample.

We have also tested and extended the fitting software in order to give an error estimate. We have written a Fortran77 program that performs the fit with the same algorithm of Opus 3.3. A complete agreement of the results of the two programs has been obtained. But in the homemade program an algorithm has been developed with the aim to calculate the statistical errors on the fitting parameters. Since the standard deviation of each point of the spectrum is not known (because the commercial program does not estimate it during the Fourier Transform procedure), we used

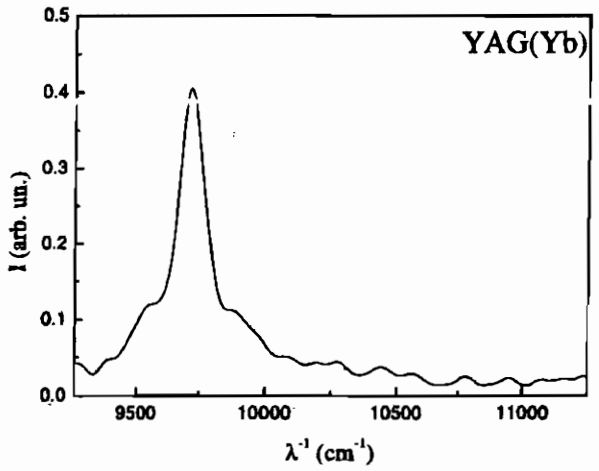

Figure 1.17: Fluorescent spectrum of YAG(Yb) excited by the electron beam.

an unweighted algorithm[Bev-92, Rot-01] that proceeds according to the following scheme:

1. The program minimizes, respect to the fitting parameters ξ_1, $\ldots,\xi_m$, the unweighted χ^2 estimator, defined by:

$$\chi^2 = \sum_i (y_i - f(x_i; \xi_1, \ldots, \xi_m))^2 \qquad (1.4)$$

   where y_i are the experimental values of the spectrum in correspondence of the wavelength number x_i, and f is the fitting function. The minimizing procedure is performed according to the Levenberg-Marquardt algorithm†.

2. Once the program has found the minimizing parameters $\tilde{\xi}_1$, $\ldots,\tilde{\xi}_m$, it calculates the standard deviation (assumed to be the same for all the points of the spectrum) by means of:

†Up to this point, the homemade program is equal to the commercial one

$$\sigma = \sqrt{\frac{\sum_i \left(y_i - f(x_i; \tilde{\xi}_1, ..., \tilde{\xi}_m)\right)^2}{(N-m)}} \tag{1.5}$$

where N is the number of the spectrum points.

3. Using this estimate for σ, the program calculates the covariance matrix in correspondence of $\tilde{\xi}_1, \ldots, \tilde{\xi}_m$.

The method is rigorously correct if two assumptions are satisfied: (i) the probability distribution of each spectrum point is Gaussian, and (ii) all the spectrum points have the same standard deviation. The first hypothesis is normally assumed by the users of the χ^2 estimator, but the second one is not always satisfied. However, we have no other means to estimate errors.

Chapter 2

Prompt spectra of particle induced infrared emission in noble gases.

Introduction

In this chapter we present and discuss the light spectra of prompt infrared emission induced by particles in noble gases.

We shall point out that the emission mechanism varies from species to species. For lighter gases (Helium, Neon and Argon), the spectrum is dominated by atomic emissions (although some other mechanisms could also be present). In Xenon, a broad band dominates over the wavelength region under investigation. We shall identify an excimer radiative transition as the origin of the emission observed. In Krypton, an excimer transition (on the wavelength edge of our detector sensitivity) is also present, but its intensity is of the same order of magnitude of the atomic emissions that also appear in the spectrum.

We also present a systematic study of the excimer transition observed in Xenon. As the density of the gas is increased, the spectrum is shifted towards higher wavelengths. The shift is explained using a simple model, that is tested on Argon-Xenon mixtures.

In section 1 we report the results of our measurements, presenting the spectra relative to all the species investigated. In the light of those results, we discuss the mechanism of emission. Section 2 is devoted to the study of the density dependence of Xenon spectra. We show the results and discuss our interpretative model. In section 3 we test the model on the results obtained with an Argon-Xenon mixture.

2.1 Particle induced infrared spectra in noble gases at nearly atmospheric pressure

2.1.1 Experimental results

In figures 2.1 to 2.5 we report the spectra of Helium, Neon, Argon, Krypton and Xenon, obtained with the experimental apparatus previously described, with a resolution of 100 cm^{-1} in the 5000 to 15000 cm^{-1} range. The samples were kept at room temperature and nearly atmospheric pressure.

The spectra show the following features:

- In Helium, Neon and Argon, the spectra are dominated by several sharp lines.
- In Krypton the spectrum is characterized by several sharp lines plus a broad band in the wavelength region above $\simeq$ 8000 cm^{-1}. Note that the red wing of the band lies in the wavelength region above $\simeq$ 6000 cm^{-1}, where the quantum efficiency of the InGaAs photodiode decreases dramatically.
- In Xenon the spectrum is dominated by a broad band centered about 7800 cm^{-1}. Less intense sharp lines are also present.

We repeated the measurements with a different set-up, irradiating the gas with a 5 MeV proton beam, and we obtained the same

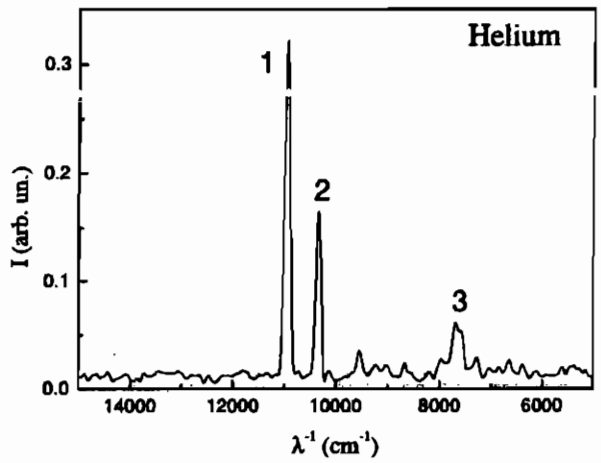

Figure 2.1: Spectrum of particle induced infrared emission in Helium at room temperature and nearly atmospheric pressure.

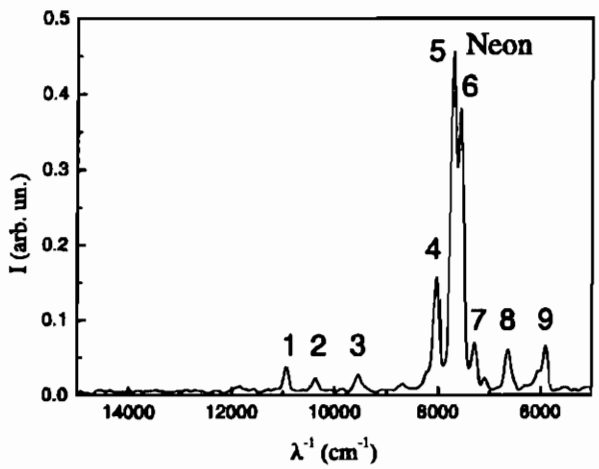

Figure 2.2: Spectrum of particle induced infrared emission in Neon at room temperature and nearly atmospheric pressure.

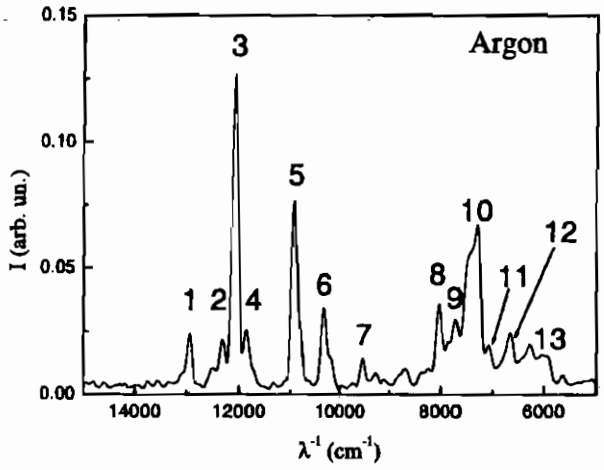

Figure 2.3: Spectrum of particle induced infrared emission in Argon at room temperature and nearly atmospheric pressure.

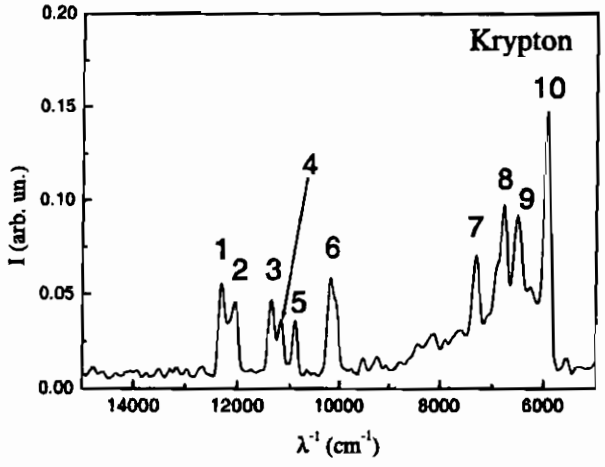

Figure 2.4: Spectrum of particle induced infrared emission in Krypton at room temperature and nearly atmospheric pressure.

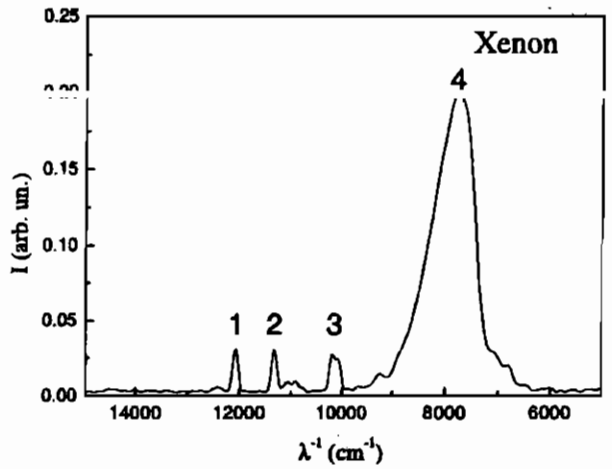

Figure 2.5: Spectrum of particle induced infrared emission in Xenon at room temperature and nearly atmospheric pressure.

results. Furthermore, the spectra do not depend on the amount of injected charge in the range explored (0.05 to 10 nC per bunch).

2.1.2 Discussion

The emission of infrared light in noble gases excited by ionizing particles is the result of the following processes (see figure 2.6).

- The 100 keV electrons produce excited atoms and ion-electron pairs. Ionization electrons also scatter inelastically against the atoms, giving rise to further atomic excited states and ion-electron pairs, until the energy of the electrons becomes lower than the first excitation level. Then the electrons thermalize reaching an equilibrium configuration in which their mean energy is equal to the thermal energy of the gas atoms.

- Most of the ion-electron pairs recombine, giving rise to other excited atoms.

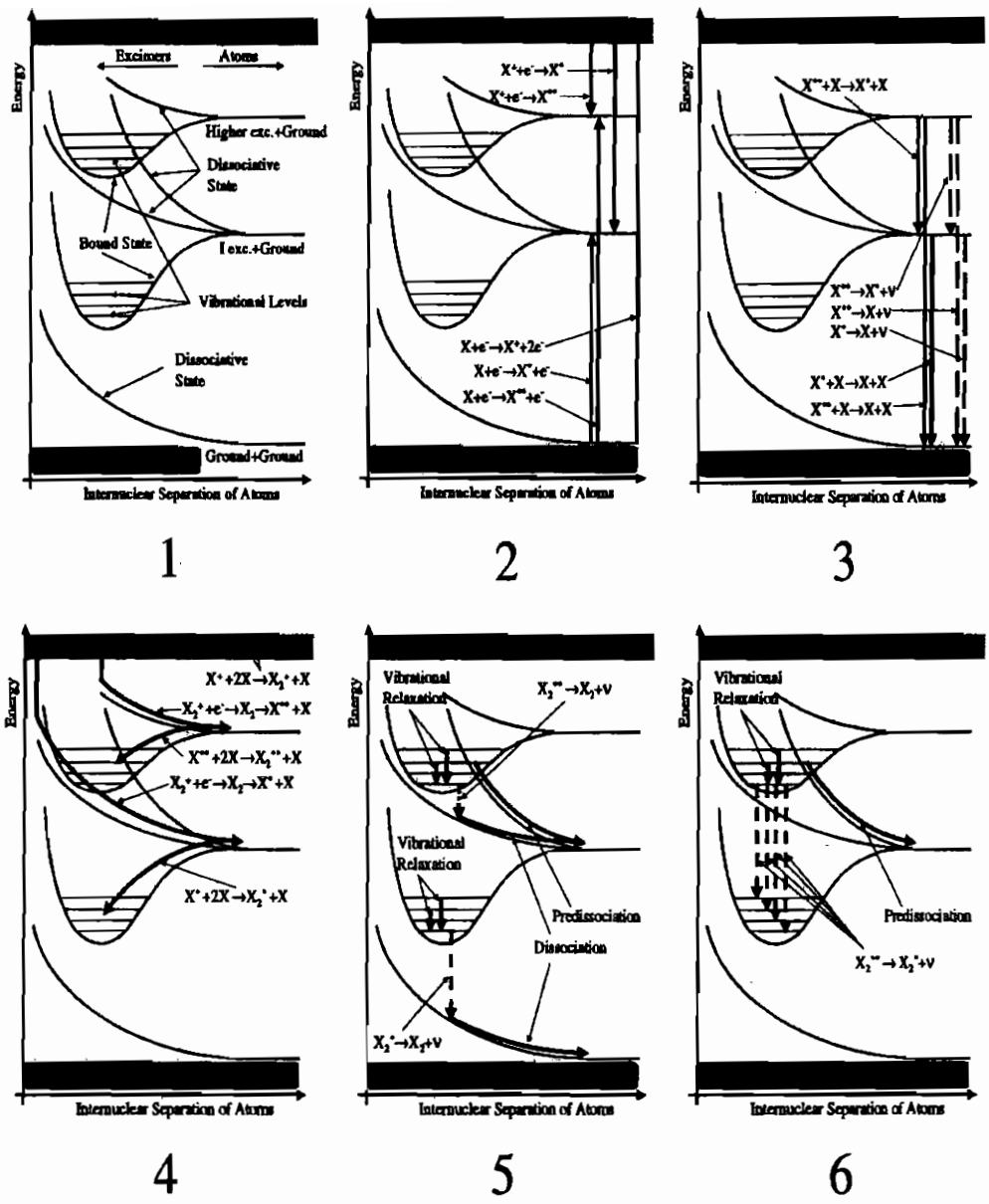

Figure 2.6: A schematic view of the main kinetic processes induced by the passage of ionizing particles into a gas.

- At this point, the gas contains a huge number of excited atoms[†] that relax towards the ground state by means of: (i) collisional non-radiative de-excitation, or (ii) radiative decays.

- As the pressure of the sample is higher than the atmospheric pressure, three bodies processes also take place[Bra-79]. Thus, excited and ionized atoms can also give rise to bound excimer states by means of the following reactions:

$$X^+ + 2X \longrightarrow X_2^+ + X \tag{2.1}$$

$$X_2^+ + e^- \longrightarrow X_2 \longrightarrow X^* + X \tag{2.2}$$

$$X^* + 2X \longrightarrow X_2^* + X \tag{2.3}$$

where X is a neutral atom in its ground state, X^+ is an atomic ion, X_2^+ is a molecular ion, X^* is an excited atom, and X_2^* is an excimer state. The X^* state can be populated by direct excitation as well.

Among the X_2^* states, for example, the $^1\Sigma_u^+$ and $^3\Sigma_u^+$ levels are populated, and their de-excitation towards the $^1\Sigma_g^+$ repulsive molecular ground state gives rise to the well known vacuum-ultraviolet excimer emission (see Introduction). But also higher bound excimer states can be formed as well[Mul-70], that can de-excite either through (i) a radiative decay towards a dissociative excimer state (the so-called *bound-free transition*), (ii) a radiative decay towards another bound state (the so-called *bound-bound transition*), or (iii) a non-radiative pathway. Note that, since we are dealing with samples at relatively high pressure, it is assumed that vibrational relaxation is rapid prior to the excimer decay[Bra-79, Pol-81, Mus-94].

[†]The number of the excited atoms depends on the gas sample and on the energy of the ionizing particle. This will be discussed in the following chapters.

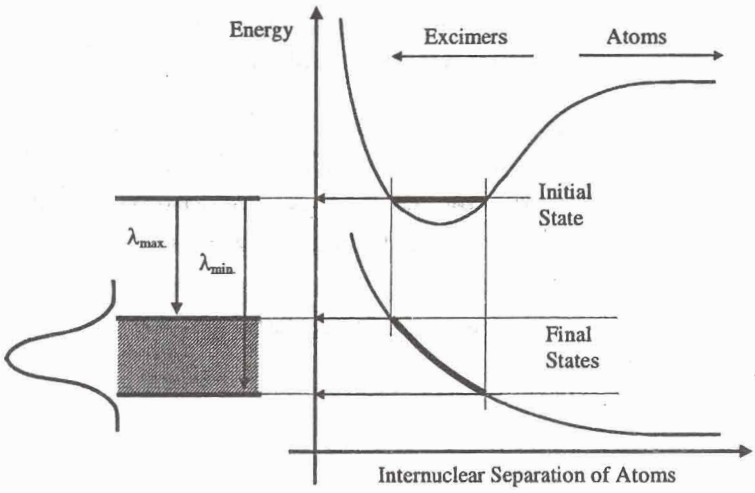

Figure 2.7: A schematic view of a bound-free transition.

According to the scheme described above, infrared light emission can be ascribed either to (i) radiative decays of excited atoms, (ii) bound-free excimer decays, or (iii) bound-bound excimer decays. In the first case, the spectrum is characterized by an isolated sharp line. In the second case, on the contrary, a broad band is expected, because the transition involves a broad continuum of final energetic states (see figure 2.7). In the third case, the main feature of the spectrum is a series of several lines, corresponding to different overtones of the same transition (see figure 2.8).

Following this scheme, it can be argue that in Helium, Neon and Argon atomic decays dominate over other radiative mechanisms. It is however important to underline that the resolution of our spectra is not high enough to rule out the hypothesis that the structures (4-7) in Neon (figure 2.2) and (8-13) in Argon (figure 2.3) are generated by bound-bound transitions. A detailed study at much lower densities is necessary in order to confirm or reject this hypothesis.

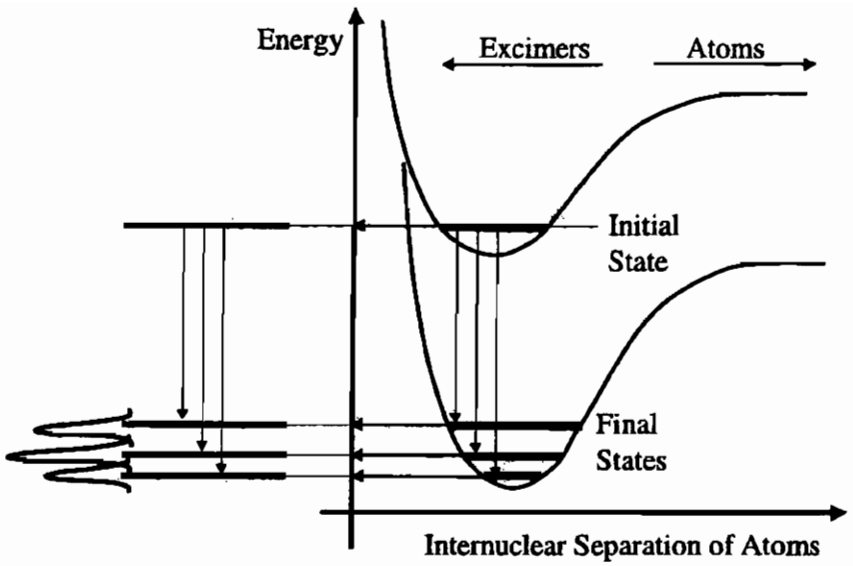

Figure 2.8: A schematic view of a bound-bound transition.

At lower densities, in fact, the vibrational relaxation of the initial state is slower than the excimer decay time. Thus the spectrum structure should contain a higher number of lines corresponding to transitions in which the initial state is vibrationally excited.

The spectrum of Xenon is dominated by a broad band, that we assign to a bound-free transition among highly excited excimer states. Also some atomic lines of lower intensity are present.

In Krypton, several atomic transitions characterize the spectrum, together with a broad band presumably peaked above 6000 cm^{-1}, and thus only partially detected in our spectrum range. Also this broad band can be ascribed to a bound-free transition among highly excited excimer state.

In table 2.1 to 2.7 we report the list of the wavelengths of the sharp emission lines estimated from our spectra. Comparing those values with the wavelength of the optical transitions[Mar-99, Str-68], we tentatively assign the lines observed in our experiment

Helium	
Line (cm^{-1})	Transition
(1) 10950	$3p\ ^3P_{0,1,2}$ - $8d\ ^3D_{1,2,3}$ $3d\ ^3D_{0,1,2}$ - $9f\ ^3F_{2,3,4}$
(2) 10350	$3s\ ^1S_0$ - $6p\ ^1P_1$ $3p\ ^3P_{0,1,2}$ - $7s\ ^3S_1$
(3) 7655	$3d\ ^3D_{1,2,3}$ - $5p\ ^3P_{0,1,2}$ $3p\ ^1P_1$ - $5d\ ^1D_2$ $3p\ ^3P_{0,1,2}$ - $5s\ ^3S_1$ $3d\ ^3D_2$ - $5f\ ^1F_3$ $3d\ ^3D_{1,2,3}$ - $5f\ ^3F_{2,3,4}$ $3d\ ^3D_3$ - $5f\ ^3F_2$

Table 2.1: Tentative assignment of atomic transitions to the lines observed in the Helium spectrum[Mar-99, Str-68].

to known atomic levels[††]. The assignment is not unique because our resolution is rather poor. Furthermore, it is well known that the intensity of the lines in a beam excited sample is rather different respect to optical or discharge experiments[Pol-81, Lin-88a]. Thus we can not refer to the intensity reported in literature because those results were obtained with the latter technique. It is interesting to note that in Neon no known transition matches the wavelength corresponding to transition (7), suggesting that this line could arise from a bound-bound transition.

Concerning the excimer emissions, we can only analyze the spectrum of Xenon. In this case, in fact, the spectrum is dominated by this transition and the broad band is completely contained in the wavelength region of high quantum efficiency of the InGaAs photodiode.

[††]The notation *Observed-Unclassified* means that the lines have been already observed with other techniques, but have not yet a precise assignment.

Neon	
Line (cm^{-1})	Transition
(1) 10940	$3d\,[7/2]_{3,4}$ - $9f\,[9/2]_4$ $3p'\,[3/2]_1$ - $3d\,[5/2]_2$ $3p'\,[3/2]_1$ - $3d\,[3/2]_1$
(2) 10370	$3s'\,[1/2]_1$ - $6p\,[1/2]_0$ $4s'\,[1/2]_0$ - $6p\,[1/2]_1$ $3p\,[1/2]_1$ - $4s\,[3/2]_2$
(3) 9545	$4s\,[3/2]_1$ - $5p'\,[3/2]_2$ $3p'\,[1/2]_0$ - $5d'\,[3/2]_1$
(4) 8045	$3p'\,[3/2]_1$ - $4s\,[3/2]_1$ $3d\,[1/2]_{0,1}$ - $5f\,[3/2]_1$
(5) 7710	$3p'\,[1/2]_1$ - $4s\,[3/2]_1$ $3p'\,[3/2]_2$ - $4s\,[3/2]_2$
(6) 7570	$3p'\,[1/2]_1$ - $4s\,[3/2]_2$
(7) 7300	Unclassified
(8) 6650	$4p\,[5/2]_{2,3}$ - $5d\,[7/2]_{3,4}$ $4p'\,[3/2]_{1,2}$ - $5d'\,[3/2]_{1,2}$ $4p'\,[3/2]_{1,2}$ - $5d'\,[5/2]_{2,3}$ $4p\,[5/2]_2$ - $5d\,[5/2]_{2,3}$ $4p'\,[1/2]_1$ - $5d'\,[3/2]_1$ $4p'\,[1/2]_1$ - $5d'\,[5/2]_2$
(9) 5915	$4p\,[3/2]_{1,2}$ - $6s\,[3/2]_1$ $3d\,[3/2]_1$ - $5p\,[5/2]_2$ $3d'\,[3/2]_2$ - $5p'\,[1/2]_1$ $3p'\,[3/2]_1$ - $5d\,[1/2]_1$

Table 2.2: Tentative assignment of atomic transitions to the lines observed in the Neon spectrum[Mar-99, Str-68].

Argon	
Line (cm^{-1})	Transition
(1) 12935	$4s\,[3/2]_2$ - $4p\,[3/2]_1$ $3s'\,[1/2]_0$ - $4p'\,[1/2]_1$
(2) 12310	$4p'\,[3/2]_2$ - $6s\,[3/2]_2$ $4s\,[3/2]_1$ - $4p\,[3/2]_1$ $4s\,[3/2]_2$ - $4p\,[5/2]_3$ $4p'\,[1/2]_1$ - $6s\,[3/2]_1$
(3) 12085	$4s'\,[1/2]_1$ - $4p'\,[1/2]_1$
(4) 11865	$4s'\,[1/2]_1$ - $4p'\,[3/2]_2$ $4s\,[3/2]_1$ - $4p\,[5/2]_2$ $4p'\,[3/2]_1$ - $4d\,[3/2]_2$
(5) 10935	$4s\,[3/2]_2$ - $4p\,[1/2]_1$ $4p\,[1/2]_1$ - $5s'\,[1/2]_1$
(6) 10335	$4s\,[3/2]_1$ - $4p\,[1/2]_1$
(7) 9535	$4s'\,[1/2]_0$ - $4p\,[1/2]_1$ $4p\,[1/2]_1$ - $5s\,[3/2]_1$ $3d\,[3/2]_2$ - $4f'\,[5/2]_{2,3}$
(8) 8030	$4p\,[5/2]_{2,3}$ - $5d\,[5/2]_{2,3}$ $3d\,[3/2]_2$ - $4f\,[5/2]_{2,3}$ $4p\,[3/2]_1$ - $3d\,[3/2]_1$ $4p\,[1/2]_1$ - $5d\,[3/2]_2$ $4p\,[5/2]_{2,3}$ - $5s\,[3/2]_{1,2}$ $4p\,[1/2]_0$ - $5s'\,[1/2]_1$ $4p'\,[1/2]_1$ - $5d'\,[3/2]_1$ $4p'\,[3/2]_1$ - $5s'\,[1/2]_1$
(9) 7710	$4p'\,[3/2]_{1,2}$ - $5s'\,[1/2]_0$ $4p\,[1/2]_1$ - $3d\,[1/2]_1$

Table 2.3: Tentative assignment of atomic transitions to the lines observed in the Argon spectrum[Mar-99, Str-68].

Argon (cont.)	
Line (cm^{-1})	Transition
(10) 7345	$4p\,[1/2]_1$ - $3d\,[1/2]_0$ $4p\,[3/2]_{1,2}$ - $5s\,[3/2]_{1,2}$ $4p'\,[3/2]_{1,2}$ - $3d\,[5/2]_{2,3}$ $4p'\,[1/2]_1$ - $5s'\,[1/2]_{1,0}$ $3d\,[7/2]_4$ - $4f\,[9/2]_{4,5}$ $4p\,[5/2]_2$ - $3d\,[7/2]_3$ $4p\,[3/2]_1$ - $3d\,[5/2]_2$
(11) 7085	$4p'\,[1/2]_1$ - $3d\,[3/2]_2$
(12) 6665	$4p\,[3/2]_2$ - $3d\,[7/2]_3$ $5s\,[3/2]_2$ - $4f\,[5/2]_{2,3}$ $5s\,[3/2]_2$ - $4f\,[3/2]_{1,2}$ $4p'\,[1/2]_0$ - $3d'\,[3/2]_1$ $4p\,[1/2]_0$ - $5s\,[3/2]_1$ $3d\,[5/2]_3$ - $4f\,[7/2]_{3,4}$ $4p\,[5/2]_2$ - $3d\,[3/2]_2$
(13) 6400-5850	$4p'\,[3/2]_{1,2}$ - $5s\,[3/2]_{1,2}$ $3d\,[3/2]_2$ - $5p'\,[1/2]_1$ $4d'\,[3/2]_1$ - $4f'\,[5/2]_2$ $4p'\,[1/2]_0$ - $5s'\,[1/2]_1$ $4p\,[5/2]_2$ - $3d\,[1/2]_1$ $4p'\,[1/2]_1$ - $5s\,[3/2]_{1,2}$ $3d\,[3/2]_1$ - $4f\,[5/2]_2$ $4p\,[3/2]_{1,2}$ - $3d\,[3/2]_2$ $3d\,[3/2]_1$ - $4f\,[3/2]_{1,2}$

Table 2.4: Tentative assignment of atomic transitions to the lines observed in the Argon spectrum[Mar-99, Str-68] (cont.).

Krypton	
Line (cm^{-1})	Transition
(1) 12300	$5s'[1/2]_0$ - $5p'[3/2]_1$ $5s[3/2]_2$ - $5p[5/2]_{2,3}$ $5p'[3/2]_2$ - $5d'[5/2]_3$ $5s[3/2]_1$ - $5p[3/2]_2$ $4d[3/2]_2$ - $6f[5/2]_3$
(2) 12075	$4s'[1/2]_1$ - $5p'[3/2]_2$ $5p[3/2]_2$ - $5d[5/2]_3$ $5s'[1/2]_1$ - $5p'[1/2]_1$ $5s[3/2]_1$ - $5p[3/2]_1$
(3) 11365	$5p[5/2]_3$ - $4d'[5/2]_3$ $5s[3/2]_1$ - $5p[5/2]_2$
(4) 11185	$5s[3/2]_2$ - $5p[1/2]_1$
(5) 10900	Observed-Unclassified
(6) 10155	$5s[3/2]_1$ - $5p[1/2]_1$ $5p[3/2]_2$ - $4d'[3/2]_2$
(7) 7315	$5p[5/2]_2$ - $4d[3/2]_1$ $5p[5/2]_2$ - $6s[3/2]_{1,2}$ $5p'[3/2]_1$ - $4d'[3/2]_1$
(8) 6780	Observed-Unclassified
(9) 6510	$5s[1/2]_1$ - $5p[5/2]_2$ $5p[3/2]_2$ - $6s[3/2]_2$ $5p[1/2]_1$ - $4d[3/2]_2$ $5p[3/2]_2$ - $4d[3/2]_1$ $5p[5/2]_{2,3}$ - $5d[5/2]_2$

Table 2.5: Tentative assignment of atomic transitions to the lines observed in the Krypton spectrum[Mar-99, Str-68].

Krypton (cont.)	
Line (cm^{-1})	Transition
(10) 5940	$5s'\,[1/2]_0$ - $5p\,[1/2]_1$ $5p\,[3/2]_2$ - $4d\,[5/2]_3$ $5p\,[5/2]_3$ - $4d\,[7/2]_3$ $5p\,[1/2]_1$ - $4d\,[1/2]_1$ $5p\,[3/2]_1$ - $4d\,[5/2]_2$ $5p'\,[1/2]_1$ - $5d\,[1/2]_1$

Table 2.6: Tentative assignment of atomic transitions to the lines observed in the Krypton spectrum[Mar-99, Str-68] (cont.).

Xenon	
Line (cm^{-1})	Transition
(1) 12075	$6p\,[3/2]_2$ - $5d'\,[3/2]_2$ $5d\,[1/2]_1$ - $8p\,[5/2]_2$ $6s'\,[1/2]_0$ - $6p'\,[3/2]_1$ $6s\,[3/2]_2$ - $6p\,[3/2]_2$ $6s'\,[1/2]_1$ - $6p'\,[1/2]_1$ $6s\,[3/2]_1$ - $6p\,[1/2]_1$
(2) 11325	$6p\,[5/2]_2$ - $6d\,[5/2]_3$ $6s\,[3/2]_2$ - $6p\,[5/2]_3$ $6p\,[1/2]_1$ - $6d\,[1/2]_{0,1}$
(3) 10135	$6s\,[3/2]_1$ - $6p\,[5/2]_2$

Table 2.7: Tentative assignment of atomic transitions to the lines observed in the Xenon spectrum[Mar-99, Str-68].

The wavelength band of the Xenon excimer emission (4) (see figure 2.5) is centered at about 7800 cm^{-1}. This value roughly corresponds to the energy difference between the stable excimer levels correlated to the $6p'$ dissociation limit, and the energy level of the dissociative excimer states correlated to the $6s$ dissociation limit[Mul-70, Bow-86] (see figure 2.9). We ascribe the broad band to the radiative decay from the former states to the latter. However, other excimer transitions could be partially or totally responsible for the emission observed (for example the transition from a bound state correlated to the $6p$ dissociation limit towards the mainly dissociative states associated to the $6s$ dissociation limit[Mul-70, Bow-86]). Note that the possibility that some atomic lines might be obscured under the broad continuum can not be ruled out.

It is interesting to note that, among the atomic transitions that characterized Xenon spectrum, we have identified both $6p'$ to $6s'$ (line (1)) and $6p$ to $6s$ (lines (1), (2), and (3)) decays. The former are due to those atoms in the $6p'$ state that radiatively decay towards the $6s'$ state before forming the corresponding excimer molecule. In the latter, the $6p$ levels are populated both by (i) direct excitation, (ii) de-excitation of higher atomic excited states, and (iii) predissociation of the excimer state that could be responsible of the broad band observed[Ket-97] (see figure 2.9). Then, the $6s$ excited atoms form the $^1\Sigma_u^+$ and $^3\Sigma_u^+$ excimer molecules, whose de-excitation towards the $^1\Sigma_g^+$ repulsive molecular ground state gives rise to the well known second continuum.

2.2 Particle induced infrared spectra in gaseous Xenon as a function of pressure

2.2.1 Experimental results

In Xenon, we observed an interesting phenomenon related to different values of the gas pressure. In figure 2.10 we report the spectra

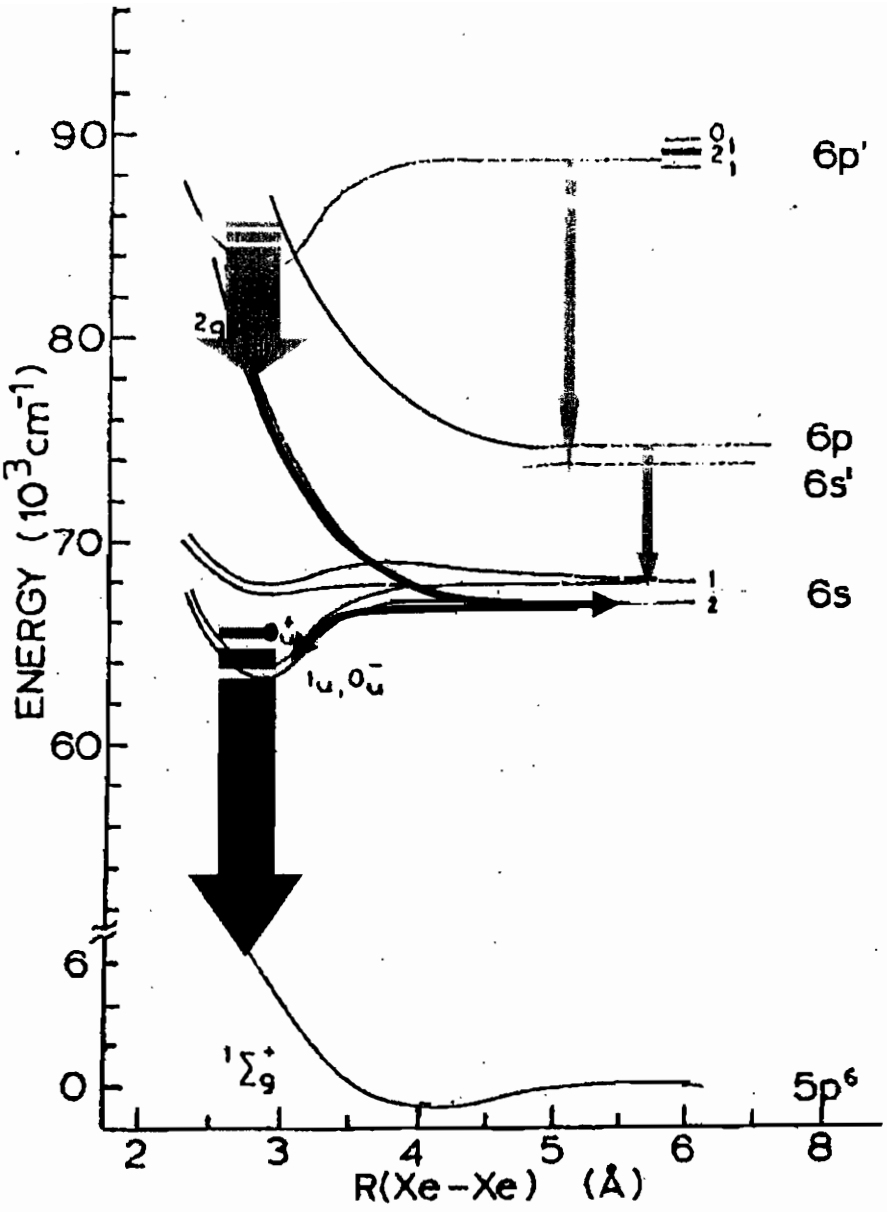

Figure 2.9: A simplified diagram of one of the possible emission pathway in Xenon[Mul-70, Bow-86].

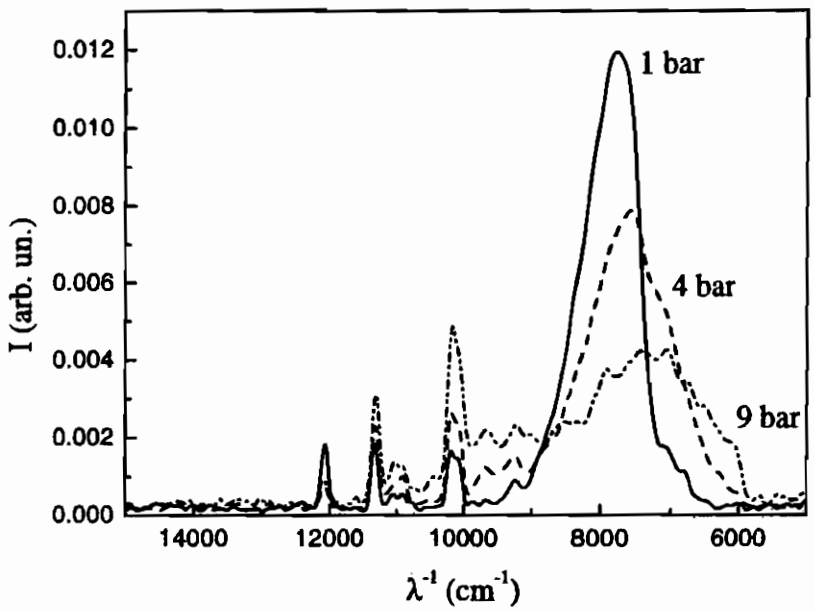

Figure 2.10: Xenon spectra at three different pressures.

obtained at three different pressures. The spectra were obtained with the same technique as before. Three effects of pressure on the excimer band can be outlined:

- The position of the centroid X_c is shifted to higher wavelengths as the pressure is increased.
- The width Δ increases as the pressure is increased.
- The ratio between its intensity and the intensity of the atomic lines decreases as the pressure is increased.

In figure 2.11 and 2.12 we show the result of a lorentzian and gaussian fit of the excimer band (pressure=1 bar), obtained with

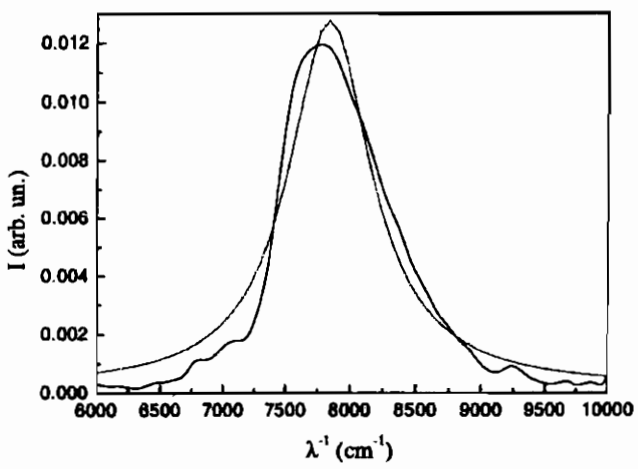

Figure 2.11: Lorentzian fit of the excimer band observed in Xenon (P=1 bar).

the unweighted fitting technique described in Chapter 1. It is evident that the neither lorentzian or gaussian shapes are suitable in order to fit the data. Thus, we used a different method. We fitted the broad bands with 3^{rd}-order polynomial functions and took the position of the maximum of the fitting functions as the best value of X_c. Since the results depend on the choice of the interpolation extremes, we repeated the interpolation procedure several times for all the spectra, changing each time the extremes. The values reported in figure 2.13 are the averages of the results of those fits, and the error bars are the standard errors.

In order to estimate Δ for each of the polynomial interpolating curves we took as a reference the maximum of the fitting function and estimated the *Full Width Half Maximum* (FWHM) using the measured spectra, hence we estimated Δ by averaging these results. In figure 2.14 we report the results of this procedure.

In order to give an estimate of the ratio between the intensities of the atomic lines I_{at} and the excimer band I_{exc}, we simply calcu-

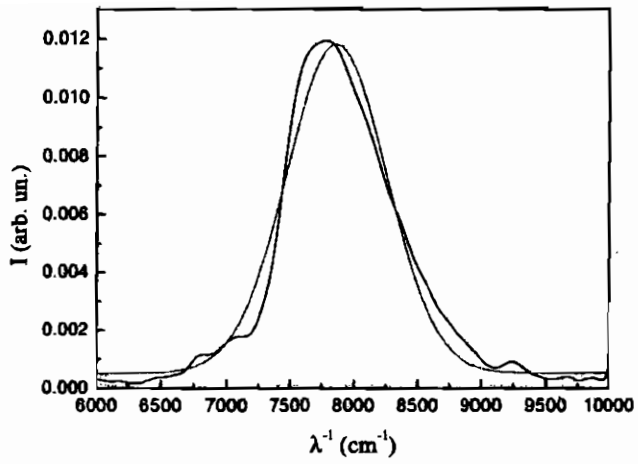

Figure 2.12: Gaussian fit of the excimer band observed in Xenon (P=1 bar).

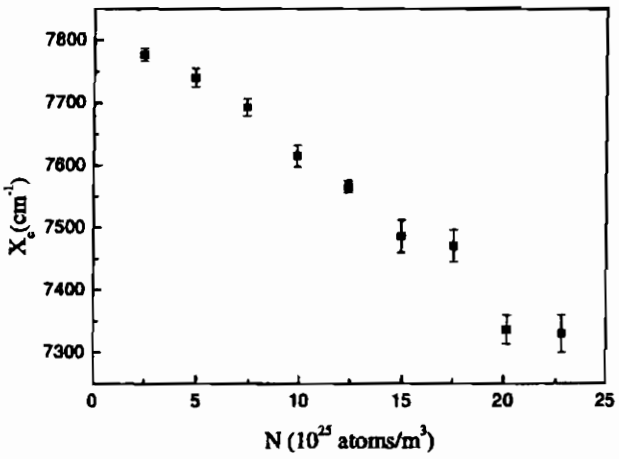

Figure 2.13: Red shift of the excimer band as a function of Xenon density.

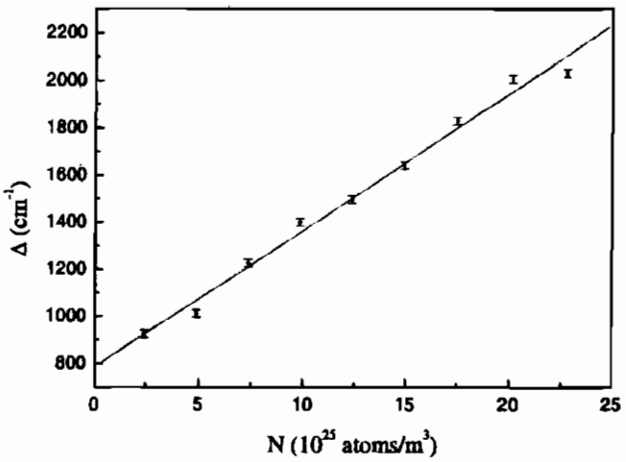

Figure 2.14: Broadening of the excimer band as a function of Xenon density. The line is only a guide for eyes.

lated the area of the spectrum under the range between 5000 cm^{-1} and 9500 cm^{-1} (where the excimer band dominates) and that in the range between 9500 cm^{-1} and 14000 cm^{-1} (where atomic lines dominate). The results are reported in figure 2.15. The error bars are due to the uncertainties in the choice of the integration intervals and are approximately equal to 15%.

We also calculated the ratio between the three atomic lines observed in Xenon as a function of pressure. To do that, we interpolated the lines with loretzian curves by means of the fitting procedure explained in Chapter 1. In figure 2.16 we show the area of each line $I_n(i)$, normalized in such a way that $I_n(1) + I_n(2) + I_n(3) = 1$, as a function of the gas density.

2.2.2 Discussion

The most important feature of the observed broad band is its large density-dependent red shift. A similar shift of the emission maxi-

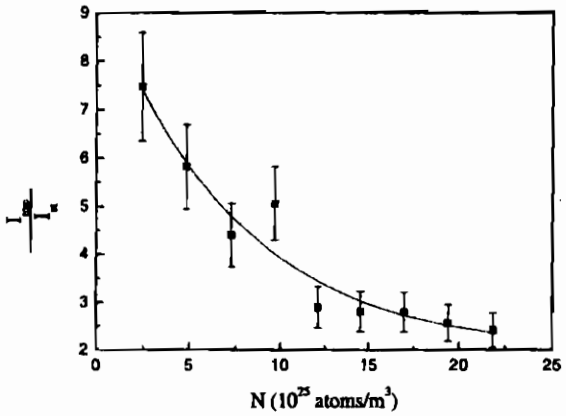

Figure 2.15: Ratio between the excimer band intensity (I_{exc}) and the atomic lines intensity (I_{at}) as a function of Xenon density. The line is only a guide for eyes.

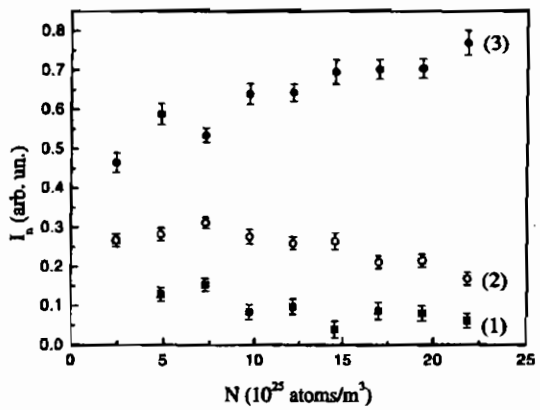

Figure 2.16: Normalized intensity of the atomic lines observed in Xenon as a function of density. The normalization is such that $I_n(1) + I_n(2) + I_n(3) = 1$.

mum has been observed in the same density range for the second vacuum-ultraviolet continuum in Xenon[Koe-74], even though the maximum relative shift ($\simeq 1\%$) is comparable with the experimental accuracy of the data. In this case, however, the density dependence of the width of the vacuum ultraviolet second continuum is opposite with respect to the present case because the FWHM decreases almost linearly by $\simeq 15\%$ in the same pressure range of our experiment. The narrowing of the vacuum ultraviolet continuum has been tentatively explained in terms of an absorption in a ground state population that increases with increasing pressure and this fact would be also responsible for the small red shift observed.

It is also known that atomic lines of noble gases exhibit a similar behavior[Sch-85, Ray-84, Mes-77a, Mes-77b, Mes-77c, Lap-75], although the observed shifts show a density dependence nearly two orders of magnitude lower than the shift of the excimer band reported in figure 2.13. The atomic red shift is usually explained either in terms of density-dependent local-field corrections in the classical dispersion theory[Lap-75], or in terms of the Margenau's statistical theory of spectral shift and line broadening[Mar-35, Mar-51, Mes-77c]. Both the approaches are in good agreement with the experimental data. Thus they are far from describing larger red shifts, as in the case of the present experimental results. By way of example, in figures 2.17 and 2.18 we report the red shift of the lines (2) and (3) of our spectra, obtained by interpolating the lines with lorentzian curves. The error bars are the statistical errors calculated using the procedure described in Chapter 1. The lines in the figures are the results of the linear best fits. The slopes are of the same order of magnitude (10^{-24} m^2) of that observed in other experiments for other atomic lines in a smaller density range.

In order to explain the large difference in the density dependence of the spectra for the excimer band and the atomic lines, we start observing that the electronic structure of homonuclear excimers can be quite accurately described by an ionic molecular core and an electron in a diffuse Rydberg orbital much larger in diameter than internuclear distance[Ara-78, Aud-91]. Such state can exist even

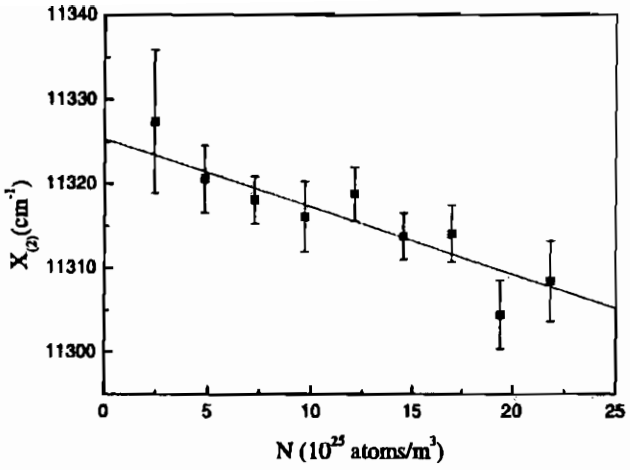

Figure 2.17: Red shift of the line (2) as a function of Xenon density. The line is the result of the linear best fit.

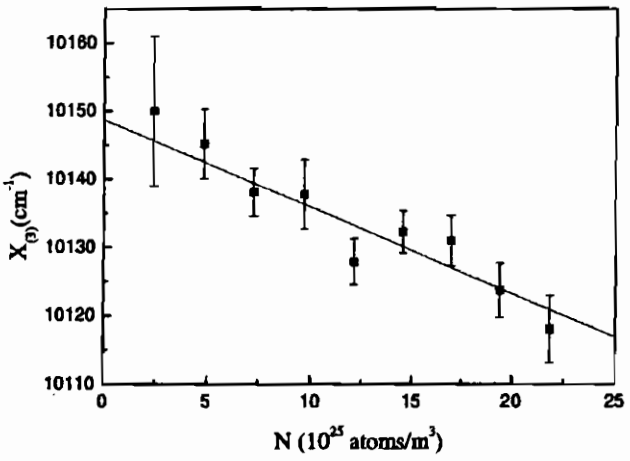

Figure 2.18: Red shift of the line (3) as a function of Xenon density. The line is the result of the linear best fit.

in high pressure environment provided that the Rydberg electron is weakly scattered off by the gas atoms, or, in other words, if the electron mean free path is much larger than the radius of the orbit of the Rydberg state. In a moderately dense gas, as in the present case, this condition is fulfilled because the electron mean free path is several nanometers long[Hua-78]. Bearing in mind this picture, we will now show that the red shift of the excimer band can be describe considering the effects of the neighboring gas atoms (hereafter *host gas*) on the energy of the outermost electron of the Rybderg-like excimer systems responsible for the emission observed.

We first assume that the energy states of the outermost electron of an excimer isolated molecule are given by the solution of the hydrogen-like Schroedinger equation:

$$\left(-\frac{\hbar^2}{2m}\nabla^2 - \frac{e^2}{4\pi\epsilon_0 r}\right)\psi = E\psi \tag{2.4}$$

where $\hbar$ is the Plank constant h divided by 2π, m is the electron mass, e is the electron charge, and ϵ_0 is the vacuum permittivity. When the excimer is surrounded by the atoms of the host gas, the Schroedinger equation must be corrected considering two different effects, that we will conventionally call (i) *Fermi contribution*, and (ii) *polarization contribution.*

The Fermi contribution* is due to the fact that the outermost electron, of the excimer, during its orbital motion, interacts with the host atoms. Locally, this interaction is very strong and can not be neglected in the Schroedinger equation, that must be re-written in the following form:

$$\left(-\frac{\hbar^2}{2m}\nabla^2 - \frac{e^2}{4\pi\epsilon_0 r} + \sum_i V_i(\mathbf{R}_i)\right)\psi = E\psi \tag{2.5}$$

where $V_i(\mathbf{R}_i)$ is the interaction potential beween the outermost electron of the excimer and the $i-$th atom located in $\mathbf{R}_i$. It has been

*We have called this contribution *Fermi contribution* because its value was firstly calculated by Enrico Fermi in 1934[Fer-34]

calculated that, due to this contribution, the energy of the outermost electron is shifted by[Fer-34]:

$$V_0(N) = \frac{2\pi\hbar}{m} Na \tag{2.6}$$

where N is the density of the gas and a is the scattering length for the interaction of the slow outermost electron with an atom of the host gas. Since for attractive electron-atom potentials (as in the case of Xenon) $a < 0$, an increase of the host gas density corresponds to a decrease of the energy eigenvalues.

The polarization contribution is due to the fact that the host atoms contained in the orbital of the outermost electron of the excimer partially screen the Coulombian potential. In order to calculate this contribution, we now assume that the excimer state can be treated in the same way as Wannier-Mott excitons are dealt with in liquids or solids[Sch-85, Raz-70, Ric-66]. Wannier excitons are related to high extravalence excitations[‡] of atomic impurities, whose energy is comparable to the energy of the excimer states involved in the transition under investigation. Accordingly, we can take into account this contribution by simply using in equation 2.5 the host gas permittivity ϵ instead of ϵ_0:

$$\left(-\frac{\hbar^2}{2m}\nabla^2 - \frac{e^2}{4\pi\epsilon r} + \sum_i V_i(\mathbf{R}_i)\right)\psi = E\psi \tag{2.7}$$

Solving equation 2.7, we obtain the energy eigenvalues of the outermost electron of the excimer molecule immersed in the host gas:

$$E_n = -\frac{1}{2}m\left(\frac{Ze^2}{4\pi\epsilon\hbar}\right)^2 \cdot \frac{1}{n^2} + V_0(N) = \frac{E_n^{is}}{\kappa^2} + V_0(N) \tag{2.8}$$

where Z is the atomic number of the excimer nucleous, n is the principal quantum number, E_n^{is} is the energy of the electron of the

[‡]i.e. excitations in which the principal quantum number of the excited electron is $> n+1$, with n principal quantum number of the outermost electron in the ground state

isolated excimer molecule, and κ is the dielectric constant of the host gas relative to vacuum, given by the usual Lorentz-Lorenz formula:

$$\kappa = 1 + \frac{\frac{N\alpha}{\epsilon_0}}{1 - \frac{N\alpha}{\epsilon_0}} \simeq 1 + \frac{N\alpha}{3\epsilon_0} \tag{2.9}$$

where α is the polarizability of the host gas and the approximation is correct within an error $< 0.02\%$ at the densities of our experiment. Since κ increases with N, also the polarization contribution gives rise to a decrease of the energy eigenvalues when the density of the host gas is increased.

The energy of the bound state involved in the transition observed is thus given by:

$$E_B = E_{n_B}\left(1 - \frac{2N\alpha}{\epsilon_0}\right) + V_0(N) \tag{2.10}$$

where E_{n_B} is the zero-density (i.e. isolated excimer) level, and where we expanded $1/\kappa^2 \simeq 1 - 2N\alpha/\epsilon_0$. Similarly, the energy of the dissociative state involved in the transition, is given by:

$$E_D = E_{n_D}\left(1 - \frac{2N\alpha}{\epsilon_0}\right) \tag{2.11}$$

where we dropped out the Fermi contribution because the energy shift $V_0(N)$ can be applied only to large principal quantum numbers n[Fer-34, Ama-34]. This assumption will be further justified *a posteriori* by the agreement of the model with the experimental data.

In the transition from the upper (bound) excimer level to the lower (dissociative) excimer level, the energy is irradiated at a wavelength λ_C given by:

$$\lambda_C^{-1} = \frac{E_{n_B} - E_{n_D}}{hc}\left(1 - \frac{2N\alpha}{\epsilon_0}\right) + \frac{\hbar}{mc}Na \tag{2.12}$$

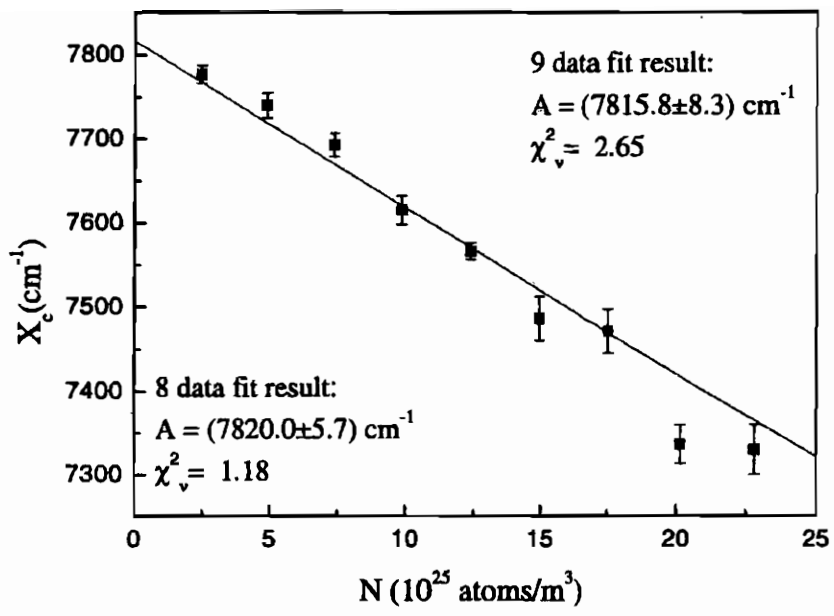

Figure 2.19: Result of the fit of the experimental data obtained with the model described in the text. The line is the result of the fit over all the data. The meaning of the 8 data fit is explained in the text.

where c is the light speed in vacuum. Actually, the principal quantum numbers n_B and n_D are not known. Therefore, we cast equation 2.12 in a form better suited for further analysis:

$$\lambda_C^{-1} = C - \left(C\frac{2\alpha}{\epsilon_0} - \frac{\hbar}{mc}a \right) N \tag{2.13}$$

where $C = (E_{n_B} - E_{n_D})/hc$ is an unknown constant. Equation 2.13 implies a linear red shift of the emission band as a function of the host gas density (note that $a < 0$).

We can now fit the data of Xenon in figure 2.13 with equation 2.13 using the experimental values of the scattering length and the

polarizability of Xenon ($a = -3.09$ Å[Zec-96] and $\alpha = 4.45 \times 10^{-40}$ F·m[Mai-81]), and treating C as a fitting parameter. In figure 2.19 we show the result of the interpolation. Note that if we repeat the fit after eliminating the data obtained at $N \simeq 20 \cdot 10^{25}$ atoms/m^3, that is more than three standard deviations lower than the fitting function value, the reduced-χ^2_ν becomes equal to 1.18, that is an excellent proof of the goodness of the fit.

We want to stress the fact that the free parameter of the fit is contained both in the intercept of the straight line at zero density and in its slope. We will be back on this point in the next section. Furthermore, neither the Fermi nor the polarization effects can be neglected, because their contribution to the red shift is nearly one to one.

A referee of a previously submitted paper[Bor-01] has suggested another model to describe the red shift of the excimer band: the broad band is ascribed to the transitions among all the vibrational levels of the bound excimer state towards the dissociative excimer state. Transitions from higher vibrational states obviously give rise to the emission of higher wavelength photons compared to transitions from lower vibrational states. Thus higher vibrational states are responsible for the *blue part* of the excimer peak, while lower vibrational states are responsible for its *red part*. As the pressure is increased, high vibrational levels relax towards the lowest vibrational level before they decay to the dissociative excimer state. So the higher the pressure, the lower the intensity of the blue part of the spectrum. This gives rise to an overall red-shift of the spectrum.

However, this model can not give quantitative predictions. Furthermore, an increase of the excimer band intensity with respect to atomic lines should be observed as the pressure is increased. The dissociation of high vibrational states is more probable than the dissociation of lower vibrational states because higher vibrational states are crossed by an higher number of dissociative curves. Since the model predicts that an increase of pressure corresponds to a depopulation of high vibrational states towards lower vibrational states, the number of states that dissociate in a non-radiative de-

cay should decrease as the pressure is increased. But we observed the opposite behavior. Moreover, we recall the fact that for pressure higher than 1 bar, the vibrational relaxation is commonly assumed to be rapid prior to the excimer decay[Bra-79, Pol-81, Mus-94]. A proof to this commonly accepted hypothesis comes from the vacuum-ultraviolet emission continua. In that case, the emission from the higher vibrational states (first continuum) can be observed only if the pressure of the gas is much lower than 1 bar[Pol-81]. Finally, in the next section we shall show another experimental result that is in striking contradiction with this approach, and that can be very well described using our Fermi+polarization model.

Concerning the broadening of the excimer band related to the increase of the gas density, it can be observed that the bound excimer state has a predissociative nature, i.e. it is crossed by several repulsive curves. In figure 2.9, for example, we have drawn the repulsive curve related to the $6p$ atomic level. When the pressure is increased, the collision-induced dissociation of the bound excimer levels also increases. This reduces the lifetime of the excimer molecules, giving rise to a broadening of the associated emission bands. It is interesting to note that the $^1\Sigma_u^+$ and $^3\Sigma_u^+$ excimer bound levels (that are responsible for the vacuum ultraviolet second continuum) are not crossed by any repulsive curve[Mul-70, Bow-86]. This could explain the different behavior of the FWHM of the second continuum respect to the band under investigation. However, a quantitative description would require much more accurate potential energy curves than those actually available.

The collision-induced dissociation of the bound excimer levels is also responsible for the overall increase of the atomic emission respect to the excimer emission. Figure 2.16 evidences that the behavior is different from line to line. More detailed spectra are necessary to determine more precisely the kinetic of the relaxation processes involved.

2.3 Test of the theoretical model for the description of the excimer red shift in Xenon

The aim of this section is to provide a striking validation of the theoretical model for the description of the excimer red shift in Xenon. We report on an experimental study of the emission spectra in an Argon-Xenon mixture (90%-10%).

Although the concentration of Xenon is rather low, the excimer band investigated in the previous section should be still present. When a small amount of a heavier gas is added to a large amount of a lighter gas, the sequence of particle induced excitation processes follows the scheme reported below (see [Bra-79] and references therein). Much of the effect of the passage of the particle is to form excited atoms and ions of the lighter (dominant) species. These evolve in the same way as they evolve when there is no added gas. In addition, if the excited species are sufficiently energetic they may react with the heavier rare gas atoms to form ions in Penning or associative reactions:

$$Ar^* + Xe \longrightarrow Ar + Xe^+ + e^- \tag{2.14}$$

$$Ar^* + Xe \longrightarrow ArXe^+ + e^- \tag{2.15}$$

Generally, these reactions are very fast and occur at every collision (if there is sufficient energy).

If the energy of excitation is not sufficient to induce reactions 2.14 and 2.15, energy transfer to heavier species may occur in the reactions:

$$Ar^* + Xe \longrightarrow Ar + Xe^* \tag{2.16}$$

$$Ar_2^* + Xe \longrightarrow 2Ar + Xe^* \tag{2.17}$$

Reaction 2.16 is generally slow, unless there is a near resonance between the initial and final states. On the contrary, reaction 2.17 is generally rapid because a close resonance is not needed.

Also charge transfer from molecular ions to atoms is generally very fast:

$$Ar_2^+ + Xe \longrightarrow 2Ar + Xe^+ \tag{2.18}$$

The ions and excited atoms of the heavier species can finally form homonuclear molecules (ions or excimers) either directly:

$$Xe^+ + Xe + Ar \longrightarrow Xe_2^+ + Ar \tag{2.19}$$

$$Xe^* + Xe + Ar \longrightarrow Xe_2^* + Ar \tag{2.20}$$

or following two step processes (usually faster):

$$Xe^+ + 2Ar \longrightarrow (ArXe)^+ + Ar \tag{2.21}$$

$$(ArXe)^+ + Xe \longrightarrow Xe_2^+ + Ar \tag{2.22}$$

and

$$Xe^* + 2Ar \longrightarrow (ArXe)^* + Ar \tag{2.23}$$

$$(ArXe)^* + Xe \longrightarrow Xe_2^* + Ar \tag{2.24}$$

In figure 2.20 we show a typical spectrum (obtained with the same technique used for the previous measurements) of the Argon-Xenon mixture at room temperature and nearly atmospheric pressure. The broad band still dominates the spectrum.

The red shift of the excimer band should be quantitatively different. Xenon excimers in the mixture are mostly surrounded by Argon atoms, whose scattering length and polarizability are smaller. A smaller red shift is therefore expected. In figure 2.21 we report

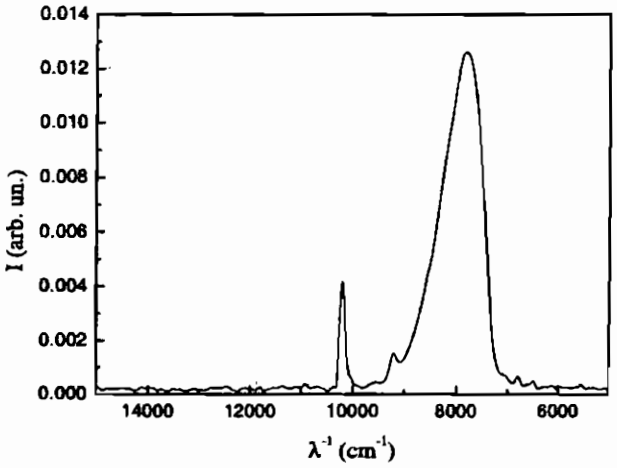

Figure 2.20: Spectrum of particle induced infrared emission in an Argon(90%)-Xenon(10%) mixture at room temperature and nearly atmospheric pressure.

the spectra obtained at the same three pressures used for the spectra of figure 2.10. The shift in pure Xenon is larger than the shift in the mixture.

In figure 2.22 we show the red shift of the excimer peak as a function of the mixture density, calculated in the same way as the red shift of pure Xenon has been calculated in the previous section. The line represents the result of the fit obtained with equation 2.13, using the scattering length and polarizability of Argon instead of those of Xenon ($a = -0.86$ Å, $\alpha = 1.827 \times 10^{-40}$ F·m[Mai-81]) and treating C still as a free parameter. The value of C obtained from Argon-Xenon mixture is in perfect agreement with that obtained from pure Xenon. If we repeat the interpolation of the mixture data using equation 2.13 with $C = 7820$ cm^{-1} (the value obtained from pure Xenon), the resulting reduced χ^2_ν (with no free parameter) is 1.79, only 13% higher than its minimum value in the one-free parameter fit.

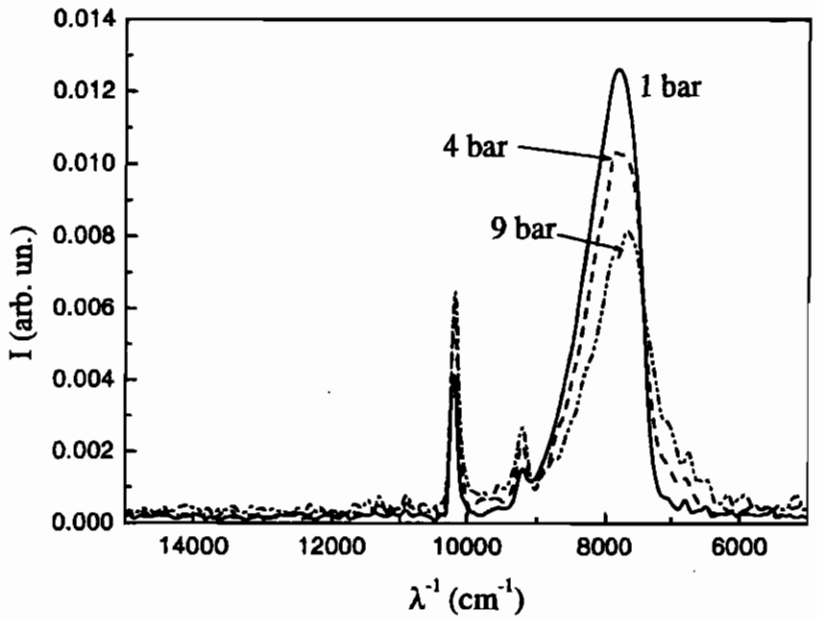

Figure 2.21: Argon(90%)-Xenon(10%) spectra at three different pressures.

This measurement is a quite stringent proof for our model. Furthermore, according to the model discussed at the end of the previous section, no differences should be observed between pure Xenon and Argon-Xenon mixtures.

We also performed a very preliminary study of a Helium-Xenon mixture. The scattering length of Helium is positive. The Fermi contribution should therefore give rise to a blue shift of the excimer band. The polarization effect, on the contrary, should still produce a red-shift of the band that should compensate the Fermi contribution. An almost pressure independent behavior is therefore expected. Our first results confirm this prediction, although we only collected three spectra in the 2 to 4 bar pressure range.

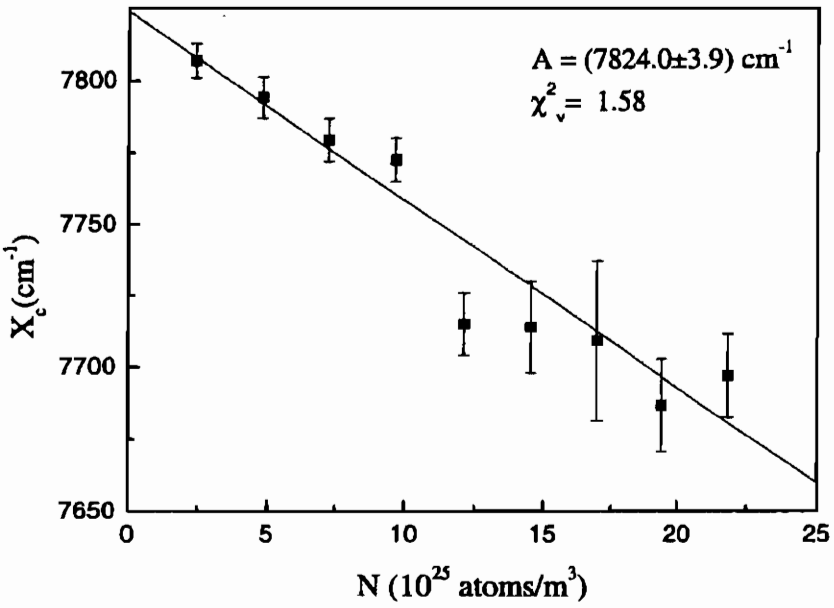

Figure 2.22: Red shift of the excimer band as a function of the density in an Argon-Xenon mixture. The line is the result of the fit obtained with the model described in the text.

Chapter 3

Drift emission in noble gases.

Introduction

In the previous chapter we have presented a study on particle induced infrared emission in noble gases. The aim of the investigation was to identify the mechanism of prompt emission. Thus, no electric field was purposely applied inside the ionization chamber. However, we have already remarked that, when an electric field is applied, an increase of the infrared light output is observed[Car-98, Lin-88c] (*drift emission*). We have also underlined that vacuum-ultraviolet emission increases as well. In the latter case, the enhancement is generated by the ionization electrons that gain energy from the electric field and excite more gas atoms through inelastic collisions[Pol-81]. It is reasonable to ascribe the increase of the infrared light output to a similar phenomenon.

This chapter is devoted to an experimental investigation of drift emission properties in gaseous Argon. The aim of this study is to verify that infrared drift emission is generated by drift electrons that scatter inelastically on the gas atoms. In the first section we describe the experimental apparatus. In the second section we show the results obtained, that are discussed in the third section.

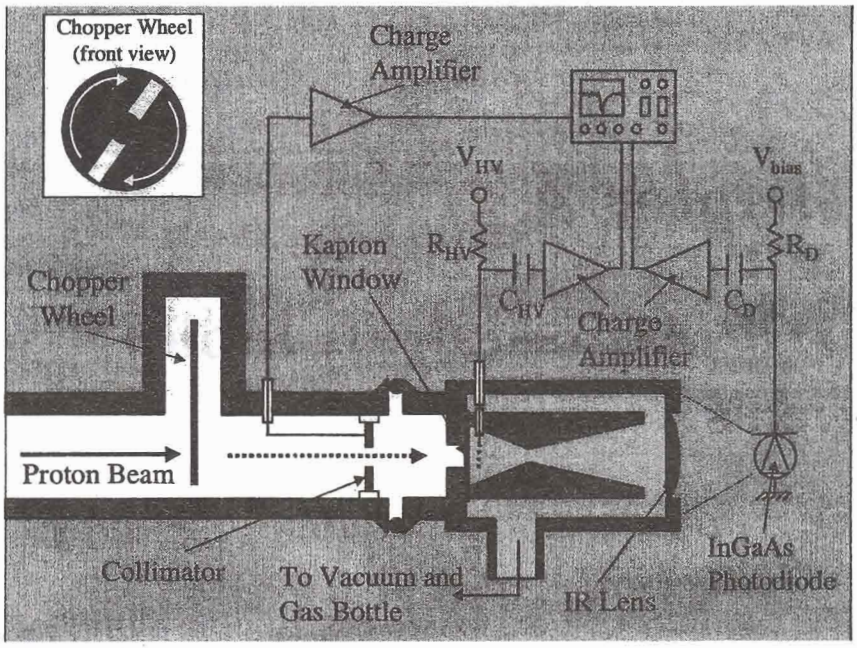

Figure 3.1: A scheme of the experimental apparatus for the measurement of the drift scintillation properties in gaseous Argon.

3.1 Experimental apparatus

In figure 3.1 we report a scheme of the experimental apparatus. A proton beam enters an ionization chamber filled with gaseous Argon, kept at room temperature and nearly atmospheric pressure. The ionization electrons drift inside the gas under the influence of an electric field. The infrared radiation of both prompt and drift emission is focused on an infrared sensor by means of a light guide coupled with an infrared lens.

The proton beam is extracted from a Van deer Waals linear accelerator (Laboratori Nazionali di Legnaro, Istituto Nazionale di Fisica Nucleare, Legnaro, Padova, Italy). The energy of the protons is 3.5 MeV and the current of the continuous beam is approximately

1 nA. The beam is bunched by means of a rotating metallic chopper, machined as shown in the inset of figure 3.1. The wheel rotates at a frequency of about 140 Hz and chops the beam into 400 μs bunches. The bunches are then collimated by means of a metallic pierced plate (hole diameter = 2 mm). The collimator is connected to a charge amplifier[Bac-86] (conversion factor = 0.25 mV/fC, decay constant = 400 μs, nominal values), whose signal is sent to a digital oscilloscope and used to monitor the beam intensity.

The collimated proton bunches enter a stainless steal vessel filled with the sample gas, passing through a pierced flange. The hole of the flange (diameter = 4 mm, depth = 16 mm) is closed by a 125 μm thick kapton window, that separates the beam pipe vacuum from the gas inside the vessel. A 2 μm thick copper film is previously evaporated on the internal side of the window. The energy of the protons after crossing the window is equal to approximately 0.9 MeV[Ber-00].

The ionization chamber consists of a copper cylinder (diameter = 38 mm, height = 45 mm) machined in such a way to obtain a double baseless semiconical cavity (see figure 3.1 and figure 3.2). The two semicones face each other, with the smaller base in common (diameter = 6 mm) and they have a common axis. Their heights are 33 mm for the longer and 12 mm for the shorter. The cavity is fixed to the pierced flange of the vessel with the entrance window in the center of the larger base of the smaller semicone. So the proton bunches enter directly from the beam pipe into the smaller semicone, aligned along its axis. The projected range of a 0.9 MeV proton in Argon gas is given in table 3.1 as a functions of pressure[Ber-00], from 2 bar (minimum working pressure) to 6 bar (maximum working pressure). It can be seen that the protons come at rest inside the smaller semicone.

An array of copper wires (diameter = 50 μm, pitch = 1 mm) is tightened at 7 mm from the entrance window. The wires are connected to an high voltage positive power supply. Since the copper film evaporated on the kapton window and the whole copper cylinder are kept to ground, the electric field drives the electrons

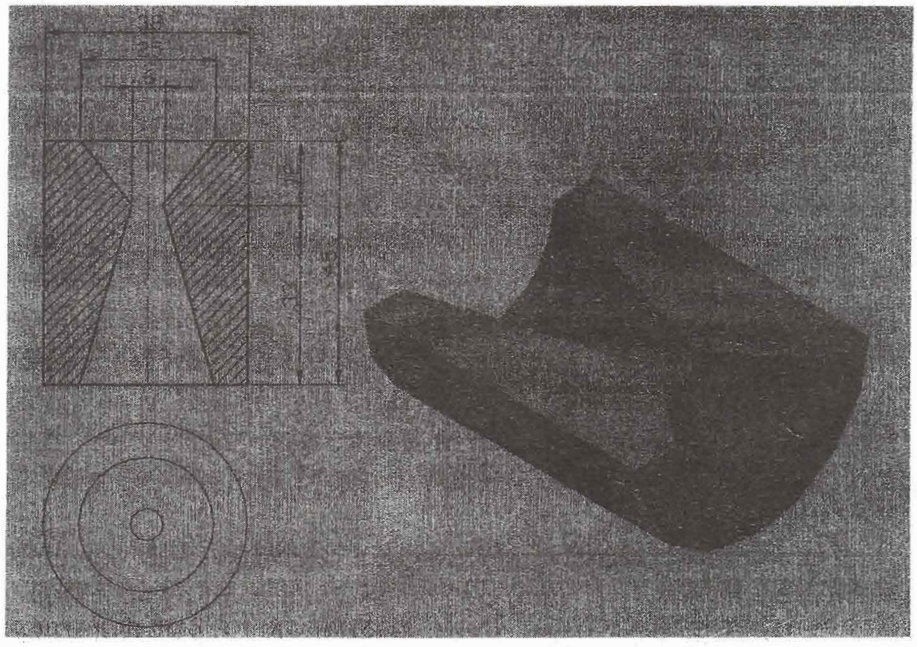

Figure 3.2: A technical and pictorial drawing of the internal part of the ionization chamber (dimensions in mm).

$E_{p^+} = 0.9$ MeV, range in Argon (cm)				
2 bar	3 bar	4 bar	5 bar	6 bar
1.09	0.72	0.54	0.43	0.36

Table 3.1: Projected range of 0.9 MeV protons in gaseous Argon at different pressures.

towards the wires. A charge amplifier[Bac-86] (conversion factor = 0.25 mV/fC, decay constant = 400 μs, nominal values) is also connected to the wires, and its signal is sent to a digital oscilloscope. The electronic coupling of the amplifier is shown in figure 3.1, where $R_{HV} = 10$ MΩ and $C_{HV} = 4.7$ nC (nominal values).

The shape of the cavity is designed to maximize the collection of the light produced in the smaller semicone on a sapphire lens (focal = 100 mm, diameter = 50 mm) located 55 mm away from the larger base of the longer semicone. Since the light collection efficiency strongly depends on the reflectivity of the walls, these were previously polished with a polishing paste containing 0.25 μm diameter diamond grains. According to [Gra-72], the reflectivity of copper is higher than 97% in the wavelength region between 0.7 μm and 1.7 μm.

The infrared sensor (InGaAs photodiode G5832-05, EG&G) and its electronic read-out are the same used in the spectrometer described in Chapter 1 (without the shaping amplifier). For the details, we refer the reader to that chapter (see also figure 3.1, where $R_D = 10$ MΩ and $C_D = 4.7$ nF, nominal values).

The ionization charge signal, the light signal, and the beam signal from the collimator are simultaneously displayed on three different tracks of a digital oscilloscope and are averaged over some hundreds sweeps in order to reduce the noise. Data were taken as a function of the high voltage applied on the wires and of the pressure of the gas.

3.2 Experimental results

We measured on the oscilloscope the amplitudes of (i) the infrared signal (L), of (ii) the charge signal (Q), and of (iii) the collimator signal (B), as a function of the voltage applied on the wires (HV), for different pressures of the gas (P). The mean value of B for different pressures runs changes because of long term fluctuations of the proton beam intensity. For this reason, we averaged B over

all the data corresponding to a given pressure, and normalized L and Q to the value obtained[†]. In figures 3.3 to 3.7 we report the normalized values (Q_n and L_n) as a function of the high voltage applied on the wires for different values of the gas pressure. The error bars have been calculated by propagating the statistical error of B in the normalization procedure.

The prompt and drift emission regions can be easily distinguished for all the pressures investigated. The light output, in fact, is independent from HV until a threshold HV_{thr} is reached (prompt emission). For $HV > HV_{thr}$, the light output increases (almost linearly) as HV is increased (drift emission). Note that, for low value of HV, Q_n increases with the increase of HV. This behavior can be ascribed to the low charge collection efficiency of our ionization chamber, that reaches its maximum value only for relatively high values of HV. Once this maximum value is reached, Q_n becomes almost independent from HV, except for very high value of HV, where charge multiplication probably starts to take place[Sau-77].

In order to study the behavior of the prompt light intensities as a function of the gas density, for each pressure we averaged the values of L_n obtained for low values of HV, where only prompt emission occurs. In figure 3.8 the results are shown. The error bars are the statistical deviations. Note that in this estimation we neglect the influences of proton range on the overall light collection efficiency, that is therefore assumed pressure independent. The data are quite scattered. However, except for the value relative to $P = 2$ bar, it can be seen that pressure has no dramatic effects on the light output, as already observed in the measurements of the prompt emission spectra (see Chapter 2). Concerning the value relative to $P = 2$ bar, the approximation on the light collection efficiency is probably too rough for a correct comparison with the other pressures. In fact the residual range at this pressure brings

[†] B is not strictly proportional to the charge entering into the chamber, because the beam profile and direction do not remain stable with time. However, its mean value averages the trajectory fluctuations, and gives a good estimate of the mean charge entered in the chamber during different runs.

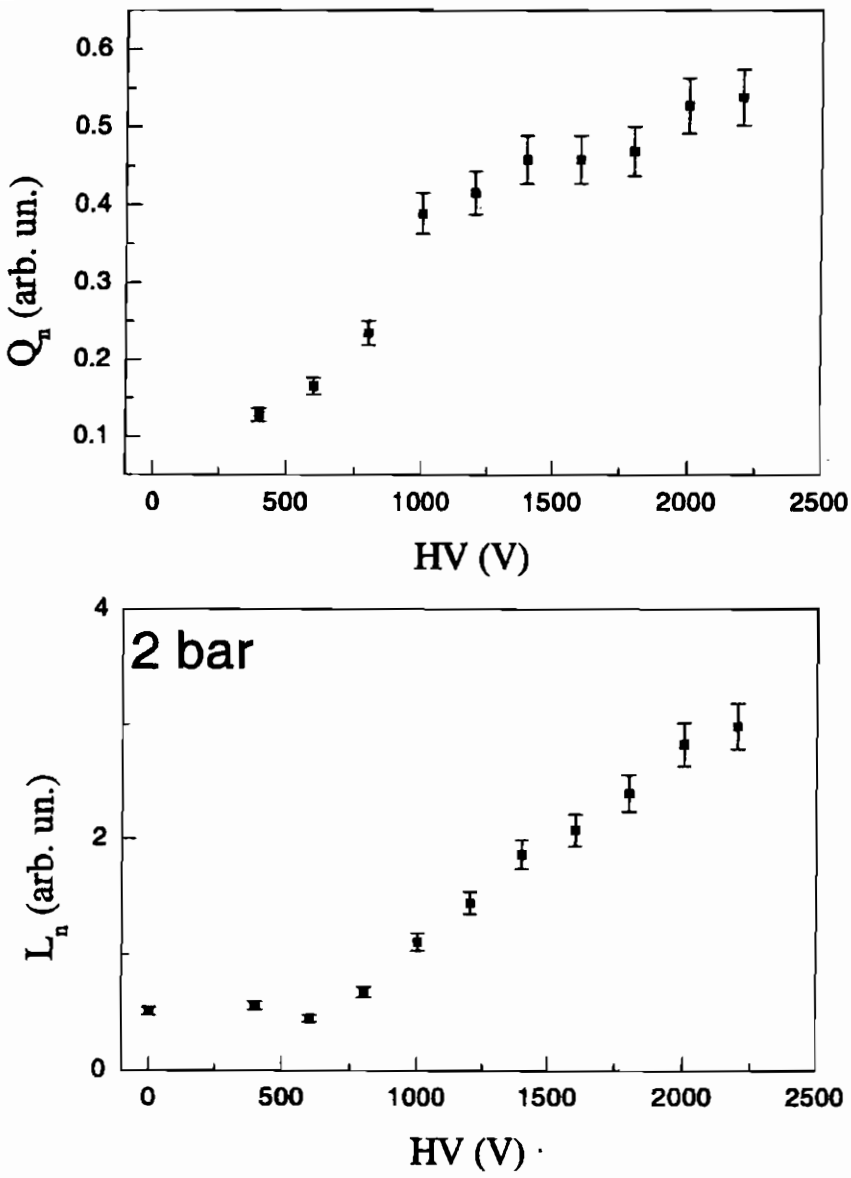

Figure 3.3: Normalized charge and light signals as a function of the voltage applied at $P = 2$ bar.

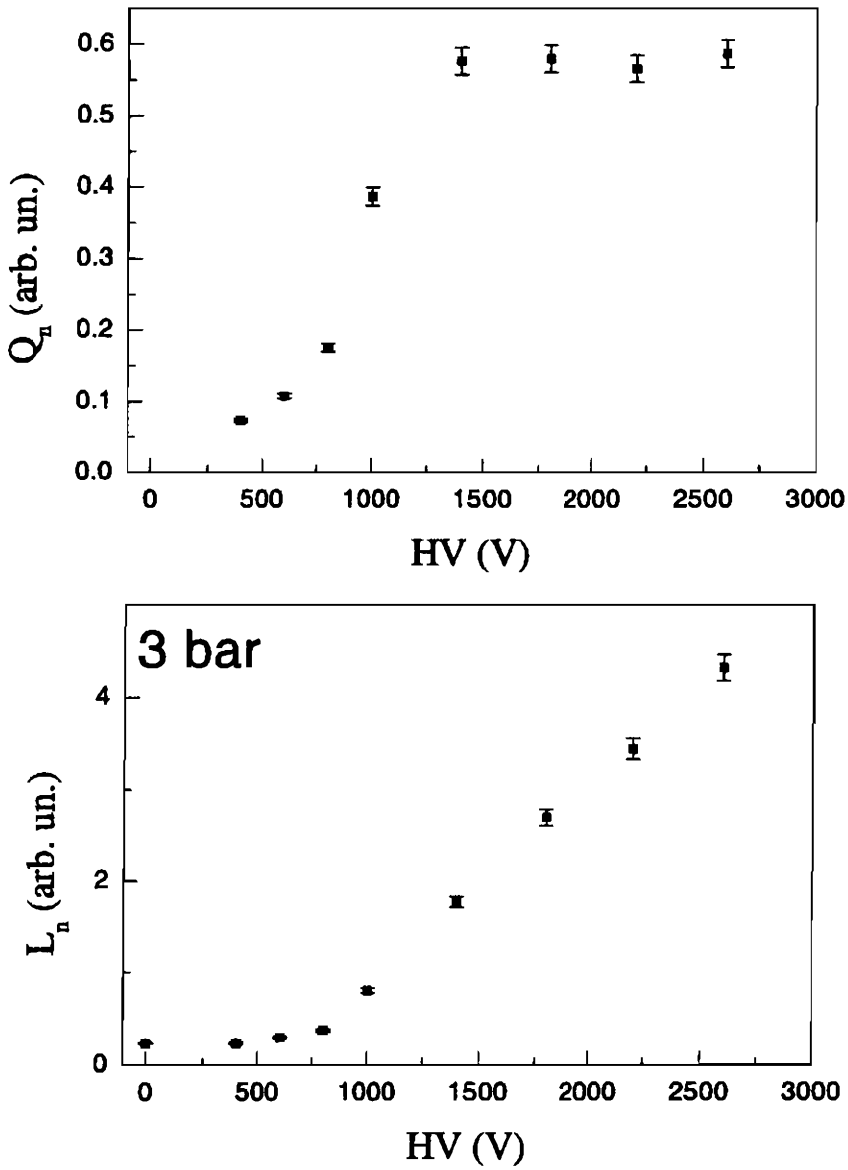

Figure 3.4: Normalized charge and light signals as a function of the voltage applied at $P = 3$ bar.

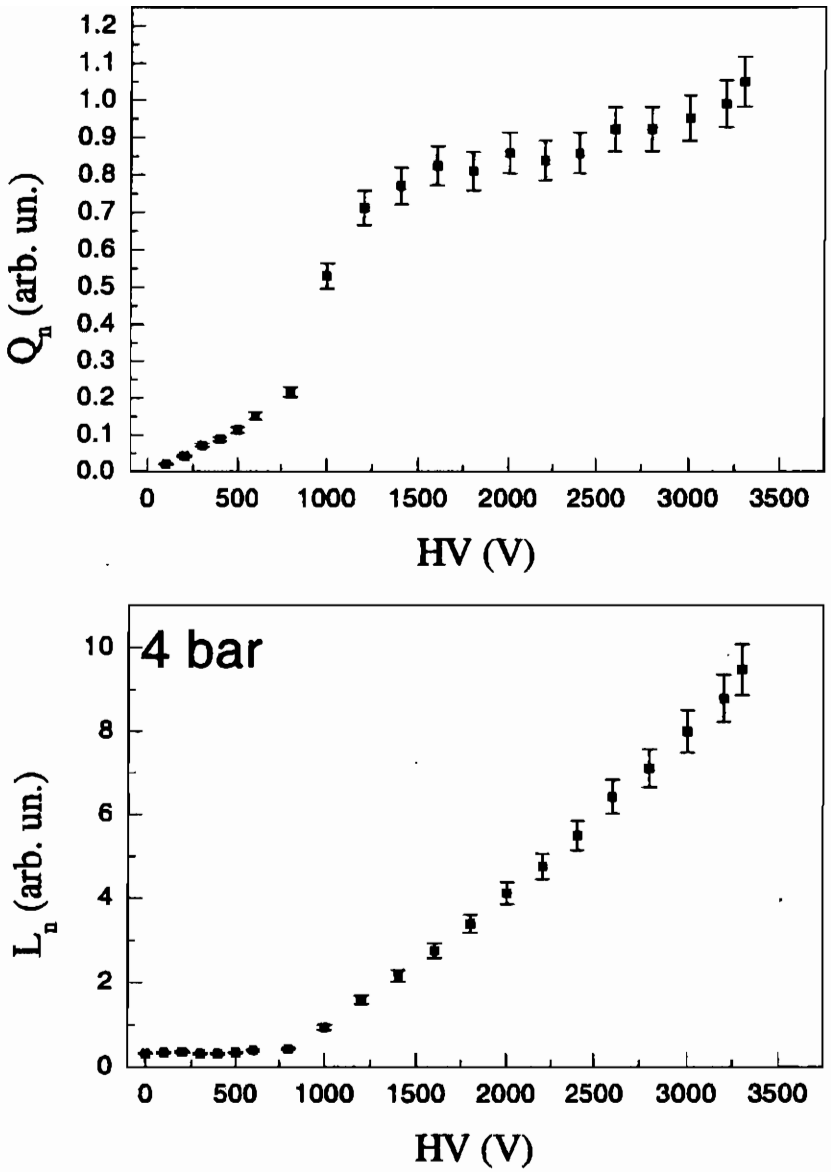

Figure 3.5: Normalized charge and light signals as a function of the voltage applied at $P = 4$ bar.

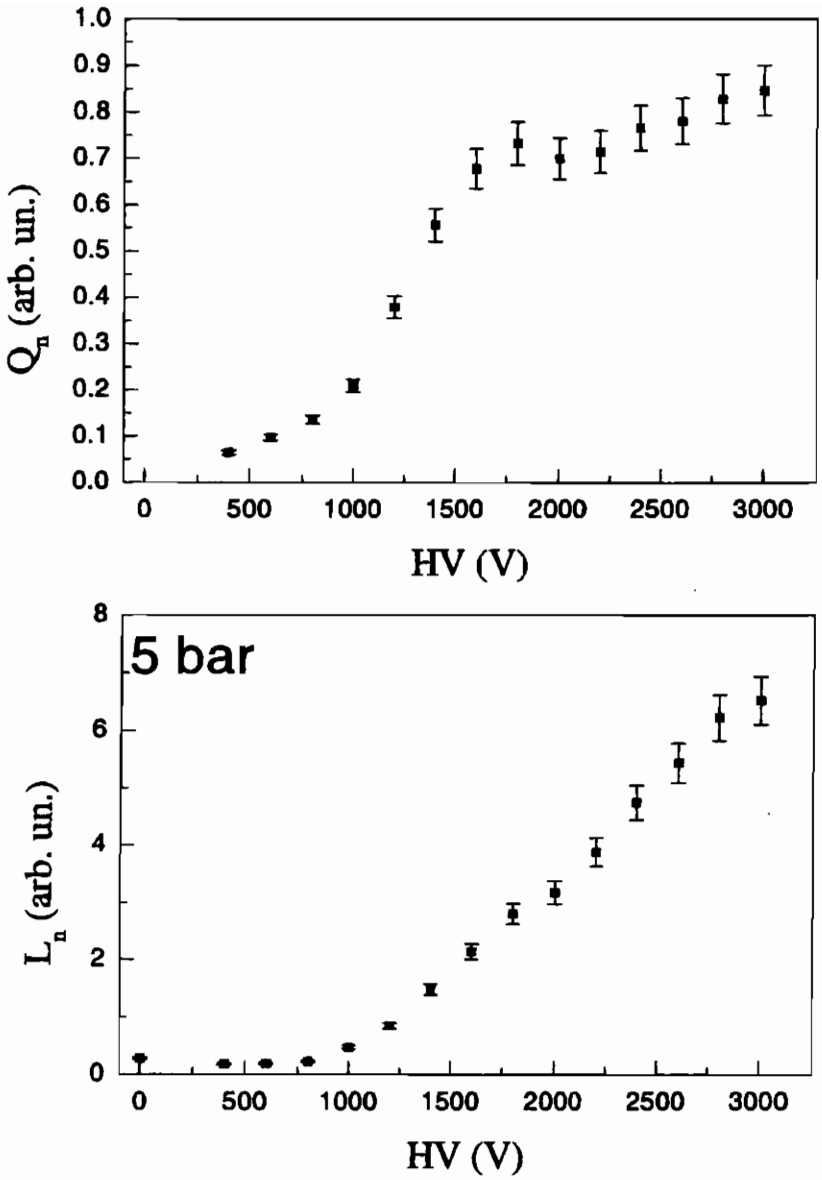

Figure 3.6: Normalized charge and light signals as a function of the voltage applied at $P = 5$ bar.

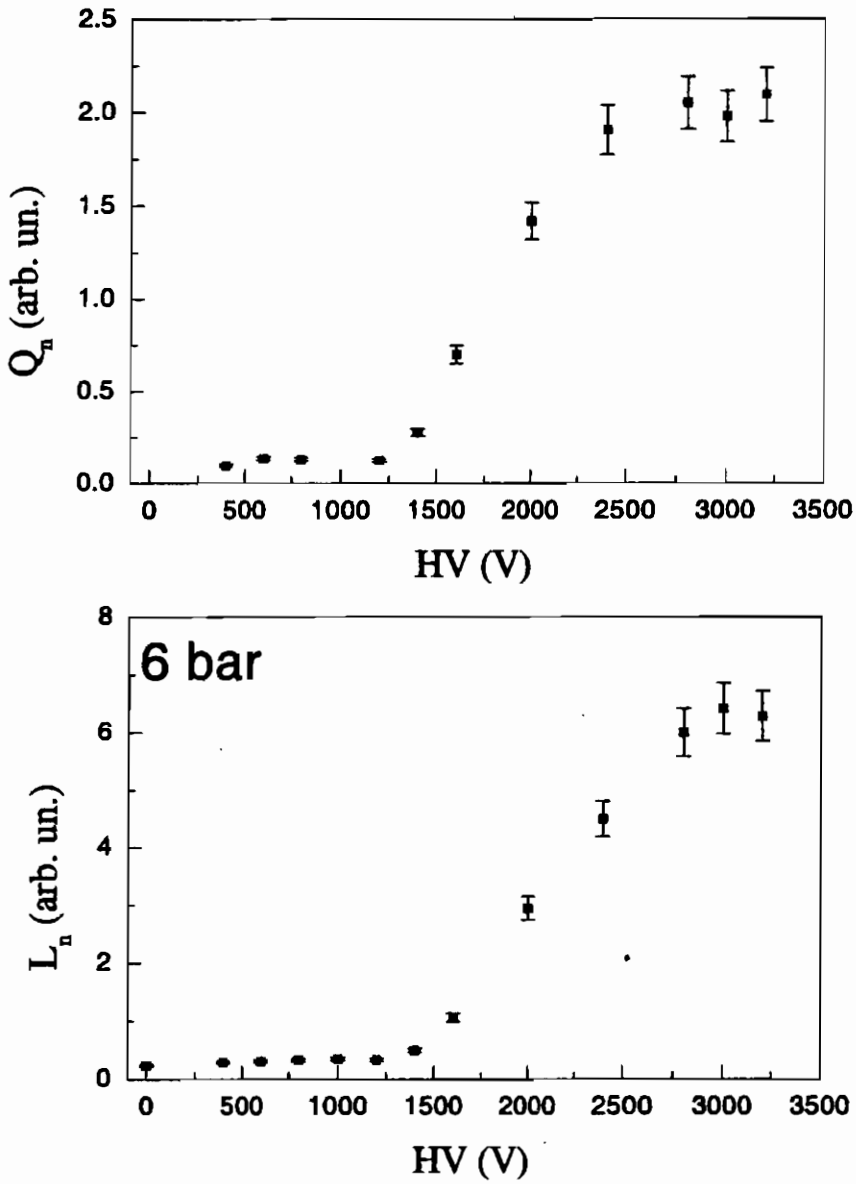

Figure 3.7: Normalized charge and light signals as a function of the voltage applied at $P = 6$ bar.

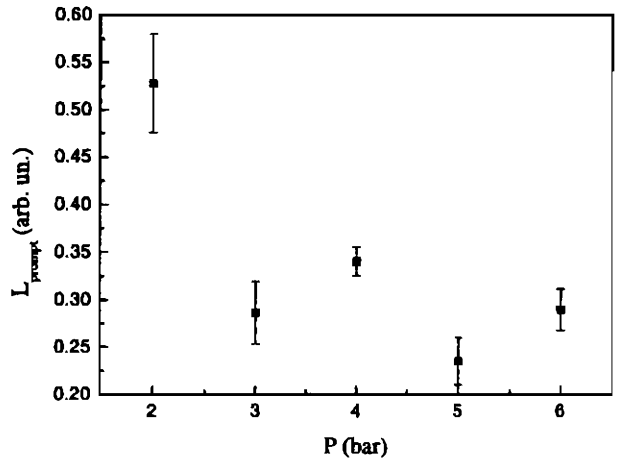

Figure 3.8: Normalized prompt emission as a function of pressure.

the protons very closed to the tip of the smaller semicone (see table 3.1).

We also evaluated HV_{thr} as the intersection of the constant part of $L(HV)$ with its linear increasing region. In figure 3.9 we show the results as a function of P and the results of the linear best fit, that excellently interpolates the data.

3.3 Discussion and conclusion.

To explain the electric field dependence of the light output we propose the following model. The hot free electrons created by the ionizing particles quickly loose their excess energy through inelastic collisions with the gas atoms and reach an equilibrium distribution. When no electric field is applied, the equilibrium energy distribution function has the typical Maxwellian shape, centered around $\langle \epsilon \rangle \simeq k_B T$, where k_B is the Boltzmann constant and T is the temperature of the gas. Since the fraction of electrons with energy ϵ

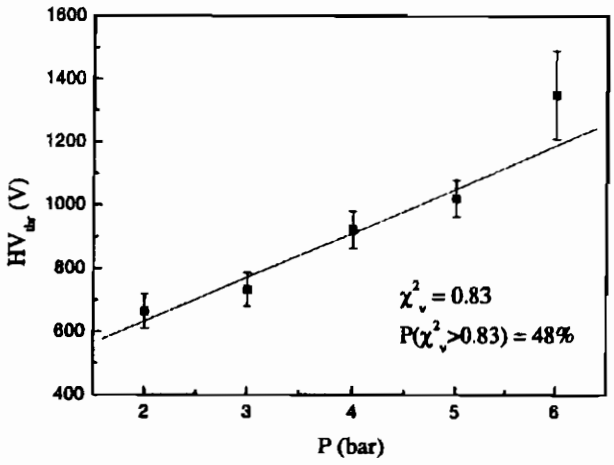

Figure 3.9: High voltage threshold as a function of pressure. The line is the result of the linear best fit.

higher than the atomic first excited state ϵ_1 is negligibly small, elastic collisions dominate in the electron-atom interactions. When an electric field is applied, the energy distribution function is shifted towards higher values, and the fraction of electrons with $\epsilon > \epsilon_1$ consequently increases. These electrons can scatter inelastically with the atoms, raising them into excited states. The relaxation process of the excited atoms gives rise to the emission of infrared photons. We therefore ascribe infrared drift emission to the de-excitation of the atoms excited by the drifting electrons through inelastic collisions.

In order to test the model with our data, we can calculate the fraction of electrons with $\epsilon > \epsilon_1$. The energy distribution function $f(\epsilon)$ of an electron swarm drifting under the influence of an electric field E can be found by solving the Maxwell-Boltzmann transport equation[Wan-68][††]:

[††]This approach is commonly and successfully applied in the description of

$$f(\epsilon) = \int_0^{\epsilon} x^{1/2} g(x) dx \tag{3.1}$$

where g is the normalized Davidov-Pidduck function:

$$g(x) = A \exp\{-\int_0^x \frac{dz}{k_B T + \frac{1}{6}\frac{M}{m}\left(\frac{eE}{\sigma(z)N}\right)^2 \frac{1}{z}}\} \tag{3.2}$$

In equation 3.2, M is the mass of an Argon atom, m is the electron mass, e is the electron charge, N is the density number of the gas, $\sigma(\epsilon)$ is the momentum transfer cross section at the energy ϵ, and A is the normalization constant, which makes:

$$\int_0^{\infty} f(\epsilon)\, d\epsilon = 1 \tag{3.3}$$

In the Davidov-Pidduck function, all the inelastic collisions are neglected. If inelastic collisions occur, the function $g(\epsilon)$ can be derived with the so-called backward prolungation technique[She-60]. In our case, however, the inelastic contribution amounts only to a 1% correction, since the inelastic cross section is at least a factor 10 smaller than the elastic one[Zec-96].

In equation 3.2 we assume that the electric field is constant and uniform in the drift region. We will be back on this point shortly below.

The fraction Φ of electrons whose energy exceeds ϵ_1 is given by:

$$\Phi = \int_{\epsilon_1}^{\infty} f(\epsilon)\, d\epsilon \tag{3.4}$$

In figure 3.10 we show the value of Φ as a function of the electric field E for different pressures. The qualitative behavior predicted by the model reproduces well our data. In fact, Φ is nearly zero until a critical value of the electric field E_{thr} is reached. Then, it increases almost linearly.

---

the electronic transport properties (drift velocity and diffusion) of gases in a wide range of densities (see, for example, [Hux-74] and [Fro-64])

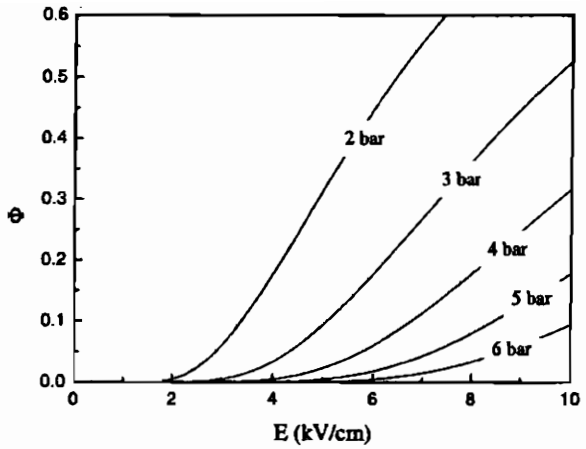

Figure 3.10: Fraction of the electrons with energy higher that the first excited state as a fuction of the electric field applied, for different values of pressure.

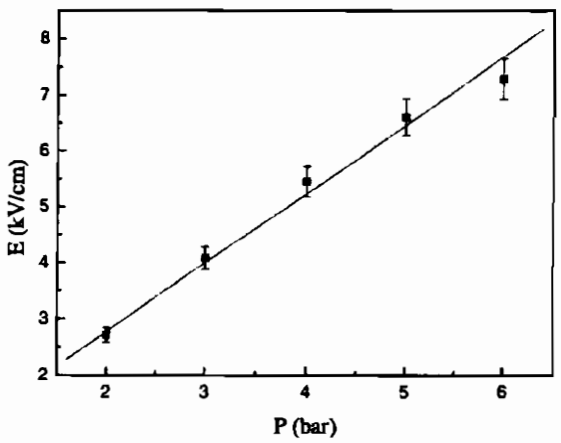

Figure 3.11: Electric field threshold as a function of pressure according to the model. The line is the result of the linear best fit.

Using the data reported in figure 3.10, it is possible to estimate the value of E_{thr} as the intersection of the linear increasing region of $\Phi(E)$ with the $x-$axis of the graph. Figure 3.11 shows the result of this elaboration. The error bars are an estimate of how the fitting extremes influence the result. The linear behavior of E_{thr} is in agreement with the linear behavior of HV_{thr}. However, if we simply estimate the electric field threshold of our experimental data dividing HV_{thr} by the distance between the entrance window and the wires ($d = 7$ mm), we obtain values that are a factor 3 lower with respect to the model. This estimate for the electric field is not sound since we are dealing with wires. Furthermore the electron drift time in the gas ($\simeq 2 - 3$ μs) is much shorter than the proton bunch length, so we can not distinguish whether the drift emission occurs in all the 7 mm drift region or only near the wires, where the electric field is stronger.

On the basis of the results reported above, we can claim that the drift emission is generated by the de-excitation of the gas atoms excited by the drifting electrons. Further studies are under way to confirm this hypothesis. Among them, we have performed a detailed study of infrared emission induced by electrons near a thin wire, that will be discussed in the next chapter.

Chapter 4

Infrared scintillation of noble gases for particle detection purposes.

Introduction

In Chapter 2 we have shown that the study of infrared emission from beam-excited noble gases is a valuable tool for the investigation of fundamental processes in the interaction of charged particles with matter. We have pointed out that the passage of an ionizing particle produces several excited atoms, whose de-excitation towards the ground state is responsible for the infrared emission observed. The emission does not follow the same mechanism for every species. In lighter noble gases (Helium, Neon, and Argon) the emission is ascribed to atomic radiative decays among highly excited states. This simple pathway is not the more efficient way to reach the ground state for heavier noble gases (Krypton and Xenon). In this case, in fact, excited atoms form excimer molecules that emit infrared photons in the decay towards lower lying dissociative states. In Krypton, excimer transitions and atomic transitions have nearly the same intensity. In low pressure Xenon (pressure lower than 3 bar), the excimer emission mechanism dominates over all the atomic

transitions.

The analogies between infrared and vacuum-ultraviolet particle induced emission in Xenon is remarkably interesting. In both cases, the spectrum is dominated by an excimer broad band. Since these continua are largely more intense than all the atomic lines, it is reasonable to expect that the infrared light yield be of the same order of magnitude of vacuum-ultraviolet scintillation light yield ($\simeq$ 20000 photons/MeV[Miy-92]). This would be extremely promising for the development of new scintillator detectors which might exploit infrared photons rather than ultraviolet scintillation light. In order to clarify if this unexplored approach can be successfully pursued, it is necessary to measure the *infrared scintillation* light yield.

Another important issue in the development of gaseous infrared scintillator detectors is to understand how much the light emission can be enhanced by accelerating the ionization electrons with an electric field. We have already seen in the previous chapter that drift emission can provide large increases on the light output. More generally, it is reasonable to expect more intense emission when very high electric fields are applied and electron multiplication occurs.

In this chapter we report on the measurement of infrared scintillation light yield in gaseous Xenon. In the first section we describe the experimental apparatus. In the second section we show the result of the measurement. In the third section, we briefly present an upper estimation of the infrared scintillation light yield in gaseous Argon and Krypton, obtained with the same set-up.

The last section is devoted to the study of the infrared emission induced by drift electrons near a thin wire tighten inside an ionization gas chamber, and its applications for particle detection purposes. In particular, we discuss the potentiality of proportional chambers in which the track of the particle is detected by an infrared optical device faced to the detection medium. This read-out system is compared to the usual electronic read-out.

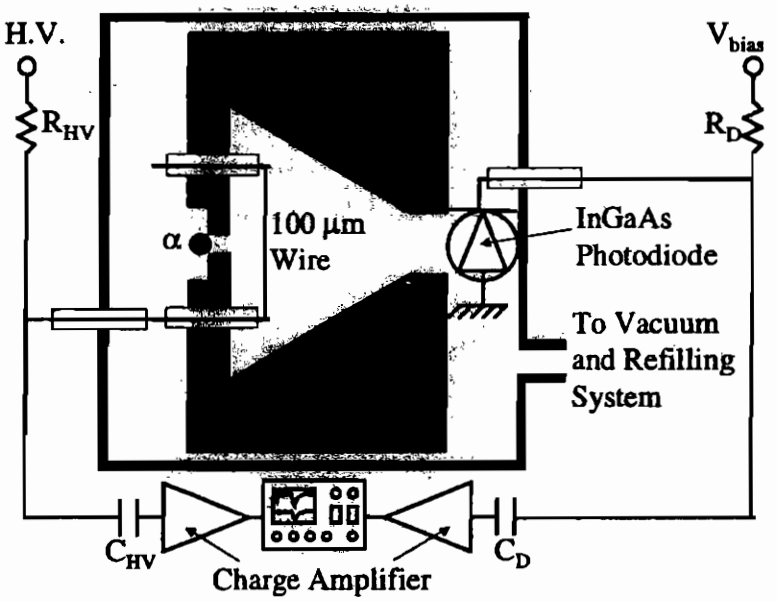

Figure 4.1: A scheme of the experimental apparatus for the measurement of the infrared scintillation light yield in gaseous Xenon.

4.1 Prompt light yield of gaseous Xenon: experimental apparatus

The experimental apparatus for the measurement of the infrared scintillation light yield in gaseous Xenon is reported in figure 4.1. The gas is excited by means of an alpha source. The infrared light emitted by a stopped alpha particle in gas is detected by an infrared photodiode. The ionization electrons are collected by a wire kept at positive voltage. The infrared scintillation light yield is calculated by means of:

$$LY = \frac{N_f}{\epsilon} \cdot \frac{1}{E} \cdot \frac{1}{Q} \tag{4.1}$$

where N_f is the (measured) mean number of photons detected by the photodiode for a single alpha particle event, ϵ is the light col-

lection efficiency (to be measured independently), E is the mean energy released in the gas in a single alpha particle event (that can be calculated using the stopping power of gaseous Xenon), and Q is the mean quantum efficiency of the detector in the wavelength region of emission (to be calculated using the nominal quantum efficiency of the detector Q_{PD} and the emission spectrum shown in Chapter 2).

The gas is contained into a large stainless steel vessel, kept at room temperature. The filling pressure is 1.95 ± 0.02 bar. The vessel can be evacuated down to 10^{-5} mbar by means of a turbomolecular pump, coupled with a membrane pump, before each filling.

To enhance the light collection efficiency, the photodiode is faced to the smaller aperture of a copper cavity with a baseless semiconical shape (smaller base diameter = 8 mm, larger base diameter = 4 cm, height = 4 cm). The opposite part of the semicone is closed with a pierced base (hole diameter = 2 mm), screwed onto the walls of the cavity. The alpha source is mounted outside the cavity, in front of the aperture of the pierced base. Thus the infrared light collected by the photodiode is a fraction ϵ of the scintillation light of the gas contained into the cavity, excited by collimated alpha particles. The walls of the cavity and of the base are polished with a polishing paste containing 0.25 μm diameter diamond grains. According to [Gra-72], the reflectivity of copper is higher than 97% in the wavelength region between 0.7 μm and 1.7 μm.

Before mounting the alpha source on the cavity and insert the cavity in the vessel, we measured the light collection efficiency, using the scheme reported in figure 4.2. The value of ϵ is obtained by means of $\epsilon = \frac{I_D}{I_T}$, where I_D is the light intensity detected by the photodiode when a light source of known intensity I_T is placed at the entrance of the cavity. The source is the black body radiation emitted by a 5 mm long incandescent nickel-chromium filament, warmed up by Joule effect. To measure I_T, the filament is previously placed directly in front of the photodiode, outside the cavity. Each point of the filament surface can be treated as a point-like source that emits isotropically in the 2π forward halve of the solid

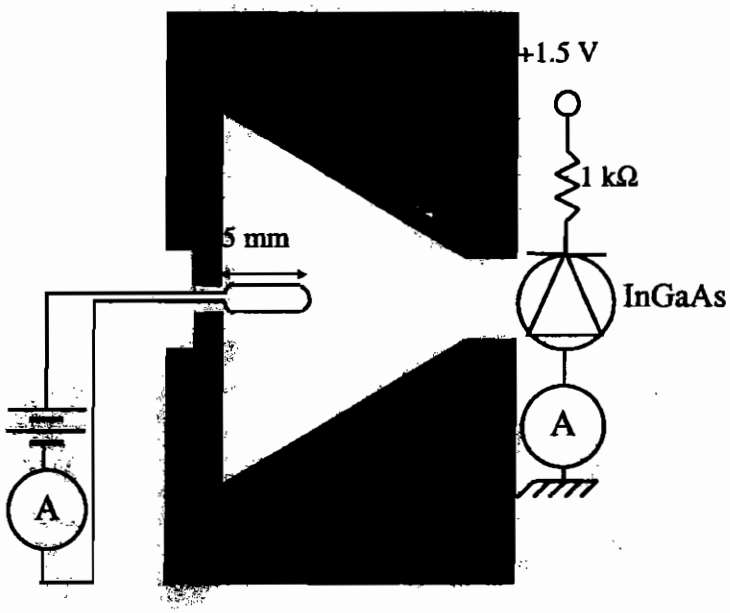

Figure 4.2: A scheme of the experimental apparatus for the measurement of the light collection efficiency of the cavity (not to scale).

angle. In the configuration illustrated in figure 4.3, the intensity of the light detected by the photodiode I_Ω is related to I_T according to:

$$I_\Omega = \frac{1}{2} \cdot I_T \cdot \left(\frac{\Omega}{2\pi}\right) \tag{4.2}$$

where Ω is the solid angle under which the detector sees the filament, and the factor $\frac{1}{2}$ is due to the fact that the photodiode sees one half of the filament total surface. If the distance d between the photodiode and the filament is much longer than the diameter Φ of the photodiode, then $\Omega = \frac{\pi\Phi^2}{4d^2}$ and

$$I_\Omega = \frac{I_T}{16} \cdot \left(\frac{\Phi}{d}\right)^2 \tag{4.3}$$

In figure 4.4 we report the values of I_T as a function of d and the fit obtained using equation 4.3, where I_T is the fit free parameter.

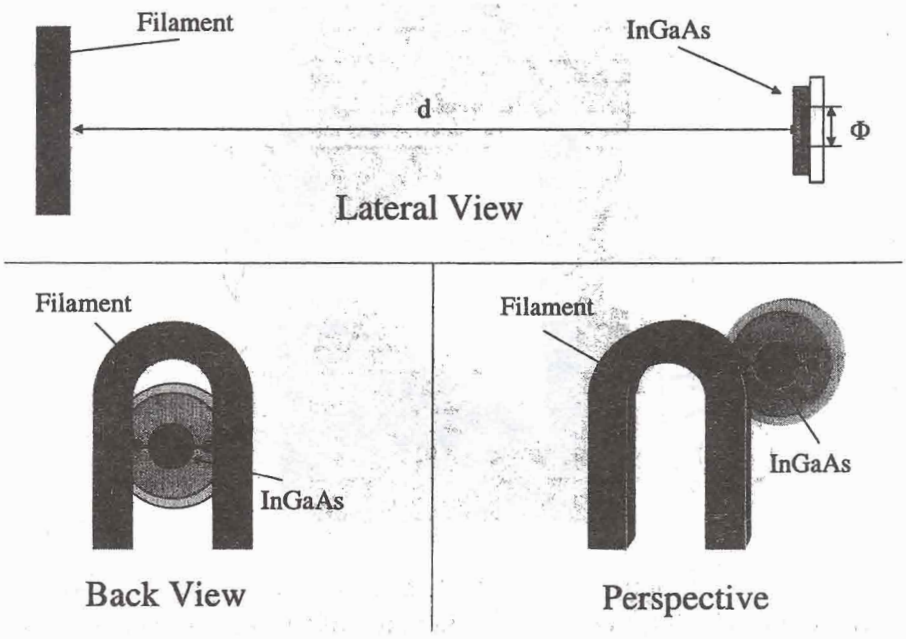

Figure 4.3: A scheme of the set up for the measurement of the light intensity emission of the filament.

The agreement of the fit with the data is sufficient to justify the assumption for the calculation of Ω.

For the method described, it is important that in the measurement of I_T and I_D the temperature of the filament be the same. The temperature was not directly under control, but just monitored by monitoring the current flowing in the filament I_f. We repeated the measurement for different values of I_f and obtained $\epsilon = 0.127 \pm 0.012$.

The alpha source is a $\simeq 1$ μCu ^{241}Am source, that emits alpha particle of either 5.4856 MeV (branching ratio = 85.2%), or 5.4429 MeV (branching ratio = 12.8%), or 5.388 MeV (branching ratio = 1.4%). The mean energy of the alpha particles is therefore 5.479 MeV. The particles enter the cavity passing through the hole of the

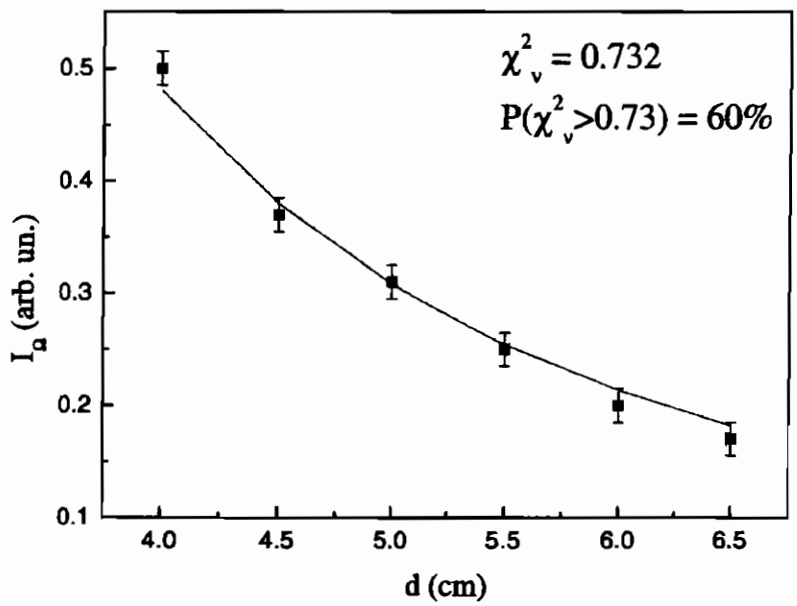

Figure 4.4: Intensity of the black body radiation emitted by the filament as a function of the distance between the filament and the photodiode. The meaning of the fit is explained in the text.

pierced base. The length of the hole is 3.0 ± 0.3 mm. Therefore, before entering the chamber, the alpha particles loose some energy scattering against the atoms contained in the hole. The energy loss over this distance, calculated according to the stopping power of gaseous Xenon reported in literature[Ber-00], is 1.08 ± 0.16 MeV, where the error is calculated considering the uncertainties on the position of the source and on the density of the gas.

The projected range of a 5.5 MeV alpha particle in gaseous Xenon at a pressure of 2 bar is $\simeq$ 1.2 cm[Ber-00], hence alpha particles that pass through the hole come completely at rest inside the cavity.

The infrared sensor is an InGaAs photodiode (G5832-05, EG&G),

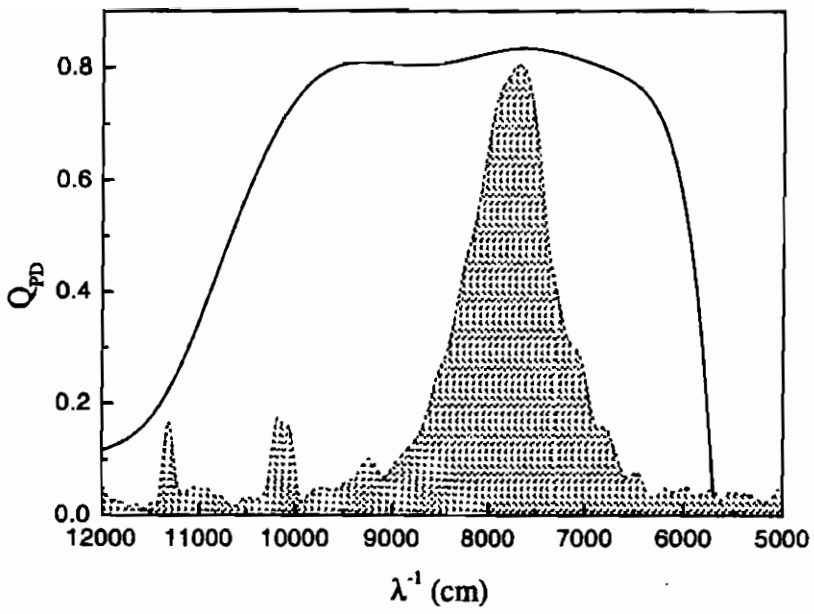

Figure 4.5: Quantum efficiency of the InGaAs photodiode (Q_{PD}) as a function of the wavenumber (λ^{-1}). The filled area is the spectrum S of particle induced infrared emission in Xenon (in arbitrary units) used to calculate the value of ϵ of equation 4.1.

whose quantum efficiency is reported in figure 4.5. The electronical read-out is the same previously used in the spectrometer described in Chapter 1 (without the shaping amplifier). For the details, we refer the reader to that chapter (see also figure 4.1, where $R_D = 10$ MΩ and $C_D = 9.4$ nF, nominal values). The photodiode and the preamplifier chain have been calibrated by measuring the output in correspondence of a light pulse emitted by a calibrated diode. The conversion factor is $G = 0.362 \pm 0.015$ mV/fC, where the error is statistically calculated from a set of different measures.

For the charge collection, a 100 μm tungsten wire is tighten 1 cm away from the large base of the cavity and connected both to

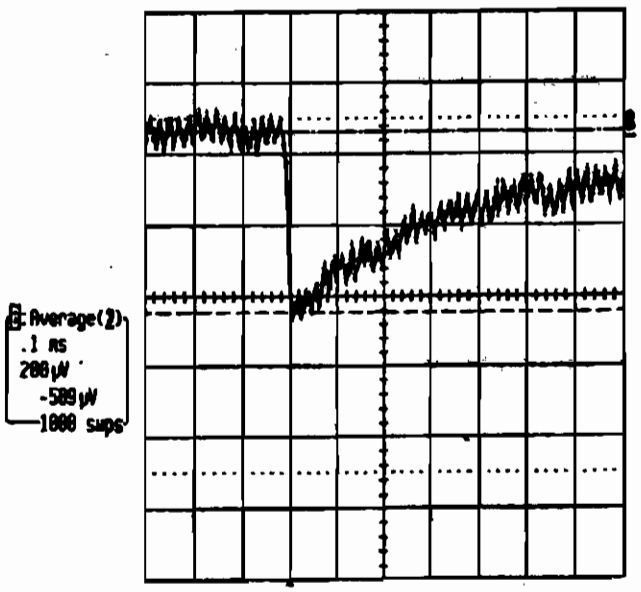

Figure 4.6: Infrared signal of an alpha particle event (1000 sweep average).

a high voltage supply and to a charge amplifier. The electronic read-out is shown in figure 4.1, with $R_{HV} = 10$ MΩ and $C_{HV} = 4.7$ nF, nominal values. The integration factor of the charge amplifier is equal to 0.25 mV/fC and its decay constant is 400 μs (nominal values). The signal is used as a trigger and its amplitude is also monitored to evaluate if charge amplification is occurring near the wire.

4.2 Prompt light yield of gaseous Xenon: results and discussion

The oscilloscope trace shown in figure 4.6 is the 1000 sweeps average of the signal detected by the photodiode in correspondence of an alpha particle event, with the wire kept at 100 V.

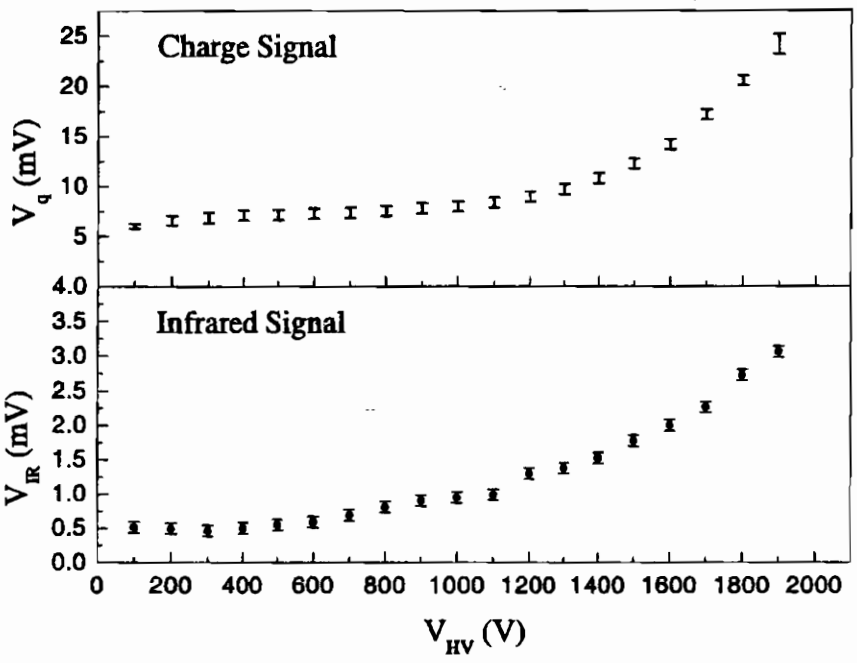

Figure 4.7: Amplitude of the charge and infrared signals as a function of the voltage applied onto the wire for a Xenon sample.

In figure 4.7 we show (i) the amplitude of the signal of the charge amplifier connected to the collection wire V_q, and (ii) the amplitude of the signal of the charge amplifier connected to the photodiode V_{IR}, as a function of the voltage applied to the wire V_{HV}. The error bars are the results of the uncertainty on the positioning of the oscilloscope cursors on the traces. The behavior of the two graphs can be divided into three intervals:

- For $V_{HV} \leq 500$ V, both V_q and V_{IR} are nearly constant. All the electrons produced in the cavity are collected by the wire[†],

[†]A small increase of V_q in the $V_{HV} \leq 300$ V region can be hardly seen. In any case, this behavior, can be ascribed to the increase of the charge collection efficiency.

but the electric field is not high enough to produce multiplication near the wire. Since the infrared signal is constant, no drift emission takes place yet.

- For 500 V< $V_{HV} \leq$ 1000 V, V_q is constant, while V_{IR} increases with the increase of V_{HV}. Since no charge multiplication occurs near the wire, the increase of V_{IR} is due to drift emission.

- For $V_{HV} >$ 1000 V, both V_q and V_{IR} increase with the increase of V_{HV}. In this interval, the electric field near the wire produces charge multiplication (see for example [Sau-77]). The increase of V_{IR} must be ascribed to the drift emission of both the electrons produced by the alpha particle and those produced in the avalanche near the wire.

In the second and third intervals, the emission of infrared light is the result of the sum of prompt and drift emission. With this experimental set up, it is not possible to separate the two contributions. For this reason, for the measurement of the prompt emission light yield, we must limit the analysis to the data with $V_{HV} \leq$ 500 V. The mean value of V_{IR} in the interval of $V_{HV} \leq$ 500 V is $V_{IR}^{mean} = 507 \pm 18\ \mu$V. The mean number of electrons produced on the photodiode is therefore $N_f = 8740 \pm 410$.

The quantum efficiency Q_{PD} of the photodiode is far to be constant in the infrared scintillation wavelength region (see figure 4.5). However, since the emission spectrum is known, it is possible to calculate the weighted mean value of Q_{PD} in the spectrum range, choosing the spectrum intensity S_n as a weighting function:

$$Q = \frac{\int Q_{PD}(\lambda^{-1}) \cdot S_n(\lambda^{-1})\, d(\lambda^{-1})}{\int S_n(\lambda^{-1})\, d(\lambda^{-1})} \simeq \frac{\sum_{\lambda^{-1}} Q_{PD}(\lambda^{-1}) \cdot S_n(\lambda^{-1})}{\sum_{\lambda^{-1}} S_n(\lambda^{-1})} \tag{4.4}$$

Note that $S_n(\lambda^{-1})$ is not exactly the spectrum $S(\lambda^{-1})$ reported in figure 4.5, because this spectrum is not normalized to the quantum efficiency Q_{FFT} of the photodiode used in the spectrometer. The normalization is performed according to:

N_f	ϵ	E (MeV)	Q
8740 ± 410	0.127 ± 0.012	4.40 ± 0.16	0.760 ± 0.020
$LY = 20600 \pm 2400$ ph/MeV			

Table 4.1: Values of the parameters used for the calculation of the light yield in gaseous Xenon. The result is $LY = 20600 \pm 2400$ photons/MeV.

$$S_n\left(\lambda^{-1}\right) = \frac{S(\lambda^{-1})}{Q_{FFT}\left(\lambda^{-1}\right)} \tag{4.5}$$

Since the photodiode used in the spectrometer is the same used for this measurement, we can assume $Q_{FFT} = Q_{PD}$. Putting equation 4.5 in equation 4.4, we obtain:

$$Q = \frac{\sum_{\lambda^{-1}} S\left(\lambda^{-1}\right)}{\sum_{\lambda^{-1}} \frac{S(\lambda^{-1})}{Q_{PD}(\lambda^{-1})}} \tag{4.6}$$

The presence of noise renders the use of equation 4.5 dangerous in regions were Q_{FFT} is close to zero. In these regions, in fact, noise can create a fictitious increase of S_n. In using 4.6, we limit the sum to λ values for which Q_{PD} is reasonably different from zero. Inserting in equation 4.6 those data for which $Q_{FFT} > 0.15$, we obtain $Q = 0.740$. Repeating the calculation with the data in the range where $Q_{FFT} > 0.25$, we obtain $Q = 0.780$. Thus, we can assume $Q = 0.760 \pm 0.020$.

In table 4.1 we summarize the values of the parameters of equation 4.1. Using these values, one obtains: $LY = 20600 \pm 2400$ photons/MeV.

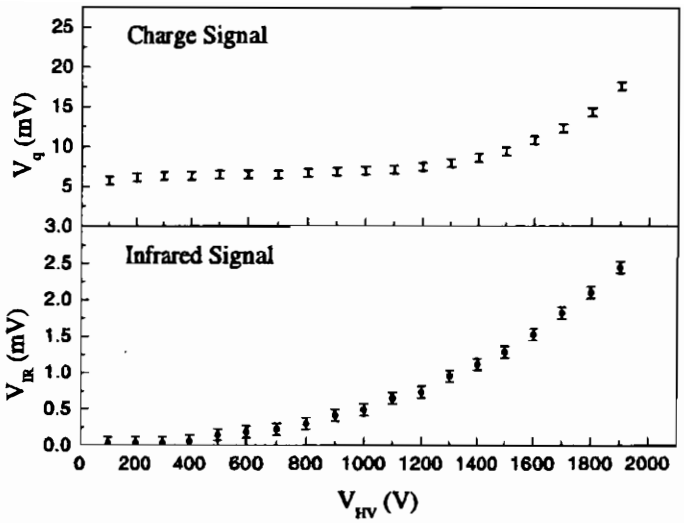

Figure 4.8: Amplitude of the charge and infrared signals as a function of the voltage applied onto the wire for an Argon sample.

4.3 Prompt light yield in gaseous Argon and gaseous Krypton

We repeated the measurements described above for gaseous Argon and gaseous Krypton. The results are shown in figure 4.8 and 4.9. Less attention was paid in evacuating the chamber before each filling procedure. Therefore, a worst purity is expected. However, the intensity of the infrared signal in both the cases is remarkably lower respect to Xenon. For low electric field values, where no drift emission takes place, the signal amplitude was within the noise level V_{noise}. Thus, using the method described in the previous section, we can only give an upper estimate of the light yield, assuming $V_{IR}^{mean} = V_{noise}$. By so doing, we obtain $LY_{Ar} < 4800$ photons/MeV and $LY_{Kr} < 4600$ photons/MeV.

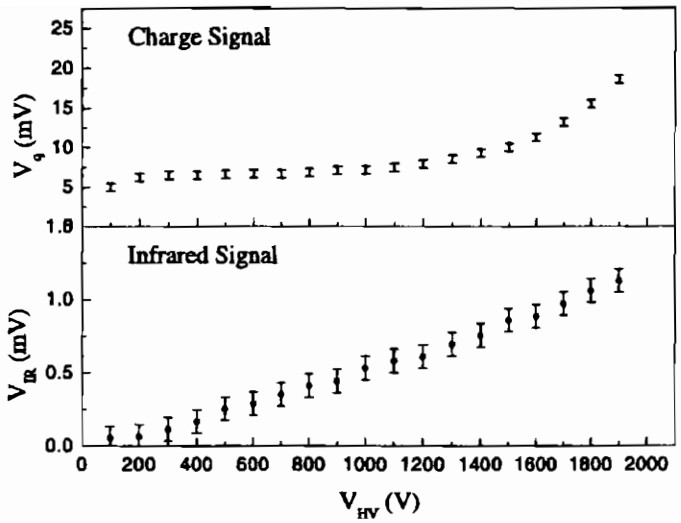

Figure 4.9: Amplitude of the charge and infrared signals as a function of the voltage applied onto the wire for an Krypton sample.

4.4 Light multiplication near a thin wire: results and perspectives

The increase of the light output as a function of the high voltage applied to the wire is extremely interesting for particle detection purposes. The amplification in the number of photons emitted could be exploited for an easier optical detection of the ionizing event. The most challenging application in this direction is, in our opinion, the development of wire chambers, microstrip chambers or gas electron multiplier (GEM) detectors where the usual electronic read-out device is replaced with an infrared camera or an infrared sensor array faced to the multiplication zone.

The use of an optical system for proportional chambers read-out provides several advantages with respect to the electronic read-out:

- When the ionization electrons are drifted over long distances

before entering the multiplication zone, electron diffusion spreads the initial cluster over several wires (in the case of wire chambers), or strips (in the case of microstrip chambers), or holes (in the case of GEMs). In this case, the reconstruction of the ionizing event[Pol-81] is usually performed by means of the center-of-gravity technique, for which electronic read-out systems show experimental spatial resolutions worse than expected [Pol-81, Sau-78]. On the other hand center-of-gravity techniques relying on optical read-out systems are known to be very efficient [Fra-00a, Sau-78].

- The optical read-out system has no multiplicity problems in the digital reconstruction of the track image. This is particularly useful in medical applications[Bar-tbp] and when the detector must be used in high counting rate conditions.

- Optical read-out assemblies are usually less complicated.

- If infrared technology will keep growing as in the past few years, with a consequent decrease of the prices of the devices, also the cost of optical read-out systems will be less expensive.

In order to understand if the optical read-out is more convenient with respect to the electronic read-out under more general circumstances, we must compare the number of information carriers that can be obtained during an avalanche with the two configurations. To do that, we can refer to the amplitude of the infrared and charge signals (V_{IR} and V_q, respectively) reported in figures 4.7, 4.8 and 4.9 as a function of the high voltage applied on the wire (V_{HV}). The number of electrons collected by the wire is given by:

$$n_e = \frac{V_q}{V_q^0} \cdot n_e^p = \frac{V_q}{V_q^0} \cdot \frac{E}{W} \tag{4.7}$$

where n_e^p is the number of primary electrons created by the alpha particle, E is the energy released, W is the $W - value$ of the gas[Lor-76], and V_q^0 is the mean value of V_q in its flat region, where

all the primary electrons are collected by the wire but no charge multiplication takes place.

The number of prompt plus secondary photons produced near the wire is given by:

$$n_f = \frac{N_f}{\epsilon \cdot Q} = \frac{V_{IR}}{G \cdot e} \cdot \frac{1}{\epsilon \cdot Q} \tag{4.8}$$

(see equation 4.1), where N_f is the (measured) number of photons detected by the photodiode (given by $\frac{V_{IR}}{G \cdot e}$, with G conversion factor of the charge amplifier and e electron charge), ϵ is the light collection efficiency, and Q is the mean quantum efficiency of the detector in the wavelength region of emission.

If $n_e > n_f$, the signal-to-noise ratio with the electronic read-out is better than the signal-to-noise ratio with the optical read-out, and vice versa. We want to stress, once more, that this statement only concerns the number of information carriers, and does not keep into account the advantages of the optical read-out reported in the list above. It is important to underline, however, that in the case of electronic read-out all the n_e electrons are collected, whereas the n_f photons are generally not all collectible and transformable in useful signal.

In figures 4.10, 4.11 and 4.12, we show n_e and n_f (normalized to $E = 1$ MeV) as a function of V_{HV}. It is evident that electronic read-out is to be generally preferred because of its better signal-to-noise ratio. However, we want to stress an important detail of this result. Generally speaking, in order to obtain charge multiplication, high electric field must be applied, which can be obtained only around small volumes near sharp electrodes. Light multiplication, on the contrary, does not require very high electric fields, as shown by our data (V_{HV} interval between 500 V and 1000 V). Lower electric field can be applied over long distances without discharge problems. In this way, since the number of photons produced by drift emission is proportional to the drift distance, higher values of light multiplication can be achieved. This could be particularly useful in applications for which space-charge effects associated with large

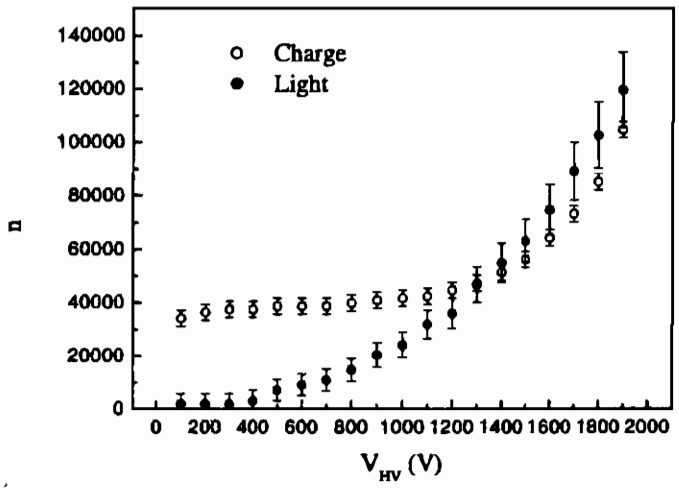

Figure 4.10: Number of information carriers produced in Argon as a function of the voltage applied for a 1 MeV event.

avalanches require to keep the charge gain very low[Pol-81, Sau-77].

Since several advantages could be obtained with the optical read-out, we have realized a first prototype of a particle detector based on secondary enhanced infrared scintillation. A schematic view of the detector is shown in figure 4.13. It mainly consists of a metallic box, filled with the gaseous scintillator and equipped with a copper plate cathode and a grid anode. The grid is made by 100 μm tungsten wires crossed with a 2 mm pitch. The infrared photons produced by prompt and amplified scintillation pass through a quartz window, that also filters out vacuum-ultraviolet scintillation photons. A Silicon camera (Find-R-Scope 89000L, FJW Optical systems) is faced to the quartz window and connected to a personal computer for the image storage. Its spectral sensitivity ranges from 400 nm to 1300nm.

We tested this set-up exciting the gas with a 3 MeV proton beam, extracted from a Van der Waals linear accelerator (Labo-

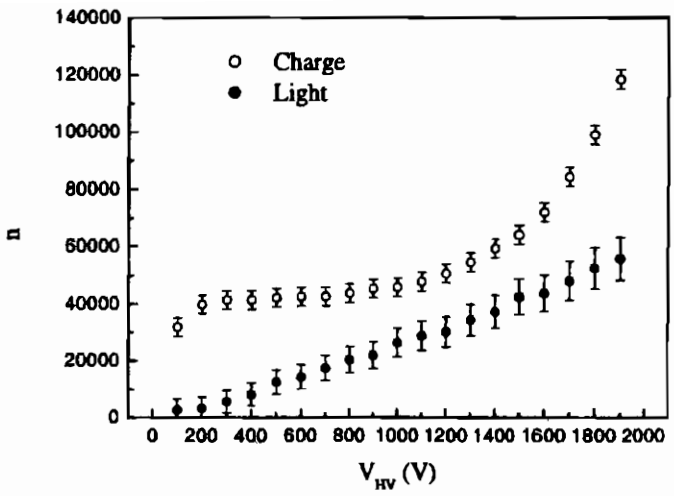

Figure 4.11: Number of information carriers produced in Krypton as a function of the voltage applied for a 1 MeV event.

ratori Nazionali di Legnaro, Istituto Nazionale di Fisica Nucleare, Legnaro, Padova, Italy) and chopped into 80 μs long bunches. In figure 4.14 we show the track of a bunch obtained with the chamber filled with pure Argon at 1 bar. Similar detectors will be soon tested with an InGaAs CCD optical read-out system, whose quantum efficiency is much higher in the infrared region of interest.

4.5 Conclusions

The light of prompt infrared scintillation in gaseous Xenon at room temperature and nearly atmospheric pressure is very promising for the future development of infrared scintillation particle detectors. Argon and Krypton show less interesting prompt scintillation properties.

The amplification of scintillation light by means of relative low

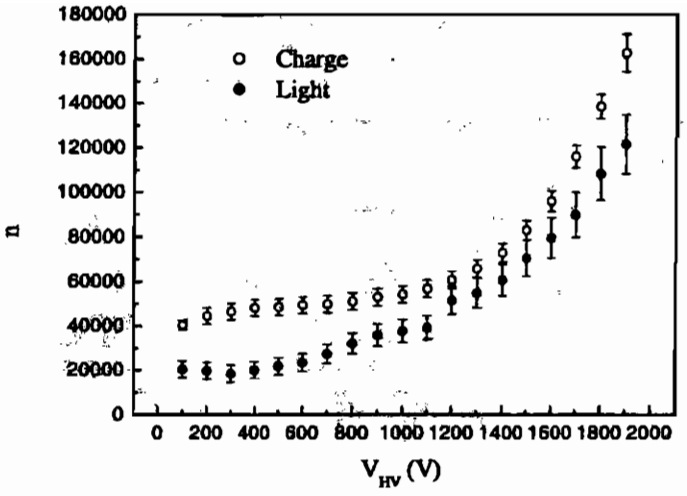

Figure 4.12: Number of information carriers produced in Xenon as a function of the voltage applied for a 1 MeV event.

electric field can be exploited for the development of proportional chambers with optical read-out, with particular reference to Argon. Although the gain in the number of photons is not as large as in the case of electronic read-out, optical read-out has several advantages in the development of high resolution position sensitive detector convenient, for example, for imageology[Fra-00b].

Another application of secondary scintillation could be the identification of defects in microstructures[Fra-00b]. The light emission is in fact correlated with the local electric field seen by the drifting electrons, that strongly depends on surface irregularities.

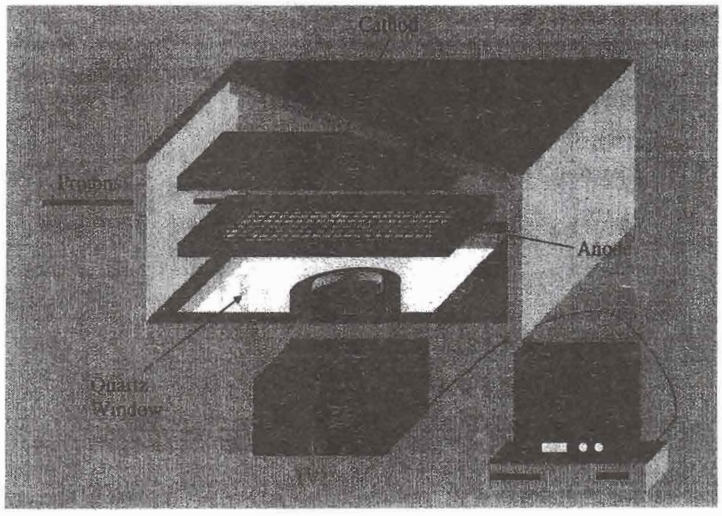

Figure 4.13: A schematic view of the first prototype of a proportional chamber with an optical read-out.

Figure 4.14: Track of a 3 MeV proton bunch obtained with a prototype of a wire chamber with optical read-out.

Chapter 5

Particle induced infrared emission in noble liquids and crystals.

Introduction

In the previous chapters we have put into evidence that the use of noble gases as infrared scintillators (with particular reference to Xenon) should be seriously taken into account for the design of future particle detectors. It is then reasonable to rise the question if other materials exist which efficiently convert the energy of an ionizing radiation into infrared photons. In this chapter we show the results of our experimental measurements aimed to answer this question.

In the first section we report on particle induced infrared emission in liquid Argon and Xenon, while the second section is devoted to the results obtained with several crystal samples.

5.1 Particle induced infrared emission in liquid Argon and Xenon

5.1.1 Overview

As already pointed out, our study of infrared emission from gaseous noble elements excited by charged particles was aimed to (i) better understand the fundamental mechanisms in the interaction of charged particles with matter, and to (ii) search for unexplored possibilities in the development of radiation detectors based on particle induced infrared emission rather than visible or ultraviolet scintillation. The same goals have been pursued in the study of particle induced infrared emission in noble liquids. In the light of the results reported in the previous chapters, we focused our attention on the following items:

- In order to verify that in the liquid phase radiative decays are not completely quenched by inelastic collisions among atoms, whose frequency increases as the density is increased, it is necessary to verify that infrared prompt emission still takes place.

- If the prompt emission takes place, it is interesting to understand if the spectrum of liquid Xenon is still dominated by the broad excimer band, or if this emission is suppressed by inelastic collisions among atoms and excimers, whose frequency increases as the density is increased (see Chapter 2).

- It is also important to understand if drift emission takes place in liquid phase. The increase of the collisional frequency among drifting electrons and atoms, or, in other words, the decrease of the mean free path of the electrons, should be so dramatic that even under a very high electric field the fraction of electrons with an energy higher than the first atomic excited state is negligible small. If this is the case, no drift emission should be observed (see Chapter 4).

- Finally, a direct measurement of the light yield is necessary to understand if noble liquids can be successfully used as infrared scintillators.

For these reasons, we measured the light output of particle excited noble Argon and Xenon in the infrared wavelength region. A rough measurement of the emission spectrum was also performed, as well as the measurement of the light output in the presence of a high electric field inside the liquid sample. In this section we describe the experimental details and present the results obtained.

5.1.2 Experimental apparatus

In figure 5.1 we show the experimental apparatus used for the study of particle induced infrared emission in noble liquids. A particle beam excites the liquid sample contained into a cryogenic ionization chamber. The infrared light produced by the particles in the liquid is detected by an infrared photodiode. In order to measure also the drift emission light, a metallic wire, tightened in the middle of the chamber, is connected to a positive power supply.

To excite the liquid we use either electrons or protons. In the first case, the beam is extracted from the electron gun already described. For the details of this experimental apparatus, we refer the reader to Chapter 1. In the second case, the proton beam is extracted from a Van deer Waals linear accelerator (Laboratori Nazionali di Legnaro, Istituto Nazionale di Fisica Nucleare, Legnaro, Padova, Italy). The energy of the protons is 5 MeV and the current of the continuous beam is approximatelly 1 nA. The beam is bunched by means of a rotating metallic chopper, machined as reported in the inset of figure 5.1. The wheel rotates at a frequency of about 140 Hz. A 30 μs bunch is followed by a 400 μs bunch, and viceversa.

The ionization chamber (see figure 5.2) is a cubic stainless steel cell with an internal volume of approximatelly 4 cm^3. The particles enter the chamber passing a kapton window orthogonal to the beam direction. The diameter of the window is 3 mm. The thickness of

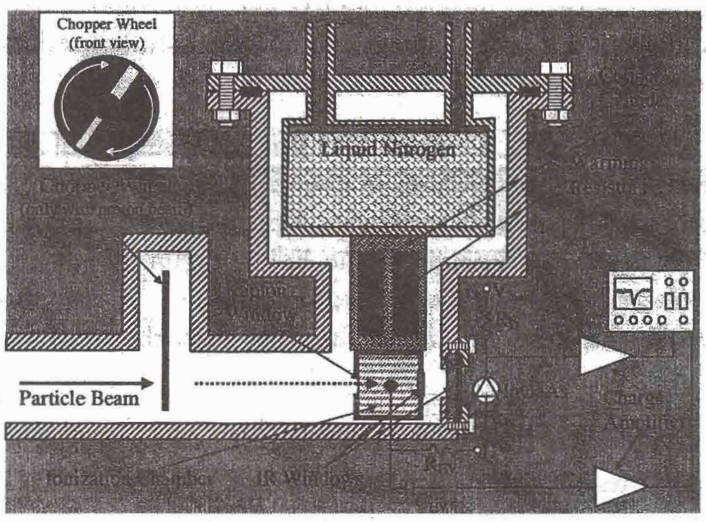

Figure 5.1: A scheme of the experimental apparatus for the measurements in noble liquids. See also figure 5.2.

the kapton foil is 125 μm when protons are used or 13 μm when electrons are used. The light exits the chamber passing through a 3 mm thick sapphire window. In figure 5.3 we report the transparency of sapphire according to [Hud-69]. Concerning the distance between the entrance window and the exit window, we used two different configurations: (i) 30 mm, and (ii) 3 mm. In the first case, in the middle of the chamber we also placed a 10 μm diameter metallic wire, orthogonal with respect to the beam. The wire is connected both to a positive power supply and to a charge amplifier[Bac-86] as shown in figure 5.2 (R_{HV} = 10 MΩ, C_{HV} = 4.7 nF, nominal values). The integration factor of the charge amplifier is equal to 0.25 mV/fC and its decay constant is 400 μs. The output of the amplifier is sent to a digital oscilloscope for the measurement of the charge collected by the wire.

The chamber is thermally coupled to a copper cylinder mounted on the bottom of a liquid nitrogen vessel (see figures 5.1 and 5.2).

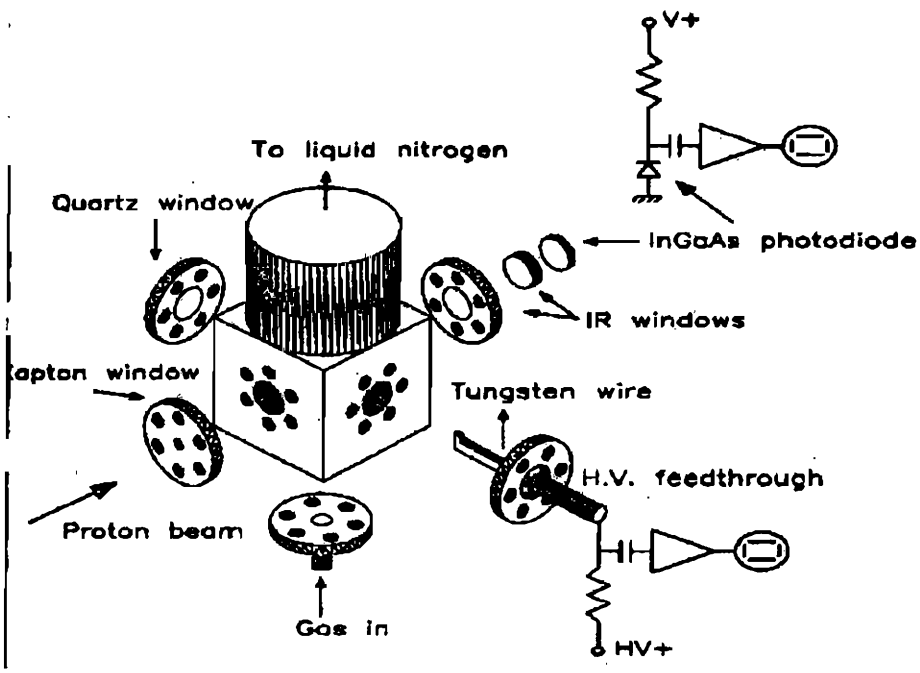

Figure 5.2: Schematic view of the ionization chamber for the measurements in noble liquids.

The chamber, the cylinder, and the vessel are completely contained inside the beam pipe and covered with several aluminized mylar sheets, to reduce heat exchanges with the environment. The temperature of the chamber is measured by measuring the resistance of a calibrated platinum resistor glued to the cell. The minimum temperature achievable is 95 K. In order to regulate the working temperature at values higher than 95 K, two warming resistors are fixed to the copper cylinder and connected to a power supply.

The chamber is also connected to a vacuum system (membrane pump plus turbomolecular pump) and to a filling system, equipped with a purifier cartridge (Oxisorb, Messer). Before each filling, the chamber is evacuated down to 10^{-5} mbar and cooled down to the working temperature by inserting liquid nitrogen into the vessel and

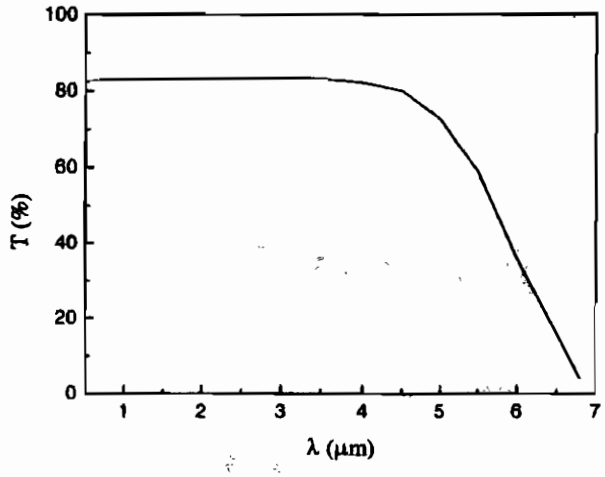

Figure 5.3: Transparency of a 2 mm thick sapphire window[Hud-69].

by adjusting the current flowing into the resistors. Once the working temperature is reached, we insert Argon or Xenon in gaseous phase inside the cooled chamber, at a pressure higher than the boiling pressure. The gas is forced to pass into the purifier cartridge before entering the chamber. A purity of the order of 10 part per million (or even better) is expected with this technique[Buc-89]. Since the gas inside the chamber has a pressure higher than the boiling pressure, the gas condensates to liquid phase. A quartz window allows to verify the presence of the liquid inside the chamber (see figure 5.2). The light that exits from the chamber passes another 3 mm thick sapphire window and hits an InGaAs photodiode (G5832-05, EG&G). The photodiode and its electronical readout are the same previously used in the spectrometer described in Chapter 1 (without the shaping amplifier). For the details, we refer the reader to that chapter (see also figure 5.1, where $R_D = 10$ MΩ and $C_D = 4.7$ nF, nominal values).

We shall show that in the case of noble liquids, with our ex-

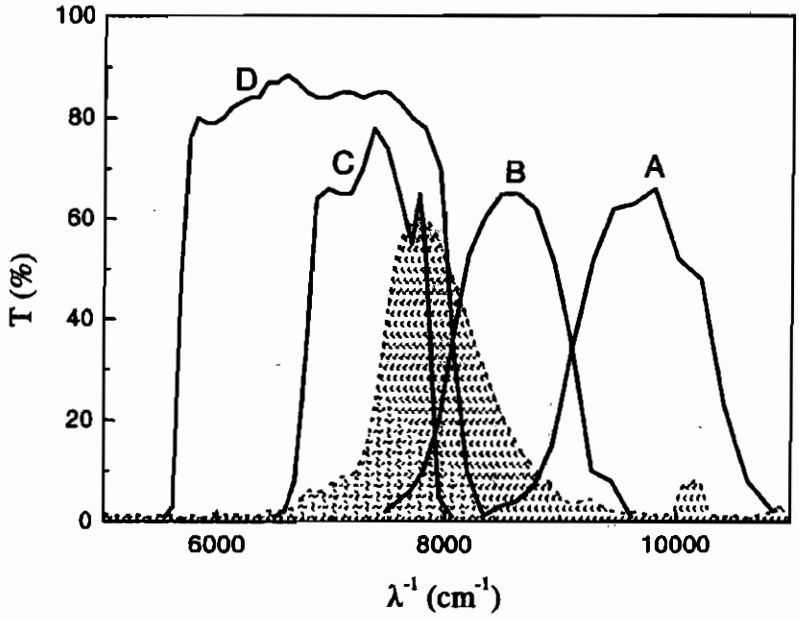

Figure 5.4: Transparency of the optical filters for a rough measurements of spectra in noble liquids. The dashed line rapresents the spectrum of gaseous Xenon that we used to test the method described in the text.

perimental set-up, it is not possible to measure the spectrum with the FFT spectrometer described in Chapter 1. However, in order to obtain a rough measurement of the spectrum, it is possible to insert optical filters with different bandpass between the chamber and the detector. The transparency of the four filters is reported in figure 5.4.

5.1.3 Results and discussion

In figure 5.5 we show the signal of the InGaAs photodiode obtained in correspondance of three proton bunches in liquid Argon (trace

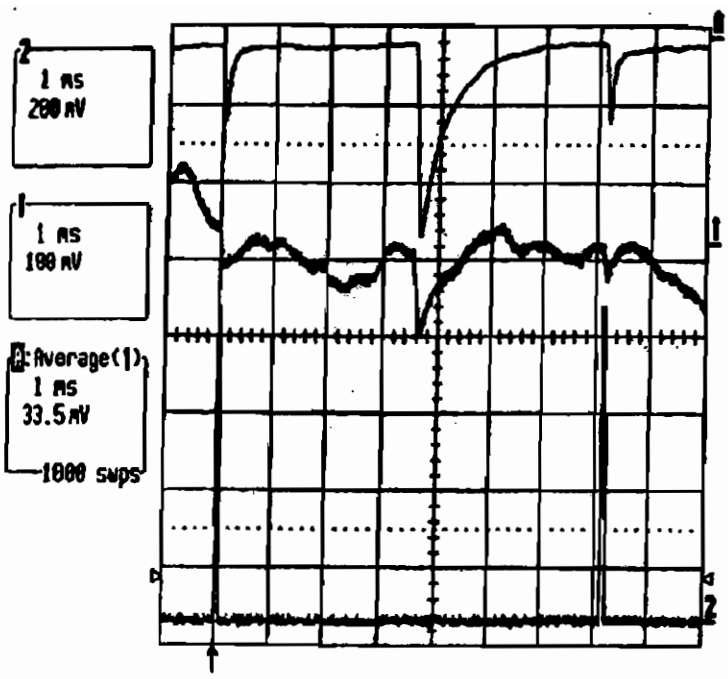

Figure 5.5: The infrared signals produced by three proton bunches. The meaning of the traces is explained in the text.

1). The two smaller lateral spikes correspond to 30 μs bunches, while the central one corresponds to a 400 μs bunch. Trace A is the average of 1000 of these signals, while trace 2 is a trigger signal. Similar results have been obtained in liquid Xenon. This proofs that the prompt emission takes place also in liquid Argon and Xenon.

In figure 5.6 we show (i) the charge collected by the wire, and (ii) the light output in liquid Argon excited by protons as a function of the high voltage applied on the wire. The uncertainty on the data is dominated by the fluctuations in the proton beam intensity, and it is equal to 10%. The charge collected by the wire reaches a plateaux value for voltages higher than 5 kV. For lower values, the electric field is not high enough to drive all the electrons to the wire. From figure 5.6, it is evident that no drift emission is observed. Similar

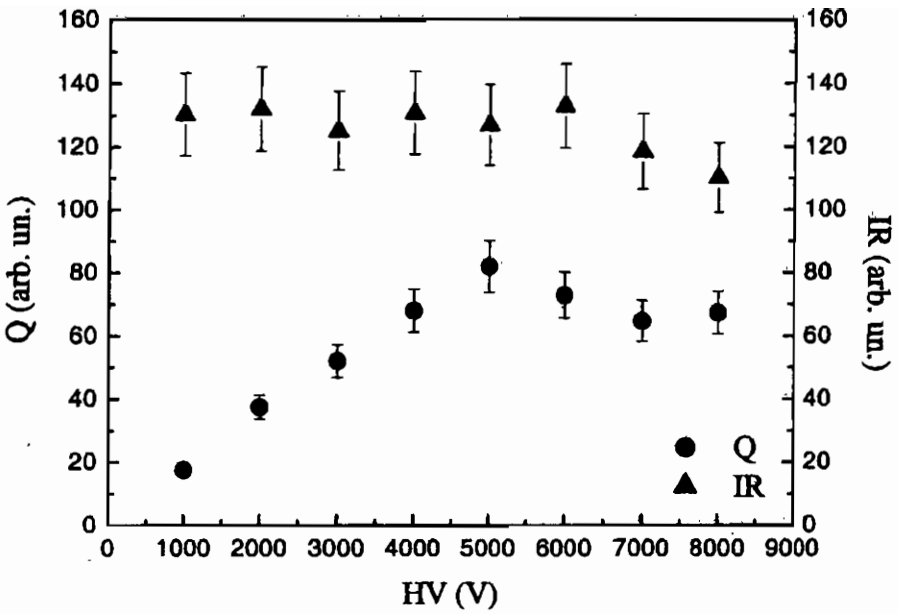

Figure 5.6: Infrared signal amplitude (IR) and charge signal amplitude (Q) in proton excited liquid Argon as a function of the voltage applied.

results were obtained in Xenon. We can conclude that, since in the liquid the electron-atom collision rate is much higher with respect to the gas (or, in other words, the mean free path is much smaller), the energy that the electrons can gain by the field between two collisions in liquid is so small that does not influence the energy distribution function of the electrons.

Since the measurements of the light yield in gaseous samples show that Xenon could be an interesting infrared scintillator, we decided to measure the infrared light yield also in liquid Xenon. To this purpose, we first filled the chamber with Xenon gas at room temperature and nearly atmospheric pressure and measured the signal on the photodiode. Then we filled the chamber with liquid

Xenon and measured again the signal on the photodiode. The signal obtained from the liquid is more than a factor 200 lower than the signal obtained from the gas. In principle, this could be ascribed either to (i) a lower light yield or (ii) to a worst light attenuation length of the liquid with respect to the gas. For this reason, we made the measurement with the two set-ups with different entrance-to-exit distances (30 mm and 3 mm), and, therefore, with different light paths. Since we obtained the same results in the two cases, we can claim that the light yield in liquid Xenon is nearly a factor 200 lower than the one of gaseous Xenon. Similar results were obtained in liquid Argon.

In order to understand if the excimer peak observed in gaseous Xenon is still present in liquid Xenon, we also measured the spectrum of the emission in liquid Xenon. Since the signal is too small to use the spectrometer, we used four optical filters. The measure was performed according to the following scheme:

1. We calculated the amplitude of the signal we should expect for each of the filters in the case of gaseous Xenon (room temperature and nearly atmospheric pressure) using the spectrum obtained with the spectrometer and the nominal transparency of the filters (figure 5.4).

2. To test the method, we filled the chamber with gaseous Xenon at room temperature and nearly atmospheric pressure, and measured the light output without any filter (V_{tot}) and inserting, one at time, each filter ($V_A, ..., V_D$).

3. We calculated the ratio $\frac{V_X}{V_{tot}}$, with $X = A, ..., D$.

4. We filled the chamber with liquid Xenon and repeated steps 2 and 3.

In table 5.1 we report the results obtained exciting the sample with electrons. The experimental data of gaseous Xenon are in a reasonable agreement with the calculations, given the roughness of the method. On the contrary, it is evident that, in the case

	Expected in gas	Measured in gas	Measured in liquid
A (980 nm - 1100 nm)	4%	12%	11%
B (1100 nm - 1240 nm)	14%	15%	7%
C (1280 nm - 1480 nm)	34%	25%	4%
D (1240 nm - 1760 nm)	58%	44%	12%

Table 5.1: Rough measurement of the spectrum in liquid Xenon. In the first column we report the range in which the transparency of the filters is higher than 50%, for a quick analysis of the results.

of the liquid, the signals obtained with the two filters at higher wavelengths (filters C and D) are much more smaller. Since the region in which these two filters are transparent is the excimer peak region, we can conclude that the excimer peak is suppressed in the liquid phase. We ascribe the suppression to the dominance of non-radiative decays, induced by the increase of the excimer-atom inelastic scattering rate.

5.1.4 Conclusions

The measurements in liquid Argon and Xenon show that prompt emission induced by particle beam is also present in noble liquids. However, the light yield is of the order of 100 photons/MeV. Furthermore, since no drift emission is observed, no amplification of the light signal can be used to increase the effective light yield. For these reasons, application of particle induced infrared emission in noble liquids for particle detection is not realistic.

5.2 Particle induced infrared emission in crystal samples

5.2.1 Overview

Visible and ultraviolet scintillating crystals are often prefered to liquid or gaseous scintillators because of their higher density and easier assembly properties. For this reason, we have been searching for solid materials whose particle induced infrared emission could be similarly used as infrared scintillation light. Our approach is essentially aimed to identify high light yield crystals by exciting several candidates and focusing our efforts on the ones with the highest light output. In this section we present the results obtained so far.

5.2.2 Experimental evidence of particle induced infrared emission in crystals

The first step in the study of particle induced infrared emission in crystals was to identify samples with high light output. To do that, we used the experimental apparatus drawn in figure 5.7. The crystal is faced to a 10 μm thick Kapton window mounted at the exit of the 5 MeV proton beam line described in the previous section. The bunches are 80 μs long and are collimated by a 2 mm diameter collimator that is also used to monitor the beam intensity. A 1 mm^2 HgCdTe infrared sensor (HCT-12.5-1.0, Graseby Infrared), sensitive in the wavelegth region between 1 and 15 μm, is faced to the opposite side of the crystal. Its quantum efficiency between 1 and 12 μm is higher than 65%. The detector is kept inside a dewar vessel and cooled down to liquid nitrogen temperature to reduce electronic noise. Just in front of the dewar, a pure Silicon slice is placed to filter out the radiation with wavelength smaller than 1.2 μm. The HgCdTe signal is read by a 1 MHz bandwidth current amplifier (DP-8000, Graseby Infrared) and sampled by a digital oscilloscope.

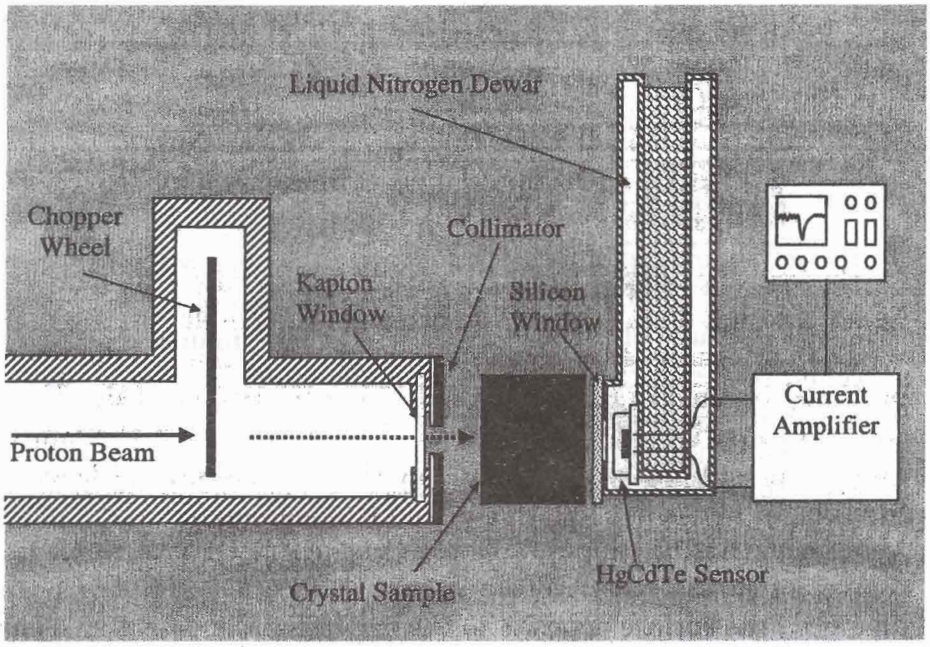

Figure 5.7: A schematic view of the experimental apparatus for the preliminary investigation of particle induced infrared emission in crystals.

By means of this apparatus, we tested approximatelly thirty different samples. All the investigated crystal are transparent to infrared light. Most of them scintillates in the visible or ultraviolet region, with a light yield which indicates that only a small fraction of the deposited energy is converted to light in this frequency range, hence suggesting that other emission mechanisms might take place. The list of the samples investigated is given here below.

Si	Ge	Quartz
CsI	CsI(Tl)	NaI(Tl)
BGO	PWO	PbF_2
BaF_2	$BaF_2(NdF_3)$	$BaY_2F_8(Ho)$

Al_2O_3	Al_2O_3(Ti)	CdI_2
GaAs	GaAs(Cr)	GaAs(Zn)
ZnSe	ZnSe(Te)	CeF_3
AgCl	AgBr	ThF_4
$LiNbO_3$(Er)	$LiYbF_4$(HoTm)	$LiYF_4$(Nd)
MgF_3(Ni)	$Y_2SiO_5(Tb^{3+})$	$Bi_{12}GeO_20(Eu^{3+})$
$KZnF_3$(Cr)	YAG(Yb)	

By way of example, in figure 5.8 and 5.9 we show the emission signal obtained from some of the investigated samples.

The amplitude of the signals reported in the figures is not proportional to the infrared light yield of the relative crystals. For a correct comparison of the signals, we must consider that the dimensions of the samples strongly influence the light collection efficiency. In order to normalize the signals to this geometrical contribution, we assume that the infrared photons are generated by a point-like source set in the center of the sample surface faced to the beam pipe (i.e., the surface opposite to the one facing the detector). This assumption is based on the fact that the range of 5 MeV protons in crystals is generally smaller than 100 μm. The most important contribution to the collection efficiency is the solid angle between the point-like source and the detector, that can be easily calculated once the dimensions of the sample are known. In table 5.2 we report the normalized signal amplitude for the most interesting samples. The values are given in arbitrary units, common to all samples. Beam current fluctuations are the most relevant contribution to the error in those measurements, that is approximatelly equal to 10%. The crystals that are not reported in the table have a normalized amplitude smaller than 1 (in the same arbitrary unit), except for YAG(Yb), whose signal is more than one order of magnitude higher respect to CsI(Tl), and whose properties will be discussed in the next subsection.

Figures 5.8 and 5.9 deserve another comment. The time behavior of the light signals is different from sample to sample. However, the $\simeq$ 80 μs long shape of many signals is due to the proton bunch shape and not to long scintillation times of the crystals. On the

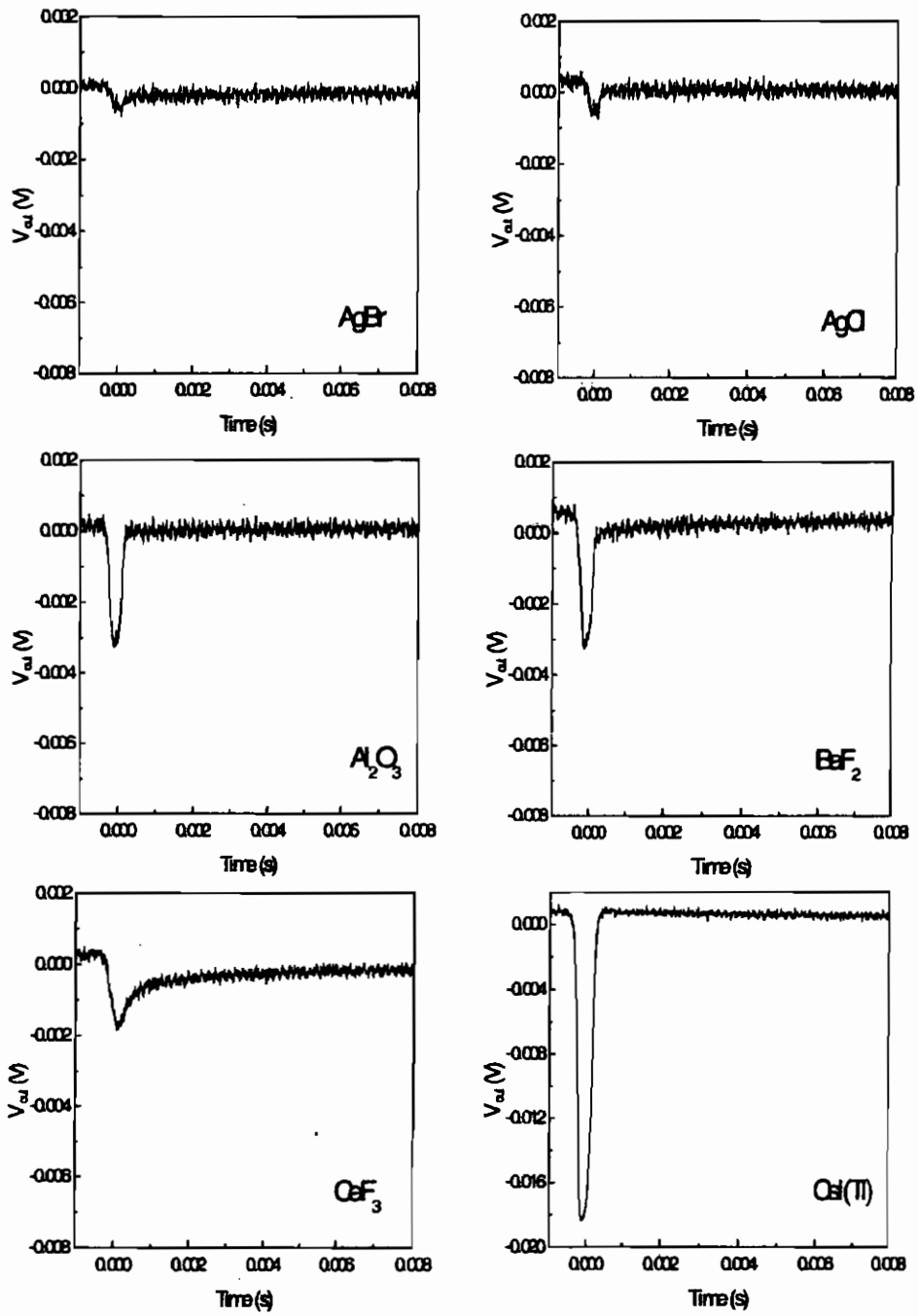

Figure 5.8: Particle induced infrared emission in some crystals.

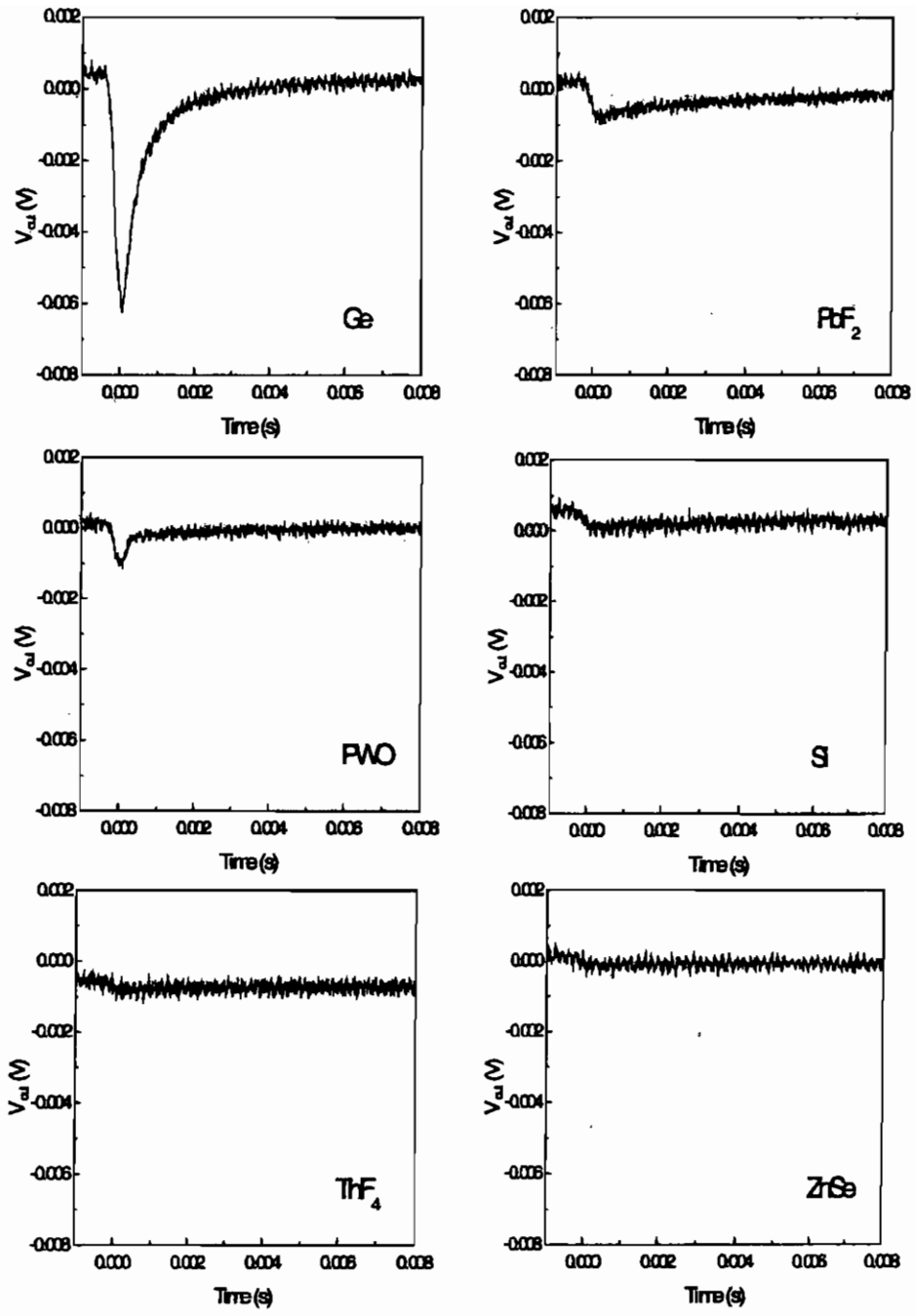

Figure 5.9: Particle induced infrared emission in some crystals.

Sample	IR signal (arb. un.)
CsI(Tl)	100
Al_2O_3(Ti)	83
$KZnF_3$(Cr)	64
$LiYF_4$(Nd)	22
Ge	12
CeF_3	4
BaF_2	3
NaI(Tl)	3
PWO	2
PbF_2	1

Table 5.2: Infrared emission amplitude of the most interesting crystals. The error in the values is approximatelly equal to 10%.

contrary, longer tails (like, for example, in Ge) must be ascribed to slow components in the scintillation time.

The samples reported in table 5.2 with an emission intensity higher than 50 were also cooled by immersion in liquid nitrogen and then exposed to the proton beam. The temperature was poorly under control and it was measured to be -100 ± 40 C. In spite of the roughness of the method, we observed that the light output of CsI(Tl) and $KZnF_3$(Cr) do not depend on temperature within the experimental uncertainty ($\simeq$10%). On the contrary, the signal amplitude of the cooled Al_2O_3(Ti) sample increases by a factor of 2.

5.2.3 CsI(Tl) and YAG(Yb): a more detailed study

The keystone in the application of particle induced infrared emission for the detection of ionizing radiation is the scintillation light

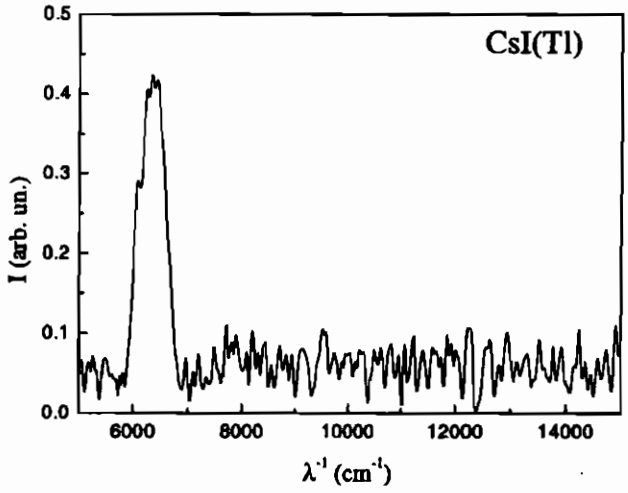

Figure 5.10: Spectrum of particle induced infrared emission in CsI(Tl).

yield. For this reason we focused our attention on the measurement of the light yield infrared scintillation in CsI(Tl) and YAG(Yb), i.e. the two samples of the previous list with the higher emission intensity at room temperature.

For the measurement of the light yield it is firstly necessary to measure the spectrum, as it will be evident below. The measurement of the spectra was obtained by means of the experimental apparatus described in Chapter 1. The results are shown in figures 5.10 and 5.11[†]. For YAG(Yb) we obtained the well known emission laser emission spectrum[Bas-95, Buc-67]. The emission observed with CsI(Tl) is yet unexplained, although the same result was already observed under X-ray irradiation[Tak-96].

In order to measure the light yield of CsI(Tl), we compared the infrared component of the scintillation light to its well known

[†]The spectrum of the YAG(Yb) was also used to calibrate the whole experimental apparatus, as already explained in Chapter 1.

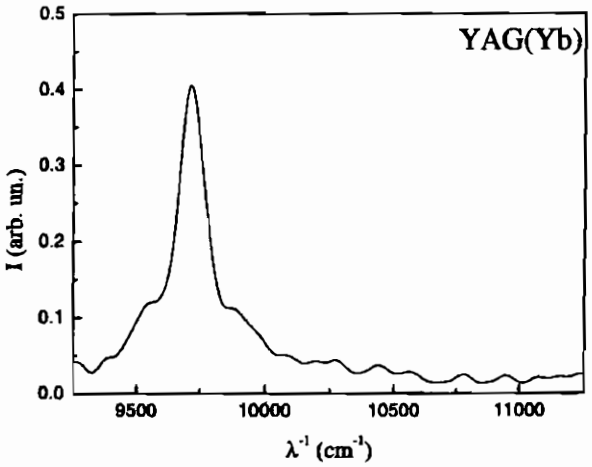

Figure 5.11: Spectrum of particle induced infrared emission in YAG(Yb).

visible component[Val-93], whose spectrum is shown in figure 5.12.

For this measurement we placed an infrared sensor directly in front of the light exit window of the electron gun beam pipe. Inside the beam-pipe, in contact with the light exit window, we placed a $3 \times 4 \times 10$ mm^3 CsI(0.01% Tl) polished sample. The light sensor is an extended InGaAs photodiode (J18TE1-37S, EG&G), connected to the usual electronic read out circuit (see figure 5.1 and the description in Chapter 1). Its quantum efficiency, plotted in figure 5.13, is higher than 30% in the wavelength region between 400 nm and 2500 nm. So, the photodiode detects both the visible and the infrared components of the scintillation light. By cutting out the visible component with an optical filter and comparing the result without and with the filter, one can measure the light yield in the infrared region.

In figure 5.14 we report the transmittance of the optical filter we used. The amplitude of the signal of the photodiode without and with the filter is given by (respectively):

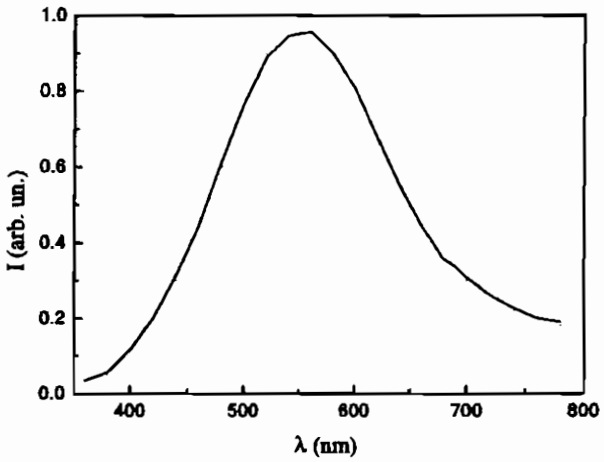

Figure 5.12: Visible scintillation spectrum of CsI(Tl), according to [Val-93].

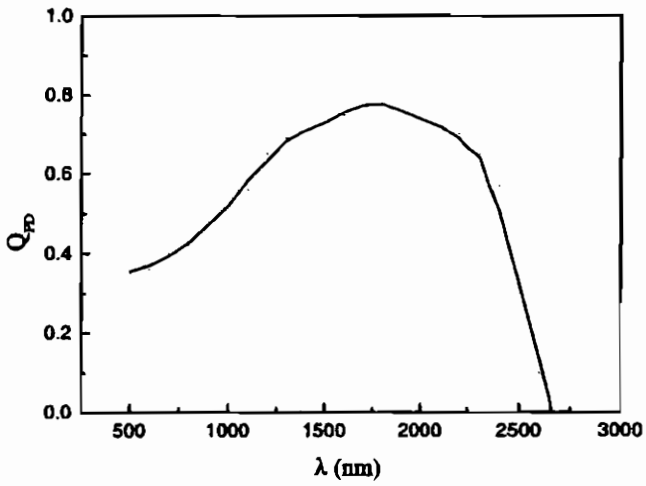

Figure 5.13: Quantum efficiency of the extended-type InGaAs photodiode

$$A_t \propto Y_{IR} \cdot Q_{IR} + Y_V \cdot Q_V \tag{5.1}$$

$$A_f \propto T \cdot Y_{IR} \cdot Q_{IR} \tag{5.2}$$

where Y_{IR} is the (unknown) infrared scintillation light yield, $Y_V = 64800 \pm 3200$ photons/MeV[Val-93] is the visible scintillation light yield, $Q_{IR} = 0.750 \pm 0.020$ is the average quantum efficiency of the photodiode over the infrared part of the scintillation spectrum (see figures 5.10 and 5.13), $Q_V = 0.3650 \pm 0.0050$ is the average quantum efficiency of the photodiode over the visible part of the scintillation spectrum (see figures 5.12 and 5.13), and $T = 0.825 \pm 0.035$ is the average transmittance of the filter over the infrared part of the scintillation spectrum[††].

From equations 5.1 and 5.2, one gets:

$$Y_{IR} = \frac{Y_V \cdot Q_V}{Q_{IR}} \cdot \frac{1}{T \cdot \frac{A_t}{A_f} - 1} \tag{5.3}$$

From the results of our measurement $A_t = 670 \pm 20$ mV and $A_f = 77 \pm 2$ mV, we obtain $Y_{IR} = 5100 \pm 470$ photons/MeV.

From this value, we can argue that the infrared light yield of all the samples we have investigated (except YAG(Yb)) is lower than $\simeq 5000$ photons/MeV (see table 5.2).

The measurement of the YAG(Yb) infrared scintillation light yield was obtained with a method similar to the one described above.

The experimental set up is identical to the previous one, except for the infrared sensor, that, in this case, is a Si photodiode (S1337-1010BQ, Hamamatsu), whose sensistivity ranges from 190 nm to

[††] T was calculated by means of:

$$T = \frac{T_M + T_m}{2} \pm \frac{T_M - T_m}{2}$$

where T_M and T_m are the maximum and minimum value of T within the *full width half maximum* range of the emission spectrum. The same method was used to calculate Q_V and Q_{IR}.

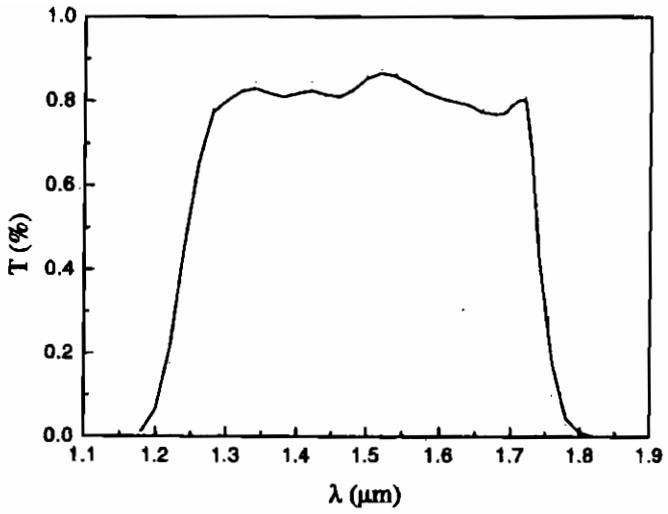

Figure 5.14: Transparency of the filter used for cutting out visible scintillation in the measurement of CsI(Tl) infrared scintillation light yield.

1100 nm. The photodiode is reversed biased by means of a +30 V applied voltage through a RC circuit configured as in the experimental set-up already described, with $R = 10$ MΩ and $C = 10$ nF (nominal values). The capacitance is not connected to a charge amplifier but directly to a high impedance (1 MΩ) channel of a digital oscilloscope. At the end of the beam pipe, either the previously described CsI(Tl) sample or a YAG(10% Yb) sample (same geometrical shape) can be excited. In front of the Si photodiode, it is possible to insert an optical filter (Oriel 57539) that is transparent only for wavelengths higher than 750 nm. In this way it is possible to cut out visible or ultraviolet components of the scintillation signal. The light yield of the YAG(Yb) is measured by comparison between the signal of the CsI(Tl) and the signal of the YAG(Yb), according to the following scheme:

- Measurement of the light output from CsI(Tl) without any filter ($A_{t(CsI(Tl))}$).
- Measurement of the light output from CsI(Tl) with the filter ($A_{f(CsI(Tl))}$) (that correspond to the infrared component of the scintillation signal).
- Calculation of the hypothetical light output in the visible region $A_{V(CsI(Tl))} = A_{t(CsI(Tl))} - A_{f(CsI(Tl))}$.
- Measurement of the light output from YAG(Yb) with the filter ($A_{f(YAG(Yb))}$).
- Calculation of the infrared scintillation light yield in YAG(Yb) by means of

$$Y_{IR(YAG(Yb))} = Y_{V(CsI(Tl))} \cdot \frac{A_{f(YAG(Yb))}}{A_{V(CsI(Tl))}} \cdot \frac{Q_{V(CsI(Tl))}}{Q_{IR(YAG(Yb))}} \quad (5.4)$$

where $Y_{IR(YAG(Yb))}$ is the (unknown) infrared scintillation light yield of YAG(Yb), $Q_{V(CsI(Tl))} = 0.659 \pm 0.028$ is the average quantum efficiency of the photodiode over the visible part of the scintillation spectrum of CsI(Tl), $Q_{IR(YAG(Yb))} = 0.435 \pm 0.047$ is the average quantum efficiency of the photodiode over the infrared part of the scintillation spectrum of YAG(Yb), and $Y_{V(CsI(Tl))} = 64800 \pm 3200$ photons/MeV is the visible scintillation light yield of CsI(Tl)[Val-93].

From our measurements ($A_{t(CsI(Tl))} = 69.9 \pm 1.4$ pC, $A_{f(CsI(Tl))} = 1.39 \pm 0.02$ pC, and $A_{f(YAG(Yb))} = 52.2 \pm 1.1$ pC) the infrared light yield of YAG(Yb) turns out to be $Y_{IR(YAG(Yb))} = 74800 \pm 9700$ photons/MeV.

However, the emission is very slow. In figure 5.15 we show a typical infrared signal obtained with the previous set up, but with a faster infrared sensor. In this case, in fact, we used a photomultiplier tube (RS 632-01, Hamamatsu), with a 0.1% quantum

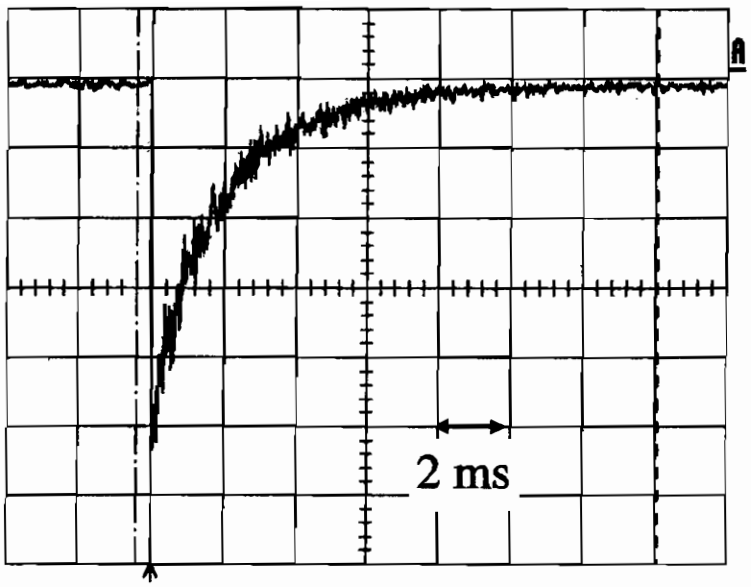

Figure 5.15: Infrared signal from an electron beam-excited YAG(Yb) crystal.

efficiency at 1030 nm. The exponential decay time of the signal is $\tau = 1.88 \pm 0.06$ ms. This result could be expected. From the emission spectrum it is evident that the transition responsible for the infrared scintillation light is the same transition usually exploited to create the population inversion in lasing YAG(Yb) crystals[Bas-95, Buc-67]. Since the population inversion requires long lifetime of the excited state that gives origin to the laser emission, one should also expect a long decay time in the scintillation emission.

5.2.4 Conclusions

We have shown experimental evidences of infrared scintillation in crystals. Among the samples investigated, YAG(Yb) shows an infrared scintillation light nearly a factor 2 higher respect to the

visible light yield of NaI(Tl) ($\simeq$ 40000 photons/MeV), the most widespread used crystal in scintillator particle detectors. In spite of this very high light yield, however, the emission decay time is nearly 2 ms, that is too long for most applications. Nevertheless, there exist some fields (such as tomography or radiography) in which the time response is not so critical, and where the light yield and the density are more relevant[Mos-99]. So infrared scintillation of YAG(Yb), whose density is $\simeq$ 5 g/cm^3, could be successfully exploited in these fields, also because the emission spectrum is centered in a region where low cost Si photodiodes have still good quantum efficiency.

All other investigated samples have an infrared scintillation light yield lower than 5000 photons/MeV. This value is nearly a factor two lower than visible scintillation light yield in BGO ($\simeq$ 8000 photons/MeV), the crystal with the lower light yield among the ones already used. For this reason, we think that the use of those crystals for infrared scintillation radiation detection is not realistic. However, a deeper and more systematic study of the emission of infrared light by particle-excited solid samples could shed light on the interaction mechanisms between charged particles and condensed matter.

Conclusions and Perspectives

The interaction of charged particles with noble gases gives origin to the emission of infrared photons. For lighter gases (Helium, Neon, Argon) the emission is due to the radiative decays of the atomic states excited by the atom-particle scattering. In heavier gases (Krypton and Xenon) some excimer transitions are also present, and in the case of Xenon this emission dominates over the atomic mechanism. The wavelength of the excimer transition depends on the pressure of the gas because of the effects of the neighboring atoms with the outermost electron of the excimer.

The light yield of infrared scintillation in gaseous Xenon (room temperature and nearly atmospheric pressure) is 20600 ± 2400 photons/MeV, i.e. of the same order of magnitude of the light yield of NaI(Tl). Argon and Krypton show much lower light yield (5000 photons/MeV). However, if an electric field is applied in the ionization chamber, the drifting electrons can excite more atoms of the gas, giving rise to an increase of the overall light emission. Such properties could be successfully exploited for practical applications in the fiels of position sensitive particle detectors.

Ionizing particles induce infrared emission in liquid Argon and liquid Xenon as well. However, only atomic transitions are responsible for the emission, because the excimer transitions are suppressed by non-radiative collisional decays. The light yield in liquid Xenon is a factor 200 lower than that in the gaseous phase, and no drift emission either in liquid Argon or in liquid Xenon is observed. The

characteristics of infrared scintillation in liquids are therefore less interesting for particle detection purposes.

Among crystals, YAG(Yb) is the most interesting. Its light yield is very high (74800 ± 9700 photons/MeV), but the emission decay time is very long (1.88 ± 0.06 ms). Nevertheless, applications for industrial purposes could be implemented.

We hope this work will be only the beginning of deeper investigations. Several studies could be undertaken in the next years. Some of them are suggested below.

- Using the experimental apparatus described in Chapter 1, high resolution spectra of particle induced emission in noble gases can be obtained, which could be helpful for an unambiguous assignment of the spectral lines to the corresponding atomic transitions. This could better clarify the mechanism of the emission. Furthermore, the density-dependence of the emission wavelength could be more carefully investigated and compared with the dispersion theory or with the Margenau's statistical theory (see Chapter 2).

- Measurements of the particle induced infrared emission in noble gases at low density should be interesting. In this case, in fact, transitions starting from vibrationally excited states of bound excimers are possible, because the vibrational relaxation is slower than the radiative decay towards the lower excimer state. Thus, at low density, the intensity of the bound-free transitions (as the continuum observed in Xenon) should increase as the pressure is increased, because non-radiative dissociations are more probable when the excimer lies in a high vibrational level (see Chapter 2). Note that this behavior is opposite with respect to the behavior at high pressure, where all the vibrational excitations relax before the radiative decay takes place, and where collisional induced dissociations give rise to a decrease of the emission intensity as a funtion of the gas density (see Chapter 2).

Another information that can be obtained by low density spectra concerns the bound-bound transitions. We have already pointed out (Chapter 2) that a bound-bound transition can not be distinguished, in our experimental data, from an atomic transition, unless no known atomic transition matches the wavelength of the line that appears in our spectrum. At low density some satellite lines could appear near a line that, in the high density spectrum, is isolated. This would be a strong evidence that the transition corresponding to that line is a bound-bound transition. The satellite lines would be the emission originated in the radiative decay from the vibrationally excited states.

- It would be interesting to test the Fermi+polarization model, used in the description of the excimer continuum red shift observed in Xenon and in an Argon-Xenon mixture (see Chapter 2), on other mixtures containing a small amount of Xenon and a buffer lighter gas. The investigation could be also performed as a function of the concentration of Xenon in the buffer gas and could be extended at higher densities.

- The extension of the spectral region at higher wavelengths is a challenging opportunity. We have recently succeeded to put an InSb (EG&G, J10D) infrared sensor at the end of the spectrometer. Its quantum efficiency is reported in figure 1. A spectrum of Neon obtained with such a configuration is reported in figure 2. Note that some new features appear in the wavelength region previously unexplored.

- If a fast, low noise, electronical read out is coupled to the infrared sensor, the Time Resolved Spectroscopy (TRS) of the particle induced infrared emission can be obtained (the spectrometer described in Chapter 1 is already equipped with a board that can perform a 10 ns resolved spectroscopy). This would be a very interesting possibility, because it would allow to analyze the evolution of the spectra with time, thus giv-

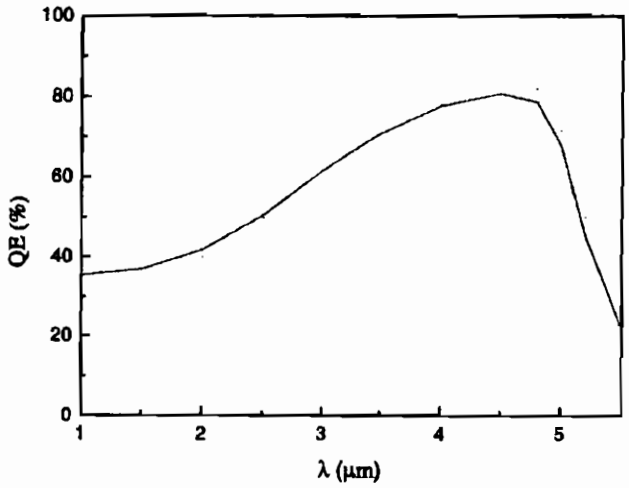

Figure 1: Quantum efficiency of the InSb sensor as a function of the incident radiation wavelength.

ing very detailed informations on the kinetic of the emission mechanism.

- A more detailed study of drift emission is necessary (see Chapter 3). A very interesting issue of this investigation is, for example, the emission spectra. We are now assembling a chamber that will allow to perform those measurements as a function of the gas pressure (up to 3 bar) and of the electric field.

- The application of infrared scintillation for particle detection purposes is worth further investigations (see Chapter 4). In particular, we suggest to study the properties of infrared emission in Helium near an array of thin wires. This could be successfully applied in the development of wire chambers with optical read-out for neutron detection.

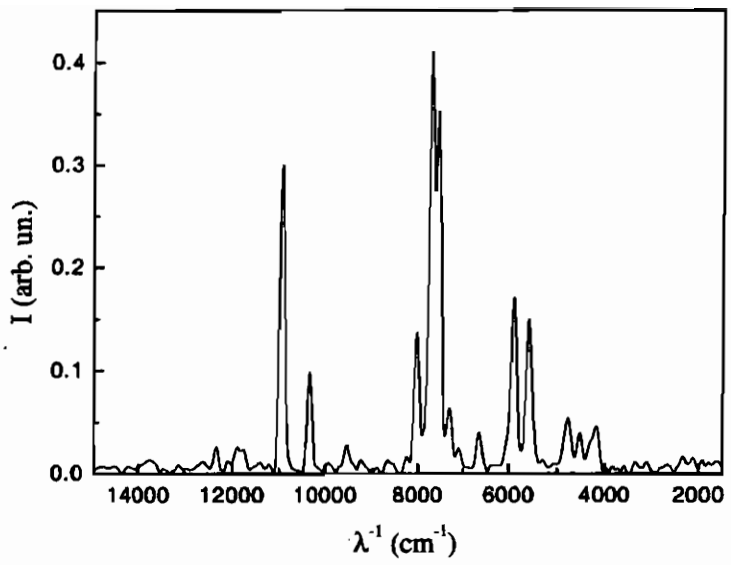

Figure 2: Spectrum of particle induced infrared emission in Neon at room temperature and nearly atmospheric pressure, obtained with an InSb sensor.

- The excimer emission observed in Xenon at $\simeq 1.3$ μm could be used for the development of infrared, high power, excimer laser, whose applications in telecommunication techniques would be extremely interesting.

Acknowledgements

This work was funded by the Istituto Nazionale di Fisica Nucleare. The author acknowledges also the University of Pavia for financial support.

The author is also indebted to P. Antonini, I. Armentano, S. Belogurov, A. F. Borghesani, G. Bressi, G. Carugno, E. Conti, C. Del Noce, and P. Santilli for their invaluable collaboration. The technical support of M. Cavicchi, S. Contran, F. Donadello, P. Gesuato, S. Marigo, M. Negrato, F. Veronese is greatfully acknowledge. Technical drawings have been performed by S. Trevisanato.

Bibliography

[Ama-34] E. Amaldi and E. Segré, Il Nuovo Cimento **11** (1934) 145

[Ara-78] S. Arai, T. Oka, M. Kogoma, and M. Imamura, J. Chem. Phys. **68** (1978) 4595

[Aud-91] E. Audouard and F. Spiegelmann, J. Chem. Phys. **94** (1991) 6102

[Bac-86] C. Bacci *et al.*, CERN UA1, Technical Note, TN 86-112 (1986)

[Bac-94] C. Bacci, P. Belli, R. Barnabei, C. Dai, A. Incicchitti, D. Prosperi, Nucl. Phys. **B35** (1994) 165

[Bar-tbp] A. Barr, L. Bonaldi, G. Carugno, G. Charpak, D. Iannuzzi, M. Nicoletto, A. Pepato, and S. Ventura, Nucl. Instr. and Meth. **A**, accepted for publication

[Bas-95] M. Bass, E. W. Van Stryland, D. R. Williams, W. L. Wolfe *Handbook of Optics* (McGraw-Hill, New York, 1995)

[Ben-93] P. Benetti et al., Nucl. Instr. and Meth. **A327** (1993) 203

[Ber-00] M. J. Berger, J. S. Coursey, and M. A. Zucker, NIST Physical Reference Data (2000)

[Bev-92] P. R. Bevington and D. K. Robinson, *Data Reduction and Error Analysis for the Physical Sciences.* (McGraw-Hill, Boston, 1992)

[Bir-64] J. B. Birks, *The Theory and Practice of Scintillation Counting.* (Pergamon Press, Oxford, 1964)

[Bor-01] A. F. Borghesani, G. Bressi, G. Carugno, E. Conti, and D. Iannuzzi, *submitted to* Chem. Phys. Lett., now *accepted for publication in* J. Chem. Phys.

[Bow-86] N. Bowering, M. R. Bruce, and J. W. Keto, J. Chem. Phys. **84** (1986) 709

[Bra-79] C. A. Brau, A. Gallagher, P. W. Hoff, M. Krauss, M. V. McCusker, F. H. Mies, C. K. Rhodes, *Excimer Lasers*, in *Topics in Applied Physics* **30** (Springer, Berlin, 1979)

[Buc-67] R. A. Buchanan, K. A. Wickersheim, J. J. Pearson, and G. F. Herrmann, Phys. Rev. **159** (1967) 245

[Buc-89] E. Buckley, M. Campanella, G. Carugno, C. Cattadori, A. Gonidec, R. Munoz, S. Ochsenbein, C. Rubbia, D. Schinzel, W. F. Schmidt, W. Seidl, Nucl. Instr. and Meth. **A275** (1989) 364

[Car-98] G. Carugno, Nucl. Instr. and Meth. **A419** (1998) 617

[Cro-03] W. Crookes, Chem. News **87** (1903) 241

[Dok-99] T. Doke and K. Masuda, Nucl. Instr. and Meth. **A420** (1999) 62

[Fer-34] E. Fermi, Il Nuovo Cimento **11** (1934) 157

[Fra-00a] F. A. F. Fraga, M. M. F. R. Fraga, and A. J. P. L. Policarpo, Nucl. Instr. and Meth. A442 (2000) 417

[Fra-00b] F. A. F. Fraga, M. M. F. R. Fraga, and A. J. P. L. Policarpo, Nucl. Instr. and Meth. A442 (2000) 423

[Fro-64] L. S. Frost and A. V. Phelps, Phys. Rev. A136 (1964) 1538

[Gei-09] H. Geiger and E. Marsden, Proc. Roy. Soc. **A82** (1909) 495

[Gei-10] H. Geiger, Proc. Roy. Soc. **A83** (1910) 492

[Gei-13] H. Geiger and E. Marsden, Phil. Mag. **25** (1913) 604

[Gra-72] D. E. Gray *et al.*, American Institute of Physics Handbook (McGraw-Hill, New York, 1972)

[Ham-ds] Hamamtsu Photonics, R5509-71 data sheet

[Hel-85] A. Helaly, J. Birchall, N. Videla, J. S. C. McKee, and W. D. Ramsay, Nucl. Instr. and Meth. **A241** (1985) 169

[Hua-78] S. S.-S. Huang and G. R. Freeman, J. Chem. Phys. **68** (1978) 1355

[Hud-69] R. D. Hudson, *Infrared System Engineering* (John Wiley and Sons, New York, 1969)

[Hur-70] G. S. Hurst, T. E. Stewart, and J. E. Parks, Phys. Rev. **A2** (1970) 1717

[Hux-74] L. G. H. Huxley and R. W. Crompton, *The Diffusion and Drift of Electrons in Gases* (John Wiley and Sons, New York, 1974)

[Ket-97] J. W. Keto, H. Cai, M. Kykta, C. Lei, T. Moller, and G. Zimmerer, J. Chem. Phys. **107** (1997) 6080

[Klo-91] P. Klocek, *Handbook of Infrared Optical Materials* (Marcel Dekker, New York, 1991)

[Kno-00] G. F. Knoll, *Radiation Detection and Measurements.* (Wiley and Sons, New York, 2000)

[Koe-74] H. A. Koehler, L. J. Ferderber, D. L. Redhead, and P. J. Ebert, Phys. Rev. **A9** (1974) 768

[Kub-82] S. Kubota, M. Hishida, M. Suzuki, and J. Ruan, Nucl. Instr. and Meth. **196** (1982) 101

[Lap-75] P. Laporte, N. Damany, and H. Damany, Phys. Rev. **A12**, (1975) 1944

[Lec-99] P. Lecoq, in *Proceedings of the Fifth International Conference on Inorganic Scintillator and Their Applications (SCINT99)* (Moscow State University, Moscow, 1999) 3

[Lin-88a] P. Lindblom, O. Solin, Nucl. Instr. and Meth. **A268** (1988) 204

[Lin-88b] O. Solin, D. Kronman, and P. Lindblom, U. Rosengard, and K. Vourinen, Nucl. Instr. and Meth. **A268** 209

[Lin-88c] P. Lindblom, O. Solin, Nucl. Instr. and Meth. **A268** (1988) 212

[Lin-91] P. Lindblom and T. Olsson, Nucl. Instr. and Meth. **A302** (1991) 113

[Lin-92a] P. Lindblom and T. Olsson, Phys. Scripta **45** (1992) 578

[Lin-92b] P. Lindblom, T. Olsson, K. Aho, and O. Solin, J. Phys. B: At. Mol. Opt. Phys. **25** (1992) 3489

[Lor-76] D. C. Lorents, Physica **82C** (1976) 19

[Mai-81] G. C. Maitland, M. Rigby, E. Brian Smith, and W. A. Wakeham, *Intermolecular Forces. Their Origin and Determination.* (Clarendon, Oxford, 1981)

[Mar-35] H. Margenau, Phys. Rev. **48** (1935) 755

[Mar-51] H. Margenau, Phys. Rev. **82** (1951) 156

[Mar-99] W. C. Martin, J. Sugar, and A. Musgrove NIST Atomic Spectra Database (1999)

[Mes-77a] I. Messing, B. Raz, and J. Jortner, Chem. Phys. **23** (1977) 23

[Mes-77b] I. Messing, B. Raz, and J. Jortner, Chem. Phys. **25** (1977) 55

[Mes-77c] I. Messing, B. Raz, and J. Jortner, J. Chem. Phys. **66** (1977) 4577

[Miy-92] M. Miyajima, S. Sasaki, E. Shibamura, Nucl. Instr. and Meth. **B63** (1992) 297

[Mos-99] W. W. Moses, in *Proceedings of the Fifth International Conference on Inorganic Scintillator and Their Applications (SCINT99)* (Moscow State University, Moscow, 1999) 11

[Mul-70] R. S. Mulliken, J. Chem. Phys. **52** (1970) 5170

[Mus-94] L. Museur, A. K. Kanaev, W. Q. Zheng, and C. M. Castex, J. Chem. Phys. **101** (1994) 10548

[Pol-81] A. J. P. L. Policarpo, Phys. Scripta **23**, 539 (1981)

[Pre-92] W. H. Press, S. A. Teukolsky, W. T. Vetterling, and B. P. Flannery, *Numerical recipes. The art of scientific computing.* (Cambridge University Press, Cambridge, 1992)

[Rac-00] P. J. B. M. Rachinhas, P. C. P. S. Simoes, J. A. M. Lopes, T. H. V. T. Dias, R. E. Morgado, J. M. F. dos Santos, A. D. Stauffer, C. A. N. Conde, Nucl. Instr. and Meth. **A441** (2000) 468

[Ray-84] T. D. Raymond, N. Bowering, C. K. Kuo, and J. W. Keto, Phys. Rev. **A29** (1984) 721

[Raz-70] B. Raz and J. Jortner, Proc. Roy. Soc. (London) **A317** (1970) 113

[Ric-66] S. A. Rice and J. Jortner, J. Chem. Phys. **44** (1966) 4470

[Rot-01] A. Rotondi, P. Pedroni, and A. Pievatolo, *Probabilità, Statistica e Simulazione* (Springer Verlag Italia, Milano, 2001)

[Rut-11] E. Rutherford, Phil. Mag. **21** (1911) 669

[Rut-14] E. Rutherford, Phil. Mag. **27** (1914) 488

[Sau-77] F. Sauli, *Principles of Operation of Multiwire Proportional and Drift Chambers* (CERN Yellow Reports 77-09, Geneva, 1977)

[Sau-78] F. Sauli, Nucl. Instr. and Meth. **156** (1978) 147

[Sch-85] N. Schwentner, E. -E. Koch, and J. Jortner *Electronic Excitations in Condesed Rare Gases*, in *Springer Tracts in Modern Physics* **107** (Springer, Berlin, 1985)

[She-60] B. Sherman, J. Math. Anal. Appl. **1** (1960) 242

[Sil-99] R. M. C. Silva, J. M. F. dos Santos, C. A. N. Conde **A422** (1999) 305

[Str-68] A. R. Striganov and N. S. Sventitskii it Tables of Spectral Lines of Neutral and Ionized Atoms (IFI/Plenum, New York, 1968)

[Tak-96] H. Takahashi, D. Fukuda, and F. Jensen, IEEE Trans. Nucl. Sci. **43** (1996) 1321

[Thi-74] P. E. Thiess and G. H. Miley, IEEE Trans. Nucl. Sci. **NS-21** (1974) 125

[Val-93] J. D. Valentine, D. K. Wehe, G. F. Knoll, C. E. Moss, IEEE Trans. Nucl. Sci. **40** (1993) 1267

[Wan-68] G. H. Wannier *Statistical Thermodinamics* (John Wiley and Sons, New York, 1968)

[Zec-96] A. Zecca, G. P. Karwasz, R. S. Brusa, Riv. Nuovo Cimento **19** (1996) 1